Universitat Politècnica de Catalunya

Strategic Minerals Milling Modelling of High Pressure Grinding Rolls and Process Parameters Dependency

Thesis for the Doctor of Philosophy Degree at the Polytechnic University of Catalonia within the Doctoral Program of the Natural Resources and Environment

Author: Hernán Francisco Anticoi Sudzuki
Directors: Dra. Pura Alfonso Abella
Dr. Josep Oliva Moncunill
Manresa, Spain, 2019

ABSTRACT

Comminution is the most energy consuming process in mining industry, where nearly 60 % of the electricity expenditure is due to grinding purposes. In the nature most of the ore minerals are found finely disseminated and intimately associated with the gangue, thus, liberation is the main target to recover these minerals. In order to optimize the size reduction process, the correct prediction of the characteristics of the product in a milling reactor turns into a crucial task, and is the main motivation to develop this thesis.

The materials used in this study belong to the so-called strategic raw materials, according to the European Commission, to increase competitiveness on the local production to those materials that are key to the industry and their supply is in a risky situation. Tantalum and tungsten ores have been selected from the critical raw materials list, and the model developed was based on these two types of ores.

The material was characterised in minerals and mechanical terms. The mineral composition was determined before being tested under a new methodology, the piston-die test, to find the breakage distribution function. After the test, the samples were also analysed to find breakage mechanism patterns. The experimental session were done using a reformed roll crusher, which was modified in order to have a high pressure environment during compression. The validation stage was performed at the Technische Universität Bergakademie Freiberg facilities, Germany, where the company Köppern Aufbereitungstechnik GmbH & Co.KG has a High Pressure Grinding Roll pilot plant.

The product prediction is presented using an approach of the Population Balance Model (PBM). Such model treats comminution as a single plug flow reactor where selection and breakage functions are involved. In the process of determining parameters of one of these function, more in concrete, the breakage distribution function, by means of the new methodology, novel discoveries on the breakage phenomena were included into this new approach. It has been found that the breakage distribution function is non-normalizable when comminution is done in two compressive conditions: bed particle compression and single particle compression. Some differences on the breakage function parameters when varying the specific pressing force for a certain particle size range where found. These function parameters are closely linked with the mineral composition of the tested material. The content of competent minerals or the presence of altered phases, resulted on variation on these parameters values.

The prediction model obtained using the lab-scale experiments data show consistency, but when the specific pressing force is included into the breakage function determination and into the model itself, it turns in a remarkable good fitting. In this case, the simulated product is compared with an industrial scale device test data. The used feed size distribution was several mono-size particles ranges but an heterogeneous particle size distribution was also tested, being the most similar material that is processed in mining industry.

The working gap was studied to determine its dependency on operative conditions or material characteristics as composition, size or moisture. The energy consumption was also studied and it has been found how the roll speed is the most energy-demanding concept in this type of machinery, and is the responsible of the plant throughput. The specific pressing force, which has an influenced on the product characteristic, has an important influence on the energy demand as well, but is not that relevant as in the case of the increment on the roll speed.

RESUMEN

La comminución es el proceso que consume más energía en la industria minera, donde casi el 60% del gasto energético es debido a esto. En la naturaleza, la mayoría de los minerales de interés se encuentran finamente diseminados y íntimamente asociados con la ganga, por lo tanto, la liberación es el objetivo principal para recuperar estos minerales. Para optimizar el proceso de reducción de tamaño de las partículas, una correcta predicción de las características de la molienda se convierte en una tarea crucial y ha sido la principal motivación para desarrollar esta tesis.

Los materiales utilizados en este estudio pertenecen a las llamadas materias primas estratégicas, según la Comisión Europea, para aumentar la competitividad en la producción local de aquellos materiales que son clave para la industria y su suministro se encuentra en una situación de riesgo. Los minerales de tantalio y tungsteno han sido seleccionados de ésta lista de materias primas críticas, y se ha desarrollado un modelo metalúrgico basado en estos dos tipos de minerales.

El material ha sido caracterizado en términos de su mineralogía y sus propiedades mecánicas. La composición mineralógica ha sido determinada antes de ser ensayada bajo una nueva metodología, denominada prueba de pistón, para encontrar la función de distribución de rotura. Después del ensayo, las muestras también fueron analizadas para encontrar patrones en su mecanismo de rotura relacionada con la mineralogía. Las pruebas de laboratorio fueron realizadas utilizando una trituradora de rodillos reformada, la cual que se modificó para tener un ambiente de alta presión durante la compresión. La etapa de validación del modelo desarrollado en el laboratorio fue ejecutada en las instalaciones de Technische Universität Bergakademie Freiberg, Alemania, donde la empresa Köppern Aufbereitungstechnik GmbH & Co.KG tiene una planta piloto de rodillos de molienda de alta presión.

El producto de molienda en un HPGR se basa en el Modelo de Balance Poblacional (MBP). Dicho modelo trata la comminución como un reactor de flujo de pistón simple, en el que intervienen ciertas funciones de selección y de rotura. En el proceso de determinar los parámetros de una de estas funciones, más concretamente, la función de distribución de rotura, mediante la nueva metodología presentada en este estudio, se incluyeron nuevos descubrimientos sobre los fenómenos de rotura en este nuevo modelo. Entre ellos, se ha encontrado que la función de distribución de rotura no es normalizable cuando la trituración se realiza en dos condiciones de compresión: lecho de compresión de partículas y compresión simple de partículas. Se han encontrado algunas diferencias en los parámetros de esta función de rotura al variar la presión específica para un cierto rango de tamaño de partícula. A su vez, estos parámetros de función están estrechamente relacionados con la

composición mineral del material ensayado. El contenido de minerales más competentes en términos de su resistencia mecánica o la presencia de fases alteradas, dio como resultado en la variación de los valores en los parámetros de la función de rotura.

El modelo metalúrgico desarrollado a escala laboratorio ha usado los datos de la caracterización mecánica de la prueba de pistón. La simulación del producto comparado con los datos experimentales muestra ser consistente. Sin embargo, cuando la presión específica se incluye en la determinación de la función de rotura y en el modelo en sí mismo, el ajuste del modelo se torna notable. En este caso, el producto simulado se compara con los datos de las pruebas en un dispositivo a escala industrial. La distribución del tamaño de alimentación utilizada fue de varios rangos de partículas de mono-tamaño. Sin embargo, también se utilizó una distribución de tamaño de partículas más heterogénea, siendo este un material más similar al que se procesa en la industria minera.

La distancia operativa entre los rodillos (GAP) se ha estudiado para determinar la dependencia de éste ante las condiciones operativas del proceso o debido a las características del material como la composición, el tamaño o la humedad. También se ha estudiado el consumo de energético del proceso y se ha descubierto que la velocidad de los rodillos requiere un consumo de energía elevado, para este tipo de maquinaria y, por lo tanto, responsable de la optimización energética de la planta. Por otro lado, la presión específica, que influye en la característica del producto, también tiene una influencia importante en la demanda de energía, pero no es tan relevante como en el caso del incremento de la velocidad de los rodillos.

ACKNOWLEDGMENTS

This thesis could not have been done without the support and the confidence that my supervisors Dr. Josep Oliva and Dr. Pura Alfonso have deposited in me. Their patience and continuous guidance in the studied topics has a result this work.

I would like to thank all my college mates, who have helped me in the data collection, laboratory work and congress or public presentation during the development of this thesis, I am referring to Eduard Guasch, Sarbast Hamid and Dr. Marc Bascompta.

I am also grateful to the department of Mining Engineering and Natural Resources from the Polytechnic University of Catalonia and all the staff of the university, professors, David Parcerisa, Oriol Tomasa, Lluis Sanmiquel, JJ de Felipe, Teresa Escobet and Toni Escobet. To the laboratory technicians, Francesca Sala and Xavier Guimerà.

This thesis was performed under the frame of the European HORIZON2020 funding programme, project nº642201, name of the project: Increasing yield on Tungsten and Tantalum ore production by means of advanced and flexible control on crushing, milling and separation process, and the acronym OptimOre. I would like to thank to all the project partners that have helped me in my academic development: from The University of Exeter, professors Dr. Rob Fitzpatrick and Dr. Yousef Gorbani, from the TU Bergakademie Freiberg, professor Dr. Holger Lieberwirth, from the Universidad de Oviedo, professor Dr. Juan María Menéndez and Msc. Gloria Gonzalez, from the Chalmers University, professors Dr. Magnus Bengtsson, Dr. Magnus Evertsson and Msc. Lorena Guldris, from the Helmholtz-Zentrum Dresden-Rossendorf, professor Dr. Martin Rudolph. I would like to include in this acknowledgements to the industrial partners of the project, the company Interkonsult, leading by Dr. Peter Graham, and the company EDMA Innova, leading by Dr. Josep María López.

The mineralogical characterization was not possible without the help of Dr. Maria Teresa García Vallés and all the staff of the Crystallography, mineralogy and minerals deposits department of the University of Barcelona.

I would also like to thank to the mining companies involved in this thesis. Strategic minerals Spain, owner of the Penouta mine, and its general director, Francisco Polonio. To the Wolfram Bergbau und Hütten AG, owners of the tungsten mine in Mitersill, Austria. To Mr. Andrés Gonzalez, owner of the quarry established next to the ancient Barruecopardo mine.

Table of contents

CHAPTER I

CHAPTER II

CHAPTER III

CHAPTER IV

CHAPTER V

CHAPTERS VI

LIST OF NOMENCLATURE AND ABBREVIATIONS

AFD	Adjustable Frequency Drive
α_n	Angles formed between the nip zone level and the centre of the roll [rad]
B	Exploitation permission type (According Spanish regulations)
BPC	Single particle compression
B_{ij}	Breakage Distribution Function, cumulative form
b_{ij}	Breakage Distribution Function, differential form
b_{ij}^{S}	Single particle compression breakage function, differential form
b_{ij}^{bf}	Bed compression breakage function for fines particles, differential form
b_{ij}^{bc}	Bed compression breakage function for coarse particles, differential form
B_{ijkl}	Quadrivariate breakage function
C	Selection function for pressure ranges
D	Roll diameter [m]
D_{10}	Diameter of the particles that represents the 10% of the population [µm]
D_{50}	Diameter of the particles that represents the 50% of the population [µm]
D_{80}	Diameter of the particles that represents the 80% of the population [µm]
Dp_i	Parent particle size [mm]
dp	Particle diameter size [mm]
dp_i	Progeny particle size [mm]
d_1	Selection function parameter, dimensionless
δ	Bulk density of the material in the extrusion zone [t/m^3]
EC	European Commission
EDS	Electron dispersive spectrometer
F	Feed size range [mm]
F_i	Feed vector
Fsp	Specific pressing force [MPa]
Gap	Distance between two rolls
G_s	Process throughput [t/h]
HPGR	High Pressure Grinding Rolls

k	Breakage function parameter, dimensionless
m_i	Mass for different size classes i
N_t	Number of single particle compression stages
N	Length of inputs vector for model prediction
n_1	Breakage function parameter, dimensionless
n_2	Breakage function parameter, dimensionless
n_3	Breakage function parameter, dimensionless
OSS	Open set setting
PBM	Population Balance Model
P^n	Product simulation for N_t determination
p_i	Product vector
ppm	Part per million
RMSE	Root Mean Square Error
SAG	Semi-autogenous mills
SPC	Single particle compression
S_0	Working gap [mm]
S_n	Selection function
Wa	Specific energy consumption for tumbling mills, coarse particles [kWk/t]
Wb	Specific energy consumption for tumbling mills, fines particles [kWk/t]
Wc	Specific energy consumption for conventional crushing [kWk/t]
Wh	Specific energy consumption for HPGR [kWk/t]
Ws	Specific energy consumption correction parameter
Wt	Total specific energy consumption [kWk/t]
wt%	Percentage in weight
U	Rolls speed [m/s]
ρ	Bulk density of the material in the feed zone [t/m^3]
V_i	Experimental value
V_f	Final model predicted value
Y_0	Breakage function parameter, dimensionless
y_i	Calculated vector for error determination

x_n	Distance between rolls when material is under the nipper action
Xc	Selection function as a cut-point
XRD	X-ray diffraction

LIST OF FIGURES

LIST OF TABLES

CHAPTER I

Introduction

Objectives

1. INTRODUCTION

1.1. Comminution in HPGR

Particle size reduction, also denominated as *comminution*, is a unit operation of great importance for a wide range of industries (Reid, 1965). It is included cement field, pharmaceutics, ceramics but especially in mining activities (Datta and Rajamani, 2002), due to the high impact in terms of cost in energy consumption and tool wear (Levesque and Millar, 2015; Guasch et al., 2018; Pérez-Garcia et al., 2018). It has been computed that nearly 55% of overall electricity expenditure in a mineral processing plant is related to grinding purposes (Buckingham et al., 2001; Sayadi et al., 2014), but less than 2% of this power is used in real comminution (Fuesternau and Abouzeid, 2002; Radziszewski, 2013) while the rest is due to heat losses (Bouchard et al., 2016).

Most of the minerals with an economical interest, or ore minerals, are finely disseminated and intimately associated with the gangue. Thus, they must be unlocked or liberated for further recovery. The main objective of comminution is to achieve a free surface of this minerals of interest, before separation can be undertaken (Wills, 1992). The liberation of the ore from the gangue involves two main operations: crushing, and, most of the time, grinding (Hill and Ka, 1996; Liu et al., 2018; Sousa et al., 2018). Crushing reduces the particle size of the ore to such level that grinding can be carry out until reach mineral liberation. However, Napier-Munn et al (1996) divided comminution in crushing, coarse grinding and fine grinding, in terms of product particle size. When it is referred to the machinery that perform the comminution, they are classified in two types; crushers and mills. Whereas crushers mainly operate on dry ores, grinding mills mostly work on slurries, which mean that a certain amount of water must be added to the ore before it enters the milling circuit (Sbárbaro and del Villar, 2010). The machineries involved to perform this task belong to the tumbling mills type: ball, rod, pebble autogenous and semi-autogenous (King, 2001). The High Pressure Grinding Rolls (HPGR) was conceived as a mills, however it is also considered as a crusher, depending on the flow-sheet needs nor the reduction ratio needed to get liberation (Liang et al., 2016; Genç and Benzer, 2016; Anticoi et al., 2018a; Anticoi et al., 2018b).

The differences on the different grinding devices lie on the material breakage mechanism. Abrasion is produced when the particles are locally stressed around the surface. This phenomenon mainly occurs when the particles are large and the stresses applied are not high enough to cause fracture. The effect of this action is a population of fines particles taken from the surface of the parent particle and other larger particles, close to the parent particle size. This process is called a birth process because of the appearance of these smaller particles. However, there is no corresponding death process since the parent particle is not destroyed and, at most, it moves across the lower boundary of its size class. This behaviour is reflected in the population balance models for autogenous mills, where the large particles act as a grinding media.

Cleavage occurs when the original mineral has some preferred surfaces along which fracture is likely to happen. If multiple fractures of the daughter fragments do not occur, this mechanism of fracture tends to produce several relatively large fragments together, which reflect the grain size of the original material with much finer particles that originate at the points of application of the stress. The size distribution of the product particles is relatively narrow but will often be bimodal, as illustrated in Figure 1, or even multi-modal, being more heterogeneous than the abrasion type but it still generates larger daughter particles, near 50-80% of the size of the initial particle.

Shatter is produced by the aggressive impact (intense stress) of the grinding media or the pebbles among themselves, which produce fragments of relatively small sizes with a relatively wide range of particle size distribution. A broad spectrum of product sizes is produced and this process is unselective. Multiple fracture processes occur and so progeny particles are immediately subject to further breakage by successive impacts. In short, the shattering process consists of a series of steps in which the parent particle is fractured and this is followed immediately by the sequential fracturing of successive generations of daughter fragments until all of the energy available for fracture is dissipated. These successive fractures take place in very rapid succession and on the macro time scale; they appear to be one single event. It is the most effective comminution action in terms of energy and size reduction rate (Monov et al., 2012). Shattering is the most common mode of fracture that occurs in industrial autogenous, rod and ball mills.

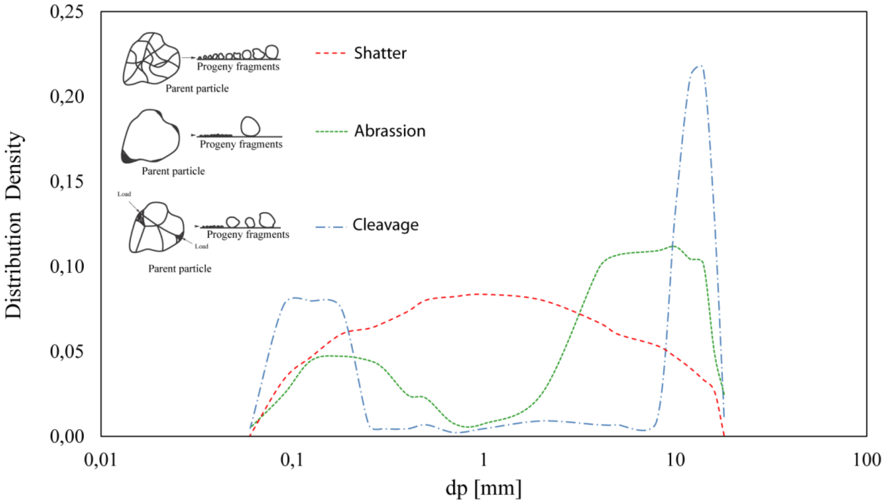

Figure 1. Mechanism fracture of the particles and the distribution density of the progeny fragments.

Since ball mills take advantages of the impact and abrasion effect, the resulted product of comminution of these devices is a fine powder with reduction ratio from 20:1 to 200:1. In the other hand, rod mills reduction is lesser than in ball mills, reaching up to a maximum of 20:1, where impact action is preferred when is not advisable to generate over-ground products. For HPGR the product particle size distribution could be equal or even finer than a ball mill (Figure 2), but, comminution is carried out mainly to compression rather impact or abrasion.

Two ways of compression are present in high pressure grinding rolls: single particle compression and bed particle compression. The inter-particle breakage in the compression zone between the rolls is achieved by choke fed condition (Otherwise, the HPGR runs as a conventional roll crusher). During comminution, a pre-crushing stage is observed and is the denominated single particle compression stage. After that, a particle bed builds up between the rolls and the applied load is transferred to the material by the surrounding particles (Dundar et al., 2013).

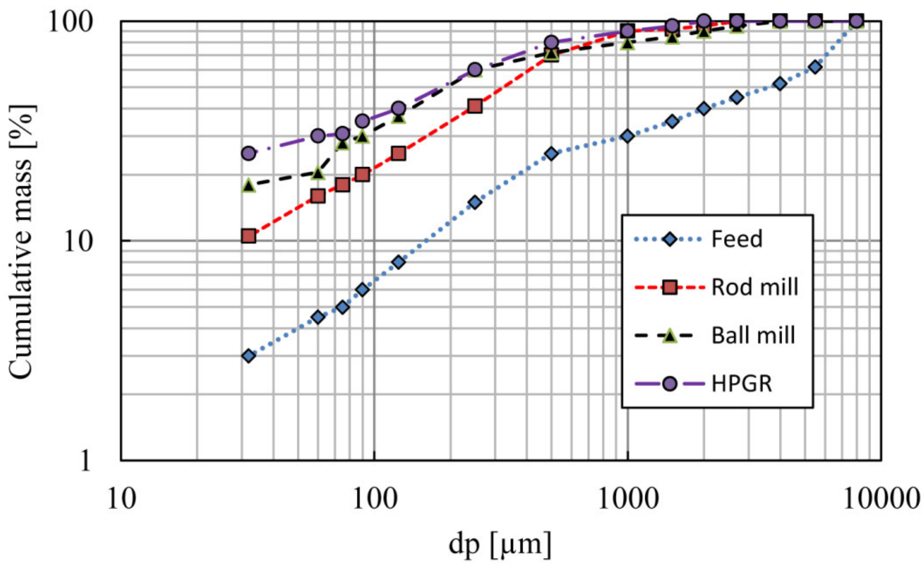

Figure 2. The different PSD reaching by a rod, ball and HPGR mills (Gupta, 2006).

Several advantages are observed between HPGR and conventional tumbling mills. One of them is related to the random fracture mechanism, which is present on ball mills. This phenomenon does not happen in HPGR; the pass of them through the rolls comminutes particles. Thus, the comminution in HPGR is highly efficient in terms of energy losses and exhibit improved liberation via inter-phase cracking (Tromans and Meech, 2004). The inter-particle bed breakage, which occurs when the compressive forces from rotating rolls, such as the HPGR, transmit energy through layers of particles, a preferential weakening of the coarser particles occurs (Tavares 2005; Ghorbani et al., 2013).

In terms of energy consumption, HPGR results to be also highly efficient, with relatively high throughput rate and low roller wear (Abouzeid and Fuesternau, 2009). Moreover, a combination of different devices could optimize mineral processing of the ore, taking into account the specific energy consumption that generates a type of material (Ballantyne et al., 2018). Table 1 show the overall specific energy consumption Wt for different combined circuits of comminution (Liang et al., 2016). Best performance is reached using a HPGR in its circuit.

Table 1. Specific energy consumption (kWk/t) of three combined circuits. Wa, specific energy to grind coarser particles in the tumbling mill; Wb, specific energy to grind finer particles in the tumbling mill; Wc, specific energy for conventional crushing; Wh, specific energy for HPGR; Ws specific energy correction in for size distribution and W,t is the sum of all specific energy consumption values) (Liang et al., 2016).

	Crusher + ball mill	Crusher + HPGR+ball mill	SAG+Ball mill
Wa	4.25	1.75	7.98
Wb	4.66	4.66	4.66
Wc	4.41	1.07	--
Wh	--	2.49	--
Ws	0.71	--	--
Wt	11.03	9.97	12.64

The HPGR is also used to prepare a weaker material for further comminution in ball mills. Figure 3 shows how the size reduction is better with a combination of these two devices.

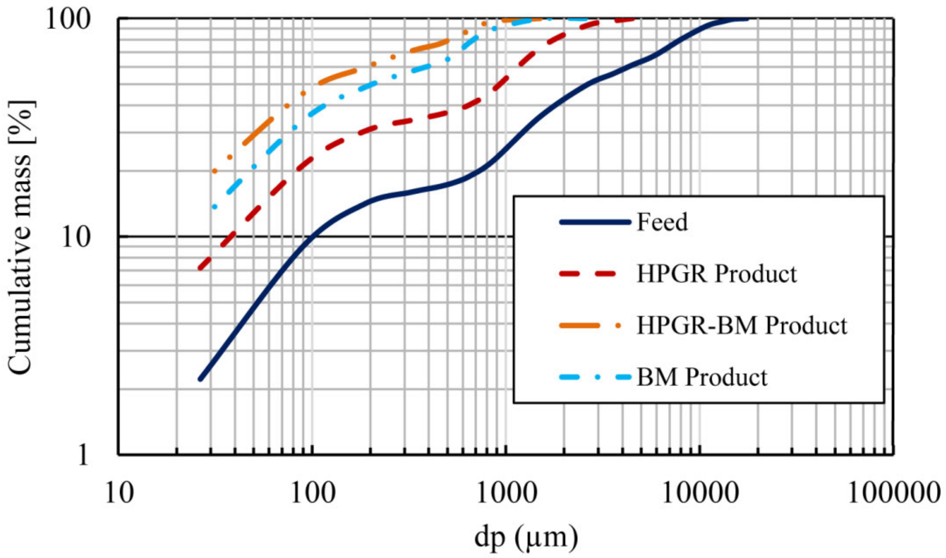

Figure 3. Comparison between product from combination of ball mil and HPGR (Ahmad et al., 2018).

In general terms, the HPGR result in an interesting device that could reduce cost and increase efficiency in a process circuit. Thus, an accurate model to predict the particle size distribution from different feed sizes and varying the operative conditions is a key point in order to do this optimization task.

1.2. European frame of the study

Many effort of the European Commission have been done in order to aim and secure Europe's global competitiveness. Between the guidelines that drive this initiative are to put in the heart of the EU's blueprint for smart, sustainable and inclusive growth and jobs (https://ec.europa.eu/programmes/horizon2020/what-horizon-2020).

Is in especial concern of our field, that the EC has analysed the local raw material production, and base on three main items; link to industry, modern technology and environment issues, the commission has considered the existence of several Critical raw materials. This is a list of 61 candidates of non-energy and non-agricultural materials that can be important for Europe economic and they can suffer a supply risk (Figure 4).

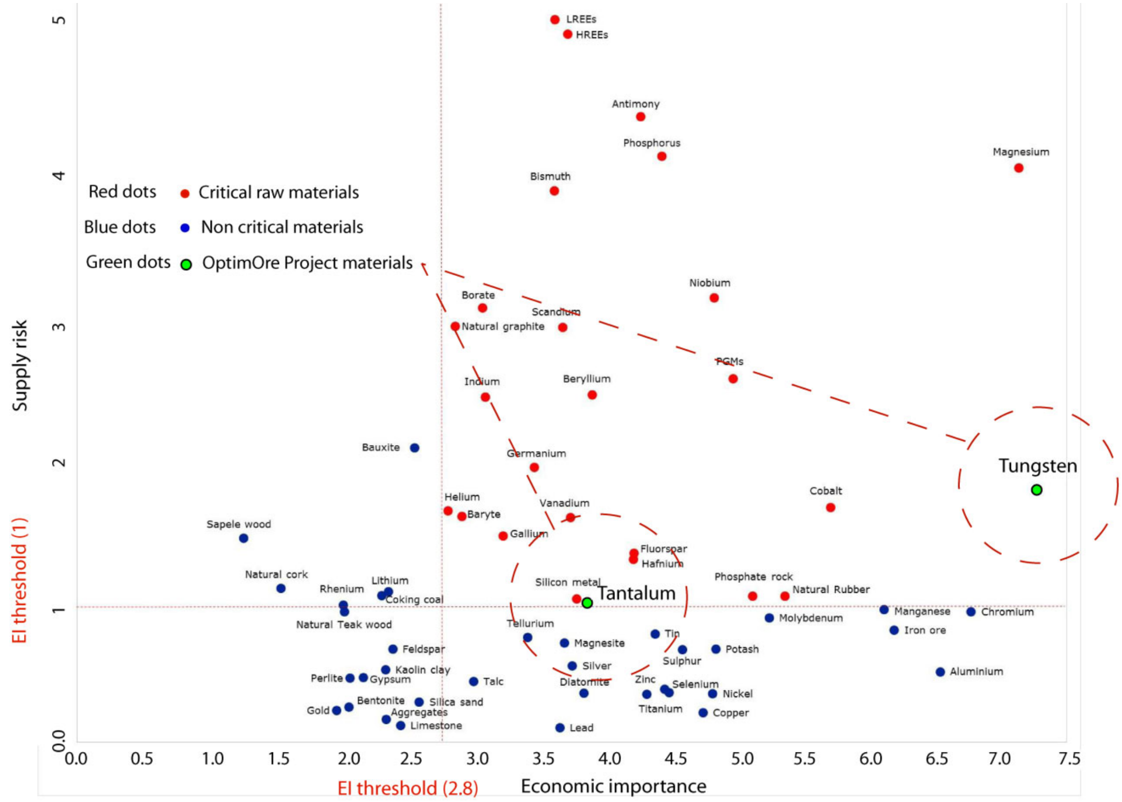

Figure 4. List of the critical raw material, from the EC (European Comission, 2017).

This work is in the frame of the European research project acronym OptimOre and named Increasing yield on Tungsten and Tantalum ore production by means of advanced and flexible control on crushing, milling and separation process and it has received funding from the European Union

Horizon 2020 research and innovation programme under grant agreement nº 642201. In this project, two main critical raw materials were selected in order to create innovate and advances technologies to optimize their mineral processing. Despite the project is dedicated to a full processing plant optimization, the different partners of the consortium were responsible for each particular stage of the process. Thus, the Polytechnic University of Catalonia was in charge on the milling field, studying milling process and mathematical modelling of the different comminution devices of this stage. One of the machinery to be studied was the HPGR, and is the main topic of this thesis.

1.3. Material context

The materials used in this study were two strategic raw materials from the European point of view perspective. The high demand of tantalum in the manufacture of capacitors and super-alloys (Korinek, 1995; Moser, 1999; Alfonso et al, 2018), and the social impact that its exploitation means in Africa (Jønsson and Fold. 2011), raises this metal into the one of major target in modern industry. Another issue present of this metal lies on the poor quality and performance of the possible substitution materials available in the market.

Tantalum (chemical symbol Ta) is a silvery-grey hard, transition metal. It has a high density (16.6 g/cm3) and the 4th highest melting point (3020 °C). It is highly resistant to corrosion and has a great permittivity. Tantalum's estimated abundance in the upper continental crust is 0.9 ppm (Rudnick, 2003), which is quite rare. This metal is not found as a free metal in nature but occurs notably in the minerals microlite and columbite-group minerals (CGM).

Tantalum occurs in the nature in minerals together with niobium. Both have similar properties but in the case of tantalum they are more extreme. Its major uses are in capacitors (electronic devices, cell phones etc.), super-alloys (aerospace), sputtering targets (storage media, inkjet printer heads etc.), but also carbides (cutting tools), mill products, medicals and chemicals (Mackay and Simandl, 2014).

The primary tantalum deposits are pegmatites and rare metal granites (Černý 2005; Linnen et al., 2014). In Europe, tantalum reserves occur in tantalum-rich lithium–cesium–tantalum (LCT)-type pegmatites and granites, which are commonly related to the Variscan European belt, which extends from the Iberian Massif, the Massif Central (France) and Central Europe. With the exception of very small quantities of by-product from kaolin mining in France, there is currently only one primary mine production of tantalum in the EU, the Penouta mine, belong to Strategic minerals company, Spain. There are a few others processors notably in Estonia (from imported primary ore), Austria, Germany and the UK (mainly from secondary material).

The same context is attributed to tungsten. Declared as critical raw material from the European commission side since 2011, the importance of this metal for the economy in Europe is doubtless. Tungsten (W), also known as wolfram, is a hard, rare metal. Under standard conditions, tungsten is found naturally on Earth almost exclusively in mineralogical form. It is mainly contained in wolframite and scheelite. The free element is remarkable for its robustness and has the highest melting point of all the elements. Its high density is 19.3 times that of water, comparable to uranium and gold, and much higher (about 1.7 times) than that of lead. Tungsten is an important metal with very low substitution, and a key component in steel manufacturing, construction, oil drilling, and mining industries. It is also used in the fabrication of wires and filaments used in electrical, heating, and lighting applications. The hardness and high density of this metal give it military applications in penetrating projectiles. Tungsten compounds are also often used as industrial catalysts (European Commission, 2017).

2. OBJETIVES

2.1. General objectives

The reduction of energy consumption during the mineral concentration is the main challenger in the current mining activity. This can be the cut point of an exploitation to be closed or continue producing. The variables which allow a process plant to obtain a profitable product have to be very well known. The prediction of the material features as the particle size distribution and its intrinsic mineral liberation degree could be the key to optimize the process. For this reason, the main objective of this study is to create innovated models that describe the behaviour of the material inside a HPGR taking into account the operative parameters, the material characteristics and the energy used, in order to obtain improvements over the current models available.

2.2. Hypothesis

The assumptions made in this study are based on the literature background and basically on some observation done on the current models that describe the comminution in High-pressure grinding rolls devices: it was not possible to find an empirical methodology to determine model function parameters (the reverse calculation is often used, helped with several inputs of the process), and it starts from the basis of the particle breakage behaviour for a certain types of material, until the complete operation of the machine. Thus, the hypotheses raised in this study are:

A) Hypothesis 1: It is possible to mechanically characterise the materials in terms of the breakage distribution function commonly used for tumbling mills, but applied for High Pressure Grinding Rolls.

B) Hypothesis 2: The breakage distribution function is mineral composition dependant but it is also influenced by the particle rupture type.

C) Hypothesis 3: It is possible to determine the breakage function parameters from two sources: mechanical characterization of the samples, and by their mineralogical composition.

D) Hypothesis 4: The breakage distribution function is non-normalizable for different specific pressing force.

E) Hypothesis 5: The current models are modifiable and can be improved according to the new discoveries in the rupture functions

F) Hypothesis 5: It is possible to define the operative gap on operative setting.

G) Hypothesis 6: The model is scale-up from laboratory scale to industrial type of machinery.

H) Hypothesis 7: The study of the HPGR is related to the energy consumption, and the model is necessary to implement the best performance of the machine.

2.3. Specific objectives

The main objective and the hypothesis stablished can be achieved and probed through the accomplishment of several specific objectives. They are sorted chronologically in according with the development of the present research.

A) To characterize the materials in order to stablish the breakage mechanism that occurs in a HPGR.

B) To determine new methodologies in order to find accurate functions that describes the breakage mechanism.

C) To design experiments in lab-scale HPGR in order to study the performance of the device with tantalum and tungsten ores

D) To create new approaches based on the mineral characterization, the breakage mechanism and the experiments in laboratory

E) To use mathematical algorithms in Matlab®2016a code in order to simulate the particle size distribution within the new model

F) To carry out tests with different materials in an industrial scale HPGR, in order to check the consistency of the new generated model.

G) To validate the model and to study the operative conditions affection on the process and the model itself.

CHAPTER II

Literature review

3. LITERATURE REVIEW

3.1. Theoretical background

Early known as High Compression Roller Mills (Schönert, 1988), the High Pressure Grinding Rolls have become in a modern and highly efficient technology. Applications of this equipment are related to the clinker cement industry in early stages (Kellerwessel, 1990; Hasanzadeh and Farzanegan, 2011) and after that, in mineral processing activities, especially in metallic ore deposits (Guevara and Menacho, 1992; Austin et al., 1993; Morrel et al., 1997; Torres and Casali 2009; Abouzeid and Fuerstenau, 2009; Saramak, 2011; Numbi and Xia, 2015). It is proven to reduce the operating costs in full scale plants when compared with other milling technologies, which is especially important with low-grade ores and inherent low efficiency of the conventional comminution system (Abouzeid and Fuerstenau, 2009; Liang et al., 2016; Lei et al., 2018). These benefits on energy savings (Hindle and kalala, 2009) and simplicity in the process are obtained even generating a product particle size reduction equal or lesser than other mills, as ball or rod mill (Gupta, 2006). In addition high pressure grinding rolls produce much more internal particle fractures than conventional crushers (Tavares 2005; Daniel, 2007; Kodali et al., 2011; Baum and Ausburn, 2011; Ghorbani et al., 2011; Fernandez and Brochot, 2014; Han et al., 2012; Charikinya et al., 2015). Whereas in conventional crushers the impact and abrasion breakage mechanism are dominant in the high pressure grinding rolls the particles are broken by compression in a packed particle bed, and not by direct nipping of the particles between the two rolls (Ghorbani et al., 2013).

The prediction of the product particle size distribution comminuted in a HPGR has been estimated using the widely known Population Balance Model (PBM). It is a mathematical description of a size-mass balance model for the breakage process (Hasanzadeh and Farzanegan, 2011; Kwon et al., 2012; Esnault et al., 2015), which is decomposed in different sub-functions that describe the behaviour of the particles being processed in a high-pressure environment. It is formulated in terms of two basic parameters: Selection criteria and breakage criteria. The selection function shows the chosen particles for being broken. In the breakage criteria, there are two approaches: the particles that have the probability to be comminuted under single particle compression and the undersized ones that are broken by the particle bed compression effect (Austin et al., 1993; Austin and Trubelja, 1994; Morrel et al., 1997; Daniel and Morrel, 2004; Torres and Casali, 2009). In addition to this selection criterion, the nature of the distribution of the particles that have been ground is described by the breakage distribution function, B. This function indicates the progeny particles arrangement caused by comminution of every single particle from a feed population (Kelly and Spottiswood, 1990; Kwon et al., 2016). These mathematical expressions are structured in such a way as to depend on feed particle size, size reduction ratio between parent particles and their progeny, and especially on certain parameters that are linked to the nature of the material being ground and on the type of comminution equipment (Hill and Ka, 1996). A widespread tendency in modelling is to adjust the parameters of these functions with experimental results (Torres and Casali, 2009). Unlike in mills, where there are experimental methodologies to find and scale-up the breakage and kinetic functions (Austin and Luckie, 1971; Austin and Luckie, 1972; Austin and Concha, 1994; Benzer et al., 2011) there is not a single methodology to determine the function parameters for processes using HPGR. Some authors used a piston compression test to study the breakage behaviour under a pressure environment (Benzer et al., 2011; Dundar et al., 2013). Meanwhile, Tavares (2005) used an ultra-fast load cell to determine the particle fracture energy. Further studies on single particle crushing, energy input required for crushing a single grain and crack generation modelling have been performed (Zhang et al., 2016).

3.2. Device description

The HPGR machinery is design with two rollers that are mounted in a strong frame. One of the rollers is fixed and the other is floating, so a movement between then is possible and nowadays is denominated as working gap (Figure 5). Normally, the initial gap is nominal distance, then, the feed flows from a funnel placed above the rollers (Schönert, 1988) and the gap is opened. It is not possible to adjust the working gap; their overture depends on some feed material characteristics, as size or moisture percentage.

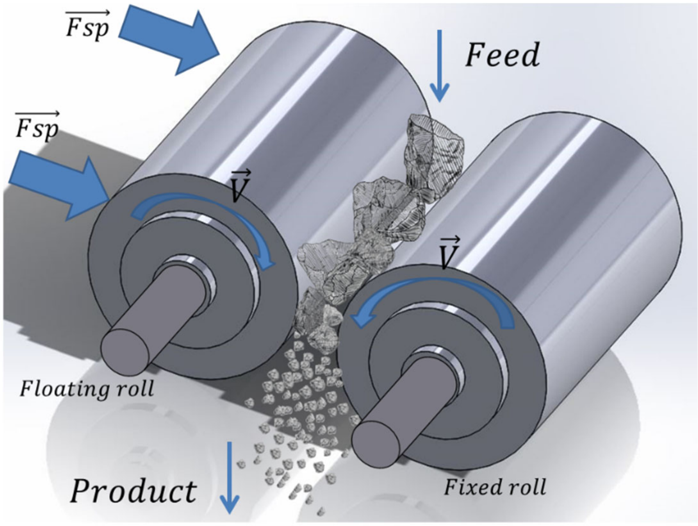

Figure 5. Compression action in a HPGR. The feed enters into the rolls gap in choke fed condition. The floating roll exert a specific pressing force into the material, producing comminution.

To perform the operation, pressure is applied hydraulically through four cylinders to the roll that is designed to move laterally. The amount of feeding material can be manipulated to achieve the optimal operating conditions, but usually, it is a characteristic of the feed ore, the roll diameter and surface characteristics (Barrios and Tavares, 2016). A crushing specific pressing force of the order of 200 MPa is applied, but for hard ores, higher pressures, until 340 MPa are used. The dimensions of the rolls used in the mineral industry are 0.7- 2.8 m diameter with a Length/Diameter ratio between 0.2 - 0.6. The roll speeds usually range between 85-105 m/min (Figure 5).

The roll faces are either studded or have Ni-hard liners (Figure 6). The studs are made of tungsten carbide to combat heavy abrasion but softer studs have better life as they are less brittle (Gupta, 2006). The shape of the studs is also important. There are hemispherical top, protected from being destroyed by stress concentration, or round edges, to be protected during, transportation, installation and production. These studs also help to form a protective layer of feed material on the surface of the rolls which prevents excessive wear of the roll surface and also facilitates material entry into the gap between the rolls. The wear phenomenon of the roll is mainly affected by three main factors; the stud material, ore properties and device set-up (Kazerani and Sam, 2017; Klymowsky et al., 2002).

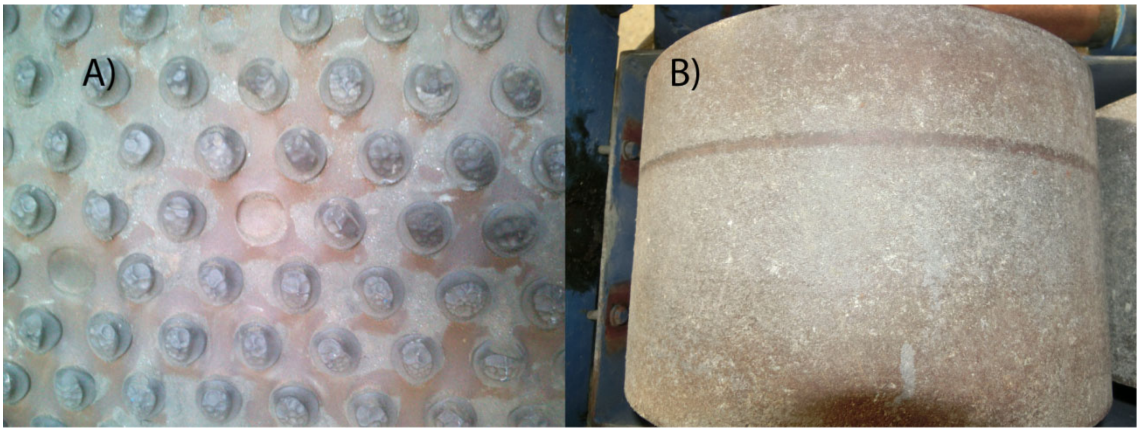

Figure 6. Roll Surface liners, A) Studded types (Kazerani and Sam, 2017) B) Smooth type.

3.3. Milling process in HPGR

The feed material enters between the rolls in choke fed condition, in order to generate pressure from all sides. The forces of compression and friction between the rolls and particles are responsible for size reduction provided the combined forces exceed the compressive strength of the particle. When a large quantity of rocks is held between the rolls and is subjected to high pressure, comminution could take place by compressive forces as well as by inter-particle breakage, provided again that the total applied pressure was greater than the crushing strength of the rock fragments. The product again is a continuous "ribbon" of crushed material in the form of a compacted cake (Gupta, 2006).

The particles begin to be comminuted since a certain compression cut-point denominated nipping, which is closely related to a nip-angle. This is basically the slope formed between the central axis of the roll with the gap line and the extension from the central axis of the roll to the roll surface where the nipping action begins (Figure 7). If the feed size particles are bigger than the gap size, single compression will appear. For particles smaller than the gap size, a bed particle action is predominant. The size reduction in a HPGR is done mainly in the bed compression zone, where the multiple micro-fractures occur and it generates the finest material. The operative gap will be influenced on the specific pressing force applied, and other factors, as the material characteristics or the feed size distribution, as well (Kellerwessel, 1990; Fuesternau and Kapur, 1994; Fuesternau et al., 1991).

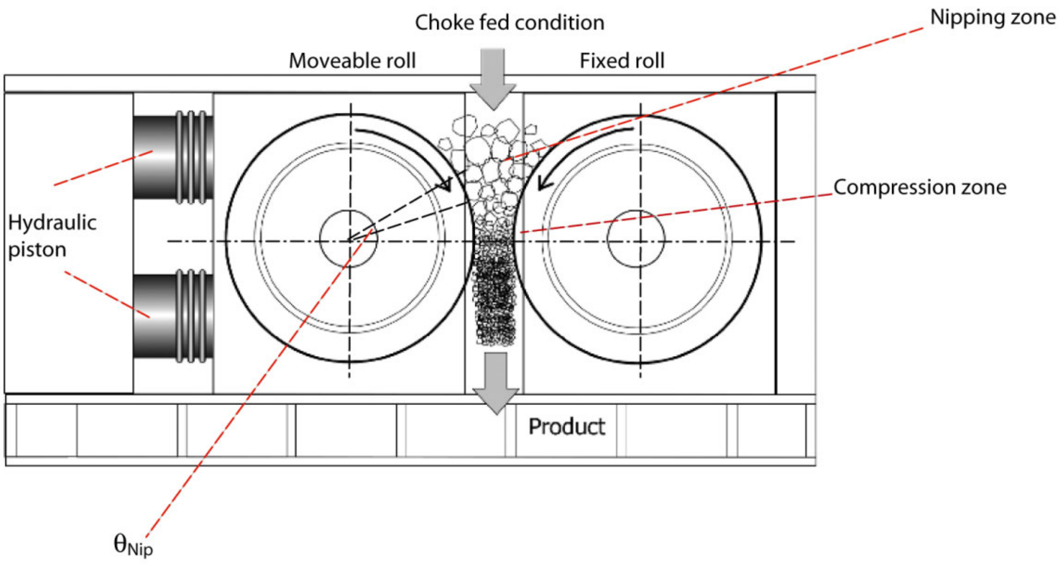

Figure 7. HPGR device diagram (Gupta, 2006).

The product of grinding from HPGR is mainly directly proportional to the specific pressing force (Apling and Bwalya, 1997; Schneider et al., 2009; Vyhmeister et al., 2019). It generates a fine kind of material, in some cases liberated enough to carry out an optimal recovery (Apling and Bwalya, 1997), or with micro-cracks that could improve further downstream milling process or leaching recovery of valuable minerals (Ghorbani et al., 2013; Dundar et al., 2013).

3.4. HPGR in process flowsheet

The applications of the HPGR in comminution circuits are designed to obtain maximum benefits and energy saving, taking into account the high capital cost of the HPGR (Rosario et al., 2011). The current flowsheet in the mining processing include several steps of comminution with a pre-crushing HPGR before ball, rod or SAG mills or in some cases, generating the final fines to recovery process (Rosario, 2017; Liu et al., 2018). The cement industry, for example, commonly uses HPGR as a pre-crushing, with several combinations on the classification stage before milling. Figure 8A show how the HPGR discharge is split into two parts, one portion is recycled back to the HPGR to obtain better particle bed breakage by filling the voids among the large particles. The other part of the material goes to the final milling to be separated by air- classifiers. To improve the optimal particle bed formation, the flowsheet is slightly changed, giving an increased flow fed from the recirculation of the undersized product of the HPGR itself and the milling product, through the air-classifier (Figure 8B).

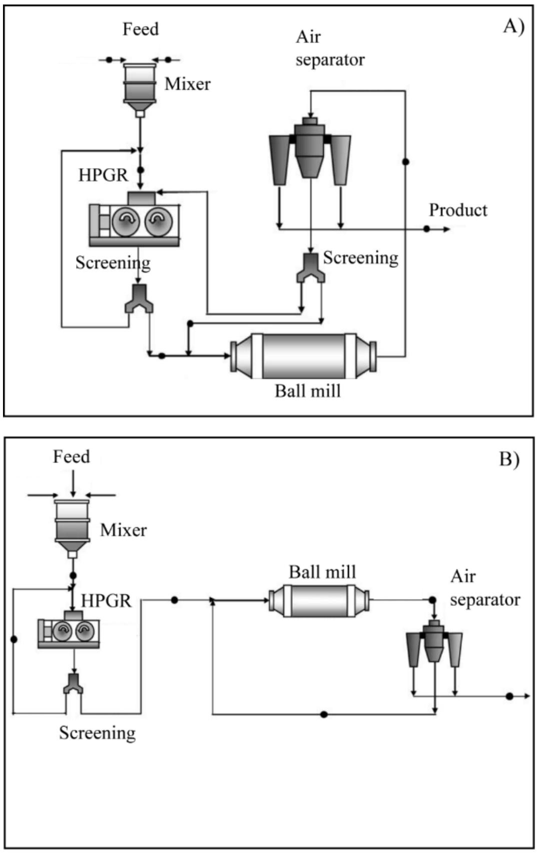

Figure 8. A) HPGR combined with ball mil and air separator, B) HPGR combined with ball mil and air separator with no stock materials (Aydogan et al., 2006).

Other improvements in the HPGR flowsheet are related to the mineral liberation properties, which is closely link to the mineralogy and the texture of the ore (Liu et al., 2018) and the subsequently improvement on the separation process.

3.5. Models

3.5.1. Functions used for modelling

All models have several elements in common. There is a selection function, which discriminates the particles population on their physical characteristics, and there is a breakage function, which is the responsible of the daughter particles arrangement from a parent particle population after a comminution action. In the case of the selection function, according to the Austin et al (1993) model, a relation between the compression action nature and the particle size population is established. In the nip action zone, if the particles are larger than a certain size, they will be under single compression action. If they are not, the bed compression effect is present. Thus, the selection function is a probability function, in which a fragment size produced by fracture in the rolls has a smaller probability of leaving without fracture than other with size small enough to enter into the bed compression. Morrel et al (1997) and Torres and Casali (2009) models are more simple, and defines a cut-point where the particles are or are not compressed singly.

The breakage function shows a wide variety of approaches, with different nature or defined on different aspect of rupture. The most popular one is the so called Empirical model based on progeny population. It was firstly describe by Whiten (1972) and Whiten et al., (1979), where it says that a progeny population is made of a mixture of two separate populations. This function is dependent of the progeny/parent particle ratio. Furthermore, three parameters, originally related to mineral characteristics exclusively, composed this breakage approach (Figure 9).

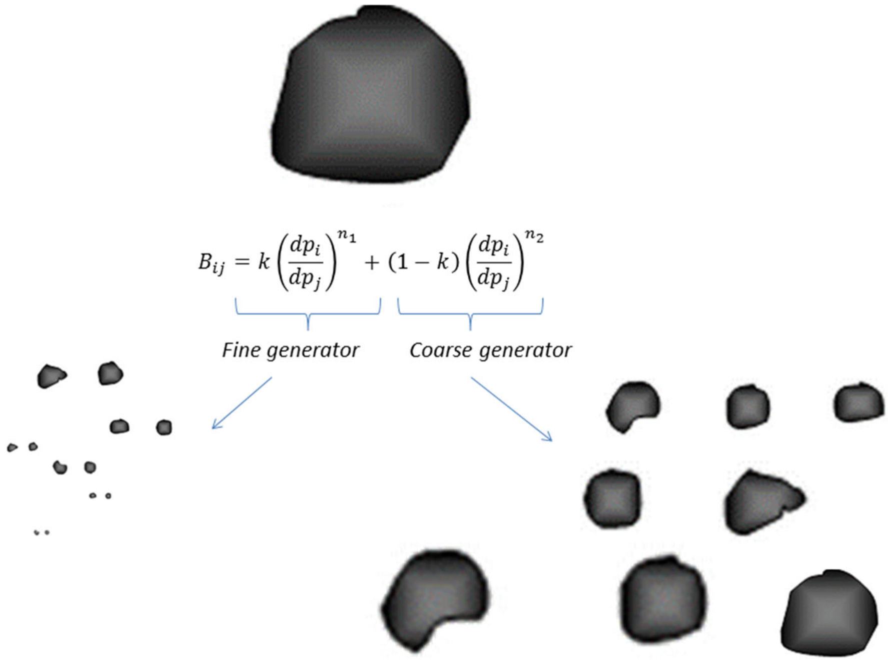

$$B_{ij} = \underbrace{k\left(\frac{dp_i}{dp_j}\right)^{n_1}}_{\text{Fine generator}} + \underbrace{(1-k)\left(\frac{dp_i}{dp_j}\right)^{n_2}}_{\text{Coarse generator}}$$

Figure 9. Breakage function form proposed by Whiten (1979) in which describe the particle population generated by a parent particle in terms of size distribution.

A second approach of the breakage distribution function (Broadbent and Callcott 1956) proposed a function based on Rosin-Rambler-Bennet Equation, which is used as a basic in engineering, in a continuous mode. It is also dependent on the progeny/parent ratio, and it has only one parameter, mineral characteristic dependent.

Nikolov (2002) proposed an extension of the originally Whithen (1972) approach, being also mineral characteristics dependent, with no influence on the operative parameter of the comminution.

In the same field, an interesting approach was generated based on the type of energy available to break the particle during the impact. In this case, Tavares and King (1998) developed the Ultra-fast load cell (UFLC). The breakage function is the sum of all individual breakage functions from each particle. All parameters are mineral dependent and they describe the way that the material breaks in terms of the energy necessary to do it.

The most complex breakage function generated until now is the one that relates the particle size population of the parent particle, with the daughter generation, taking into account their mineral composition and the subsequent grain liberation after a comminution action (King and Schneider, 1998; King, 2012). This function is denominated as the quadrivariate breakage function (Figure 10). In this case, the daughter particle arrangement is not only a matter of new size distribution; it is also a new progeny of hundreds of combination of sizes and grades (King, 1990).

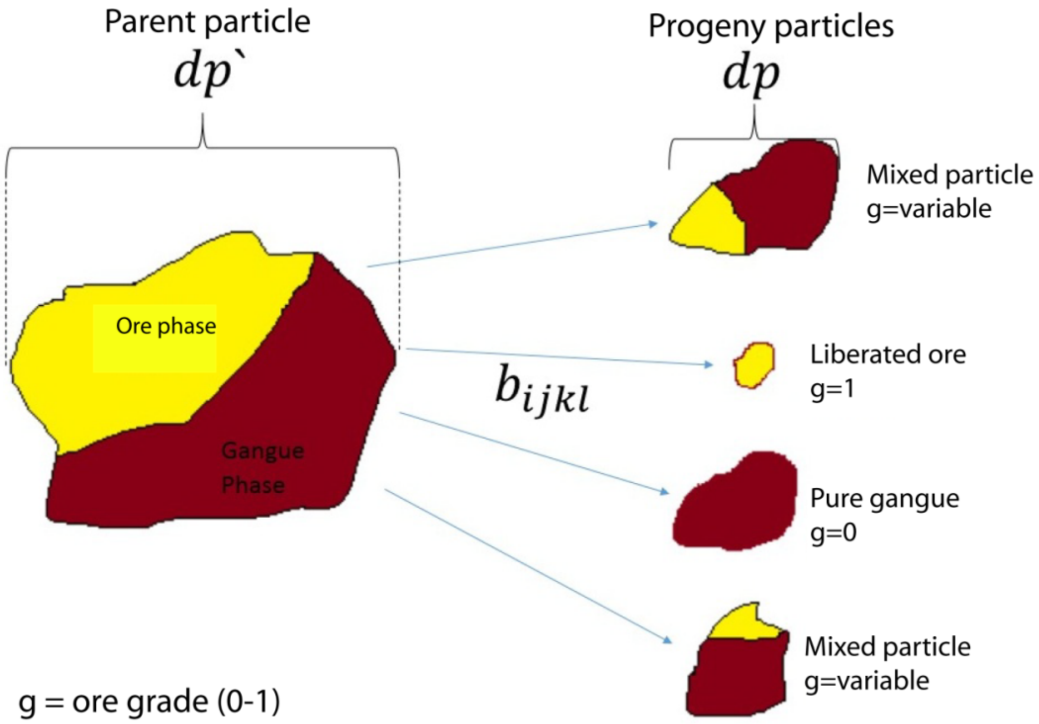

Figure 10. The quadrivariate breakage distribution function not only describe a size progeny population but also their mineral composition in terms of grain liberation (Andrew and Mika, (1975), where g=ore grade.

For HPGR modeling, the Whiten (1972) approach is widely used; however other models have been applied. The quadrivariate breakage function was conceived for milling process, and there is no author that has applied this approach to HPGR particle size distribution prediction.

Every single breakage function has also its own methodology to determine their parameters. The empirical model based on progeny population, as its name indicates, uses empirical values to determine the function constants. For milling models, it is usual to produce mono-size samples in a lab-scale tumbling mill, in ideal condition, and using back-calculation techniques to find the model values (Austin and Luckie, 1971; Austin and Luckie, 1972. The ultra-fast cell load is used the Tavares and King (1998). Benzer et al (2011) used a piston press to determine particle bed mechanism under high compression conditions, but it was not used to determine breakage function parameters. It is often used in this type of devices to used reverse algorithm calculation, using experimental data, to find the model parameters.

3.5.2. Austin model and their approaches

Several models are able to describe de motion and comminution in the HPGR. An earlier approach is the one developed by Austin for roll crushers (Austin et al., 1980), and then adapted to high pressure grinding rolls (Austin et al., 1993). In their work, different copper ores and coals were used to determine the parameters for the different functions of the model. The approach of this model is based on receiving a controlled feed rate with sieves size larger than the gap setting. Then, at any position in the rolls, they act on the large feed particles which are too big to move down further. When these particles are broken, a set of fragments are produced. The larger fragments will be broken again, while the fragments much smaller than the gap will pass down. This is a model applicable to double smooth roll crushers, so it should be modified in order to attempt to use it for high pressure grinding rolls (Figure 11).

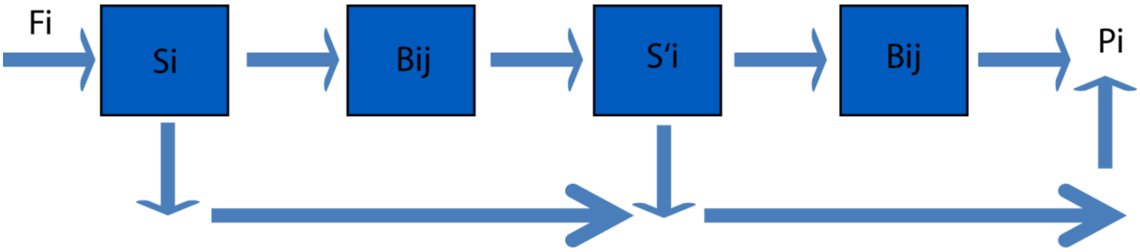

Figure 11. Austin mode presented in block scheme. It was conceived for roll crushers but it is also applicable to HPGR.

The selection function S_i could vary into S'_i, according the particle size distribution evolution after first step of breakage (which is represented by B_{ij}). In the case of the Austin model, there is no change on the breakage function parameter B for each stage of comminution. This model was fully detailed in the conference paper (Austin and Trubelja, 1994). However, some key parameter of comminution in this kind of device, as the specific pressing force, was definitely introduced into de the model by Schneider et al (2009). The selection function, in this case, discriminates the particle sunder single or bed compression, being influenced by the specific pressing force. Two breakage functions embedded into the model. First, the Whiten (1972) and Whiten et al., (1979) approach, but having six parameters, including the nipping and compression breakage, but for simplification purposes, these parameters were considered as equals. The truncated Rosin-Rambler-Bennet Equation breaking approach is also used in this mode (Broadbent and Callcott 1956), mainly due to the reduced number of function parameters, but the author does not ensure the capability on the usage of this function to other kind of ores.

3.5.3. Morrel model and their approaches

The edge effect is a second region of compression breakage, firstly introduced by Morrel et al. (1997) and further developed by Torres and Casali (2009). Basically, three stages of milling are described, one of selection and the last one of mixing stages. Then, three stages of comminution were defined by the population balance model: (a) a Single Particle Compression zone where the comminution is performed preferably by contact Roll-Particle-roll; (b) a Particle bed Compression zone where the interaction between crushed particle coming from the pre-crushing stage and c) the edge effect crusher. These first and the second stages are divided by a classification function (Figure 12).

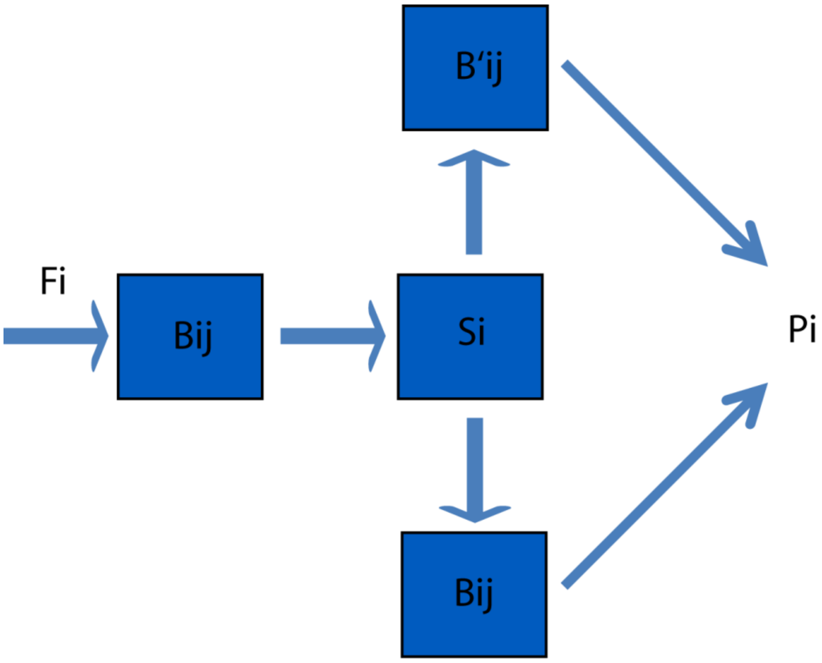

Figure 12. The three stages of comminution: a pre-crushing stage is foollowed by two simultaneous comminution stages, the bed particle compression and the edge effect (Morrell et al. 1997).

In general terms, the differential feed mass is classified in the coarse particles, larger than a critical parameter dependent of the nip angle and the fine particles. These particles are affected by single particle compression action and are broken instantly due to rolls compression. Subsequently, the progeny particles join with the undersize particles category forming a new feed that enters to the Particle bed Compression and the one that are affected by the edge effect.

In the case of the Morrel et al. (1997) model, the breakage function of the bed compression and the one of the edge effect are different, thus the number of parameter are considerably increased.

The differences of the Torres and Casali (2009) model compared with Morrel et al (1997) model lies on the bed compression calculation, in which it was introduced the edge effect by means of the scale-up of the specific rate of breakage that depends on the differential pressure over the roll length, producing the differential particle size distribution on the edge (Figure 13).

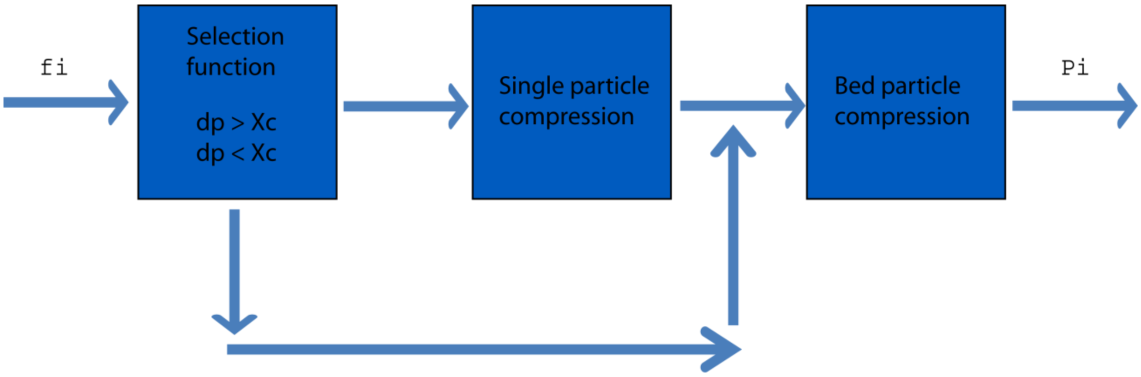

Figure 13. Torres and Casali (2009) model block scheme, where the single particle compression is followed by a bed compression condition.

From the mathematical point of view, the Torres and Casali (2009) based their calculation of the bed compression condition on the batch grinding equation kinetic equation, which was solved analytically by Reid (1965).

CHAPTER III

Materials

Methods

4. MATERIALS

4.1. Materials description

This study uses three types of materials (Figure 14): two tungsten ores, one of them from the Mittersill mine (Austria) and other one from the Barruecopardo tailings (Spain), and one tantalum ore, from the Penouta mine (Spain). They have been selected based in two main criteria:

A) They should be different from the mechanical point of view, in order to observe and compare the response of them under controlled comminution action, and to find patterns or behaviour that characterizes them.

B) They must be constituted by different minerals, with the aim to generalize the model to all types of materials.

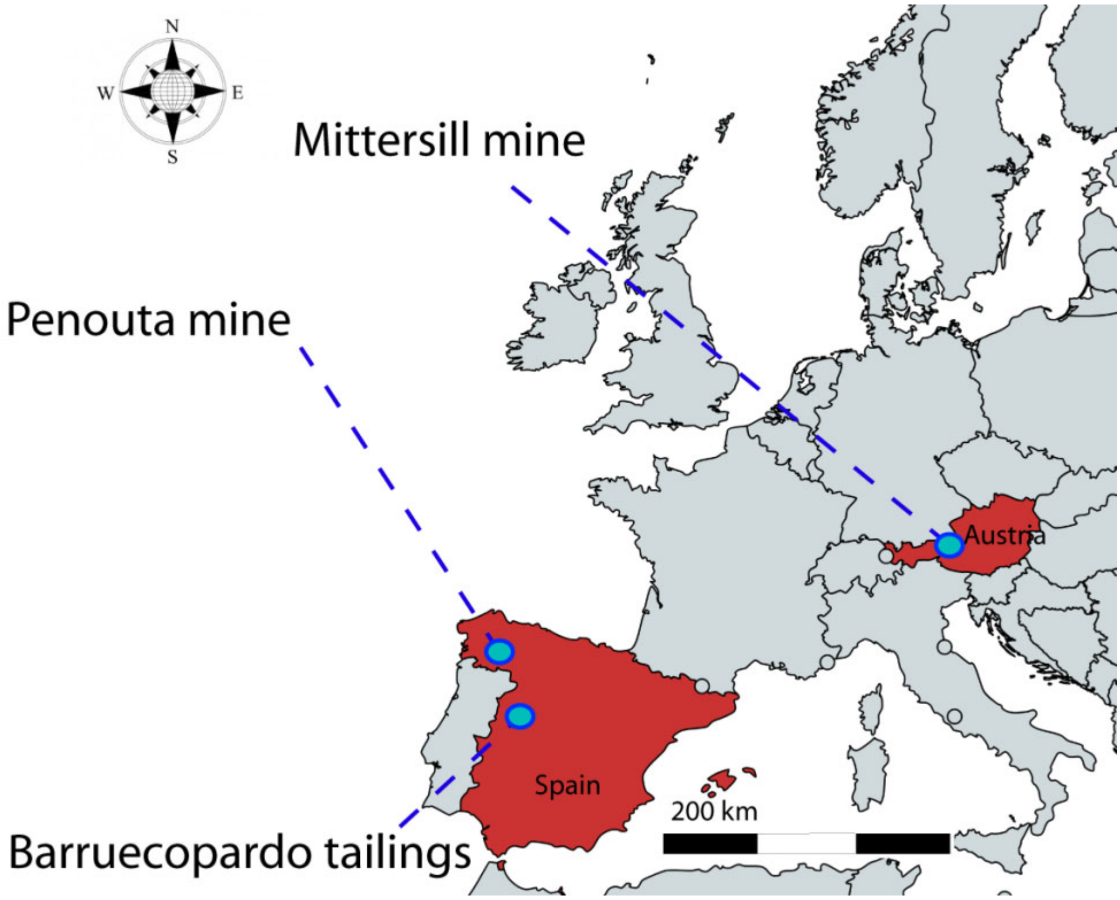

Figure 14. Geographical situation of the samples used in this study.

4.1.1 Tungsten ores

In the case of tungsten mines, ore deposits are mainly constituted by two types of rocks: veins and greisen deposits are mainly hosted in granitic rocks, whereas ores from skarns and strata-bound metamorphic deposits are hosted in calc-silicate rocks.

Skarn deposits accounted for about 30% of world tungsten production in 1986 (Werner et al., 1998). Scheelite is the principal tungsten ore in these deposits. There are a high number of skarn deposits or occurrences in Western Europe (Cheilletz et al., 2005). This strata-bound deposit also occurs in volcano-sedimentary sequences related to submarine volcanism (Holl, 1979). The distribution of the mineralization is strongly controlled by bedding in the host rocks, which usually has been affected by later mobilization. Wolfram ore is scheelite that often is accompanied with molybdenite and other sulphides. Tungsten also occurs as wolframite.

Scheelite from Mittersill

The first selected material was a tungsten-rich calc-silicate, with scheelite as a main ore. This material was extracted from a mine located of the Felber valley, 9 km south of the town of Mittersill, Austria (Figure 15). This site is considered the largest tungsten deposit in Europe and ranks among the largest deposit of the world (Thalhammer et al., 1989; Eichhorn et al., 1997). The host rock consists in a dark-green amphibolites form up to some m-thick intercalations with felsic gneiss of the poly-metamorphic volcano-sedimentary Habachs series (Holl, 1979; Raith and Schmidt, 2010; Figure 2), with numerous tungsten-rich quartz veins (Eichhorn et al. 1997). In addition, other ore minerals can be found in this deposit: powellite, wolframite, molubdenite, tungstenite, pyrrhotiete, pyrite, marcasite, pendlandite,sphalerite, galena, native Au, among others. Scheelite is found as a fine-grained (diameter of the grains less than 350 μm) enclosed in fine grained quartzite with mosaic texture (grain diameter less than 1000 μm) (Holl, 1979). As a metamorphic rock, it is a foliated type, giving it an anisotropic characteristic, having variable physical-mechanical properties in different direction (Özbek et al., 2018)

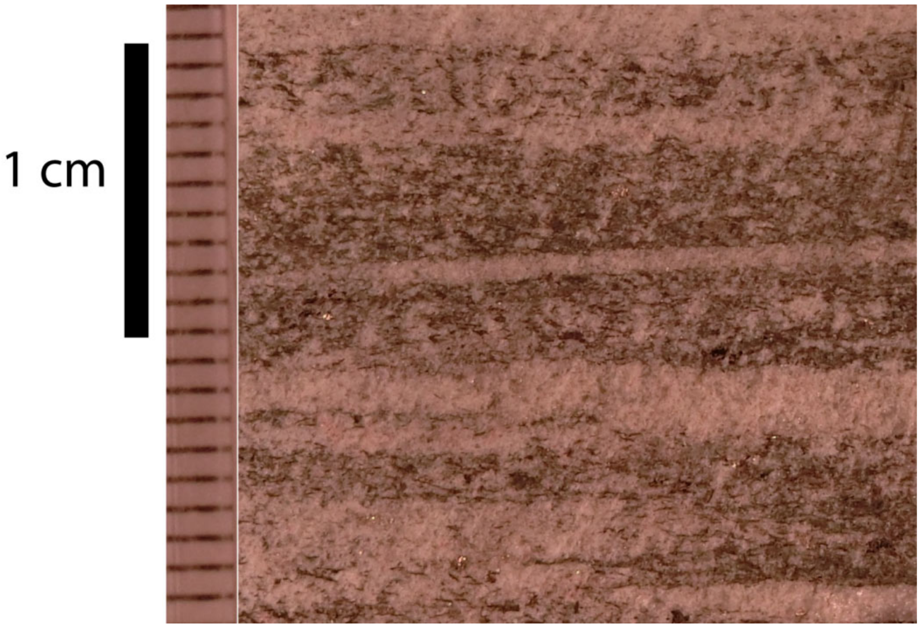

Figure 15. Texture of the cal-silicate rock from the Mittersill mine.

The deposit was discovered in 1967, but it was exploited from 1975, as an open pit and underground mining from 1976. The scheelite flotation plant started in the same year, 1976. Due to harsh climatic conditions, mining in the open pit was seasonal, and through the years it became complete underground. Another reason to be underground is due to its location, close to a national park. All auxiliary infrastructure as change room, workshops and offices are also located underground. By the end of 2008, the mine had produced 9.6 Mt of ore with 0.4-0.5 wt% $W0_3$ (Raith and Schmidt, 2010). Now it is exploited by Wolfram Bergbau und Hütten AG and they extract the scheelite ore in the state-of-the-art underground mine. The process is carried out in their processing plant, 3 km away from the mine site.

Scheelite from Barruecopardo

The second tungsten ore used in the experiments was a granitic material from the tailings of the Barruecopardo mine, located in the West of Iberian peninsula, near to Salamanca city, Spain (Figure 14). Barruecopardo was one of the most important tungsten deposits in Spain; it has been extensively exploited from 1912 to 1983, mainly marked by armed conflicts. The I World War boosted tungsten prices, reaching more than 30 tonnes production in 1917. The II World War reactivated this mineral exploitation. In the fifties, the war in Korea promoted the prices increment of this metal. Nowadays it is considered to restart the mining activity as a low-cost mining project, carried out by Ormonde Mining plc.

In the area there are mainly two groups of rocks: granitoids, and sedimentary rocks roughly metamorphosed. Schists extending around Barruecopardo have been attributed to the Cambrian and Ordovician, although, in the absence of fossils, age is not well established. These rocks consist of gray, compact, and with abundant pelitic intercalations quartzite, below which is a very monotonous series of dark schists. The degree of metamorphism of these rocks is highly variable. In general, they belong to the biotite zone, but may have been deeper changes according to their proximity to granites. Therefore, around the plutonic rocks they have been developed halos contact areas pertaining to andalusite-cordierite and sillimanite-K-feldspar, whose isograds are more or less parallel to the contact with the plutonic rocks. On the basis of this metamorphic series, 13 km east of Barruecopardo, is a complex of high metamorphic grade, consisting of fine-grained banded gneisses and ocellar gneisses, that by tectonic considerations and by comparison with existing similar rocks in the northwest of Spain, they have been attributed to the Precambrian.

The deposit is a Wolfram greisen-type ore that consists mainly of granitic rocks with scheelite, wolframite, pyrite, abundant arsenopyrite and minor amounts of chalcopyrite, molybdenite and cassiterite (Alfonso et al., 2016). This is constituted by sub-vertical quartz veins disposed in parallel intra-granitic bands. These minerals appear in the veins and on the borders of a granite body (Pellitero, 1981; Muerciego et al., 2011). Scheelite can be distinguished based upon fluorescence colour, generally under 254 nm UV (Figure 16).

The material used in this study belongs to the ancient tailing that remains from the former exploitation. Due to the poor concentration techniques performed in this site, the tailing has a strategic interest, not only for its tungsten content, furthermore by their composition suitable for use as glass ceramic materials (Alfonso et al., 2017). The stocked material is composed of around 5 Mm^3 of waste material, originated from the formers processing plant. The material is currently used as arid, being a local supplier for construction raw material. In the quarry facilities, the material is split in different sizes classes and they are sold as sand or gravel, depending on the market needs.

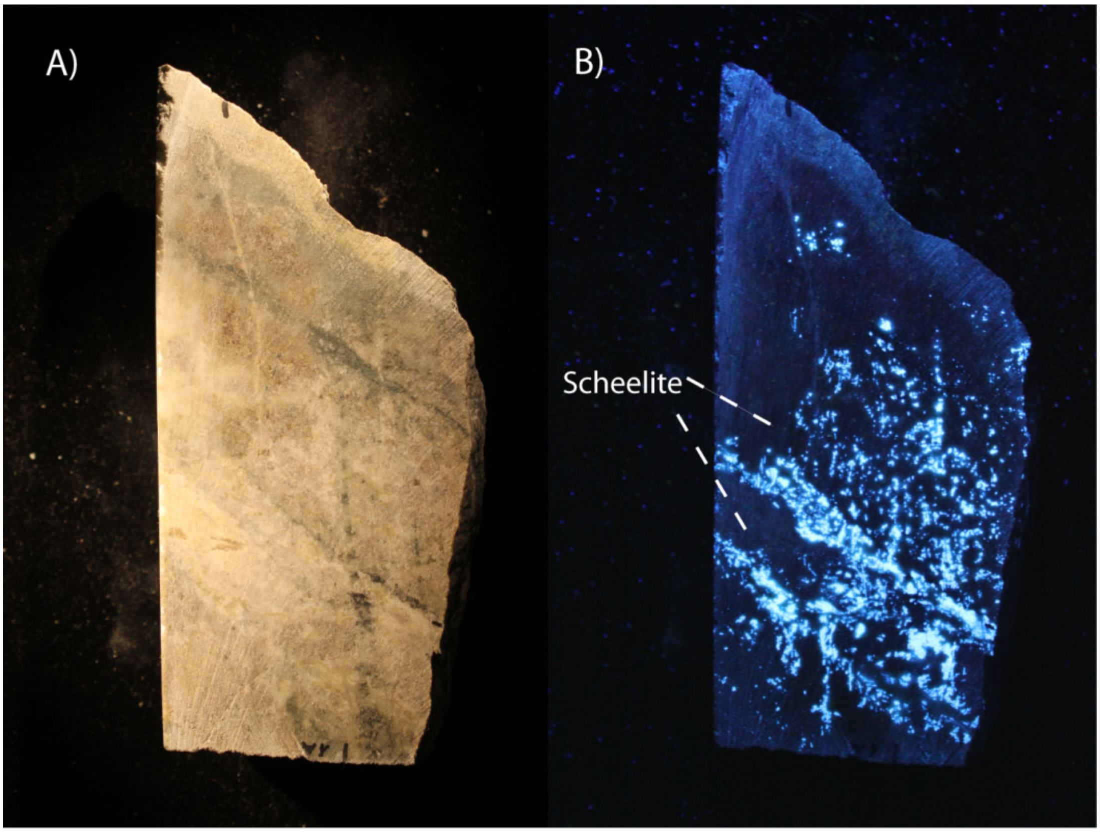

Figure 16. Calc-silicate matrix with scheelite content. This mineral reacts under short UV light (256 nm). A) Piece of calc-silicate under normal light, B) Same piece, under UV light.

Due to the Barrucopardo material composition, mainly granite, and depending on its abundance on quartz or feldspar, the response to comminution should be different compared with the calc-silicate material, being of a great interest for this study.

4.1.2. Tantalum ores

The tantalum ore was extracted from the only active mine in Europe that exploits this metal. The Penouta mine is located in the Penouta village, municipality of Viana do Bolo, Ourense, Galicia, northeast of Spain (Figure 14). It is a Sn-Ta greisen-type ore deposit where mineralization occurs as in quartz veins related to the greisen formed in the surrounding leucogranites or also called albite granite (Lopez-Moro et al., 2017; Alfonso et al., 2018).

By Exploiting since Roman times to extract Sn, this site began to be important from 1965. It was an open pit exploitation of the leucogranite unit. In 1983 the exploitation finished due the low price of metals and the low recovering degree of Sn, about 30% of the total tin content.

Although the tantalum grade of this deposit is not high, it is considered that it will become the main producer of Ta of Europe. This deposit is property of the Strategic Minerals Spain. In 2018, a pilot plant started to work and the construction of the installations to begin the processing activity was carried out. Nowadays, the mine has the environmental authorization and the exploitation permission, type B, with resources of about 12 millions of tonnes (www.strategicminerals.com).

The Penouta deposit is composed of leucogranite hosted mainly in highly metamorphosed rocks, including banded migmatitic gneisses and garnet-bearing schist, corresponding to the Viana do Bolo series (Figure 17). It is located in the Ollo de Sapo anticline and is considered of Lower Cambrian age (Mangas and Arribas, 1991; López-Moro et al., 2017).

The leucogranite of the Penouta texture is medium to fine grained (Figure 4b). The inequigranular characteristic is due to the presence of relative large grain of quartz, 1 to 2 mm in size, included in a matrix of other smaller grains, most of them lower than 500 µm. There are constituted by quartz and muscovite, with accessory biotite. Several minerals that may contain Ta are present in submillimeter-sized crystals, mainly cassiterite, columbite-tantalite, rutile and microlite. This leucogranite usually is altered by hydrothermal fluids, with albitization and muscovitization. Although it is classified as leucogranite, albitization replaces a significant amount of K-feldspar, and the resulting rock is an albitite. Occasionally the alteration is so strong that kaolin is formed. Previous analyses facilitated by Strategic Minerals indicate a grade in this part of the deposit of 50-75 ppm Ta_2O_5 (Llorens González et al., 2017; Alfonso et al., 2018; Hamid et al., 2018).

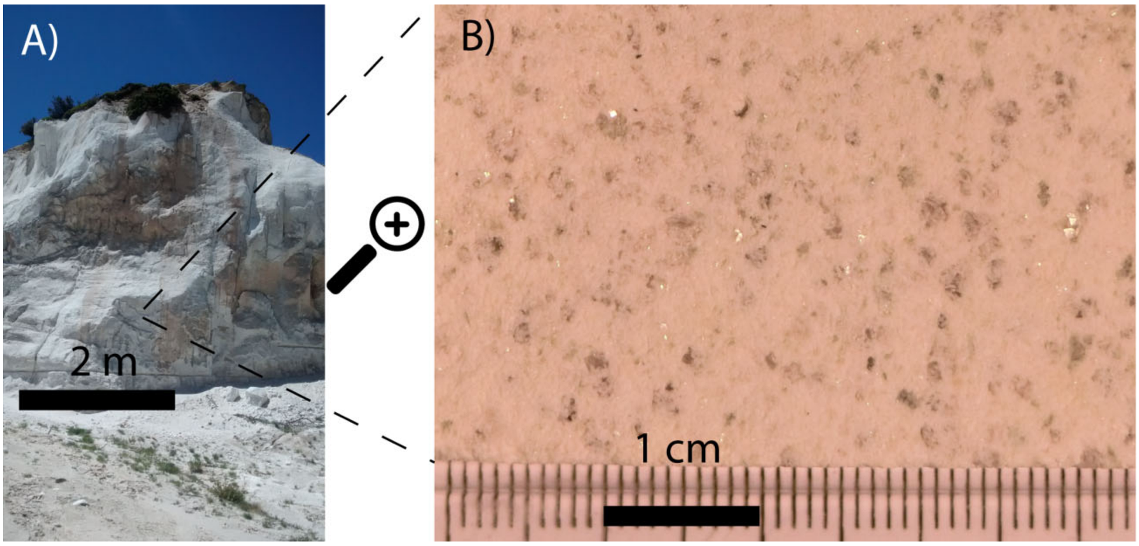

Figure 17. Leucogranite from the Penouta mine. A) View of the deposit B) Texture of the leucongranite

From the mechanical point of view, due to its high degree of alteration, the albite leucogranite is a soft rock, brittle and inconsistent. In terms of liberation, the cut-size point was determined in 250 µm (Ahmad et al., 2018), reaching 84 wt% of liberated cassiterite and 65 wt% of liberated columbite-tantalite. The columbite-tantalite also presents its characteristic columbite core surrounded by a rim tantalite (Figure 18).

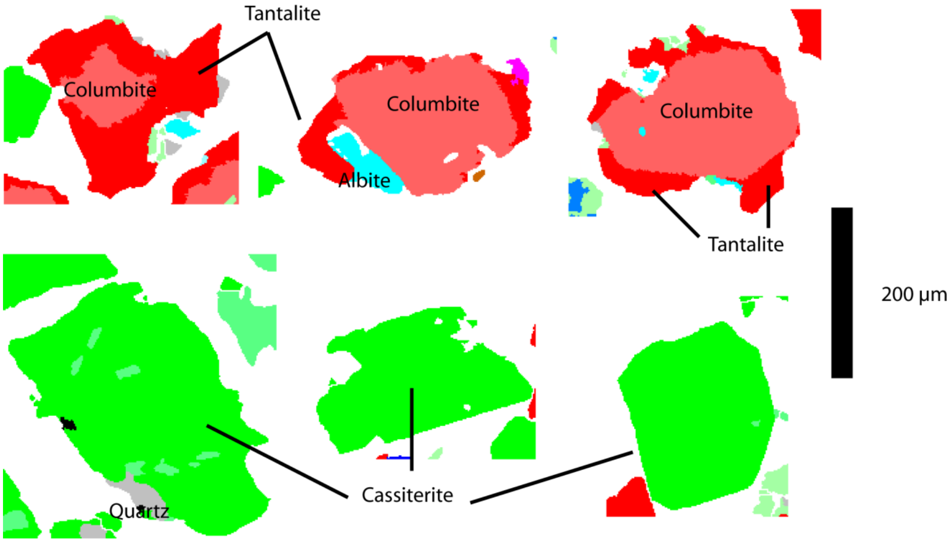

Figure 18. Mineral liberation analysis image showing the aspect of the ore minerals presented in the Penouta materials (Hamid et al, 2018).

4.2. Sampling

The sampling campaigns were done between the beginnings of the year 2015 until the middle of year 2016.

In the case of the Mittersill, the sampling was done in a survey on 2016. A delegation of the OptimOre project carried out the sampling. In order to have an overview of the process, the processing plant flowsheet was provided by the company and it is presented in Figure 19. The mining method is by means of sub-levels, using blasting to extract the rock. The material is transported from the underground levels to the processing plant facilities in conveyor belts. The primary crushing stage is fed with this material, and the product is storage, for further feeding of the Metso ball mill. The company staff prepared a pallet with around 400 kg of calc-silicate coming from the mill feed stream, showed in the point A and B of the Figure 19. The particle size distribution of this material varied from a few microns to 60 millimetres. The rest of the flowsheet correspond to the ore concentration process, which is done by means of froth flotation system.

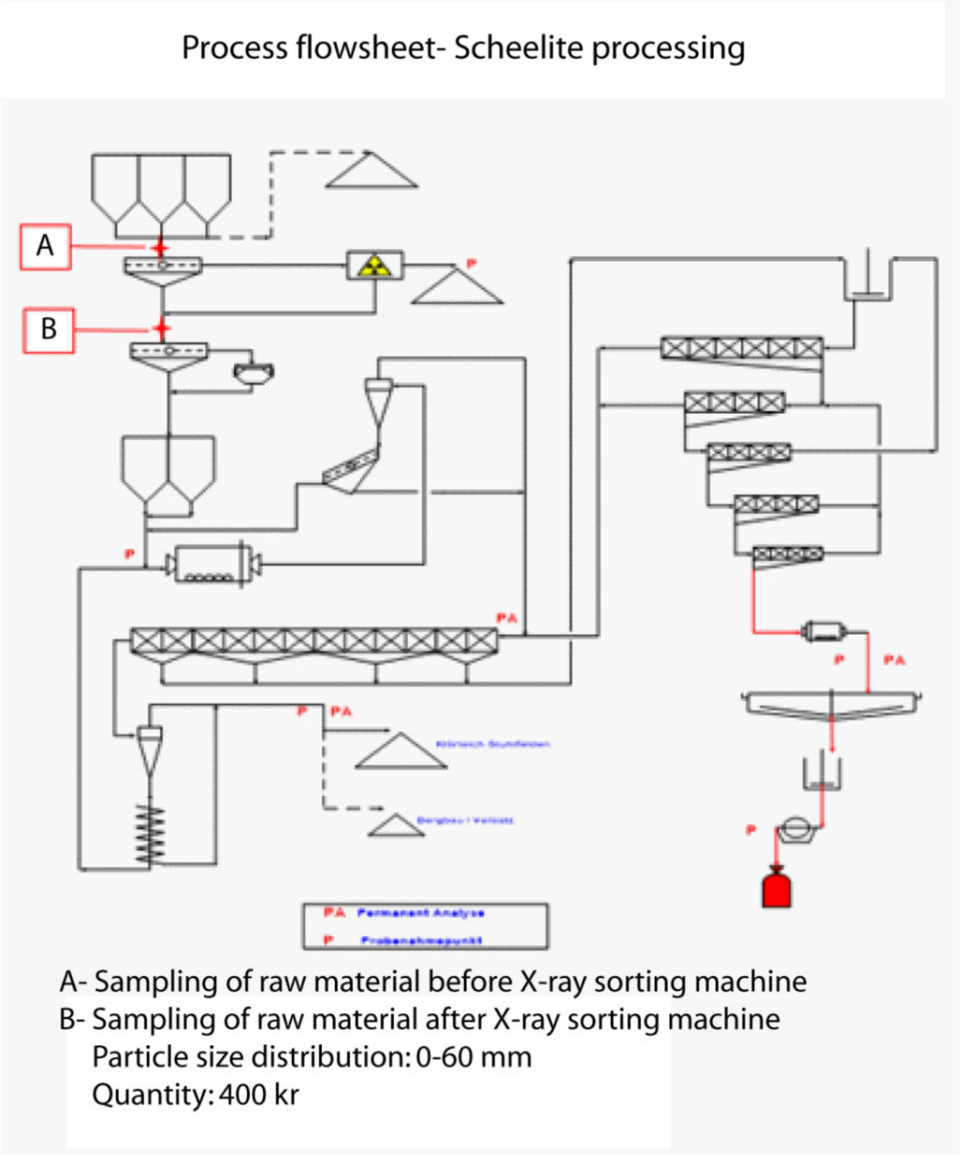

Figure 19. Mittersill plant flowsheet, showing the sampling location. The study uses material from the location B.

The sampling in the Penouta mine was carried out in different stages. The early one was done in the middle of 2015, but it was repeated several times in 2016. Nowadays, the main processed resources by the company is found in the ancient tailing (Figure 20A). Thus, it is not necessary to carry out comminution process, only recovery using gravity and magnetic separators. However, it is planned to start the exploitation of fresh material (Figure 20B) in the year of 2020. This is one of the reasons to perform the sampling in the main deposit area (Figure 20C), for future evaluation of the comminution using HPGR.

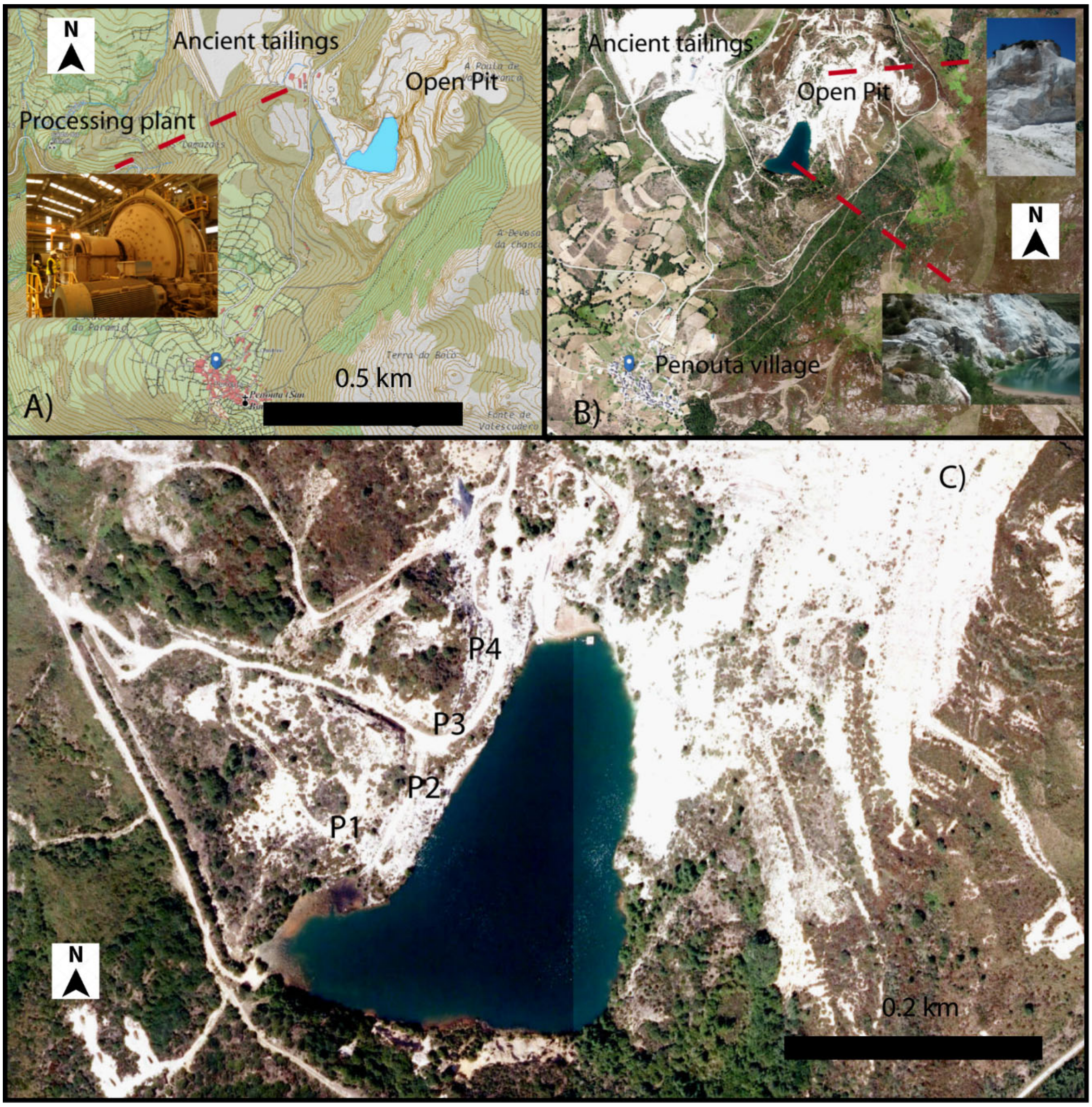

Figure 20. Geographical situation of the Penouta mine. A) Vector based map with the orographic characteristic of the site, showing the location of the ancient tailing and the processing plant. B) Orto photo PNOA 2017 type (IET, 2019), showing the open pit. C) Sampling point in the exploitation front.

For the test and experiments with HPGR, the samples have to accomplish some requirements, from its nature point of view: material that needs to be comminuted. A fresh material from the open pit, despite it has to be previously crushed, is the correct one for being used in experiment with HPGR. For sampling, the mining company provided a backhoe, thus, the material was extracted from different points at different height of the exploitation bank (Table 2). After that, five pallets of 500 kg each one, full of this extracted material, were sent to the university facilities.

Table 2 .Coordinates of the sampling point of the Penouta material.

Sample	COORD_X	COORD_Y
P1	663778.4	4672007.7
P2	663789.7	4672022.0
P3	663797.5	4672041.7
P4	663799.9	4672066.1

The Barruecopardo tailing is currently exploited as a quarry, and marketed as arid for construction. The quarry is located 2 km to the south of Barruecopardo town, Salamanca, Castilla y León region, near the border with Portugal. The former processing plant was placed to the west of the main exploitation site, where now there is a pond (Figure 21).

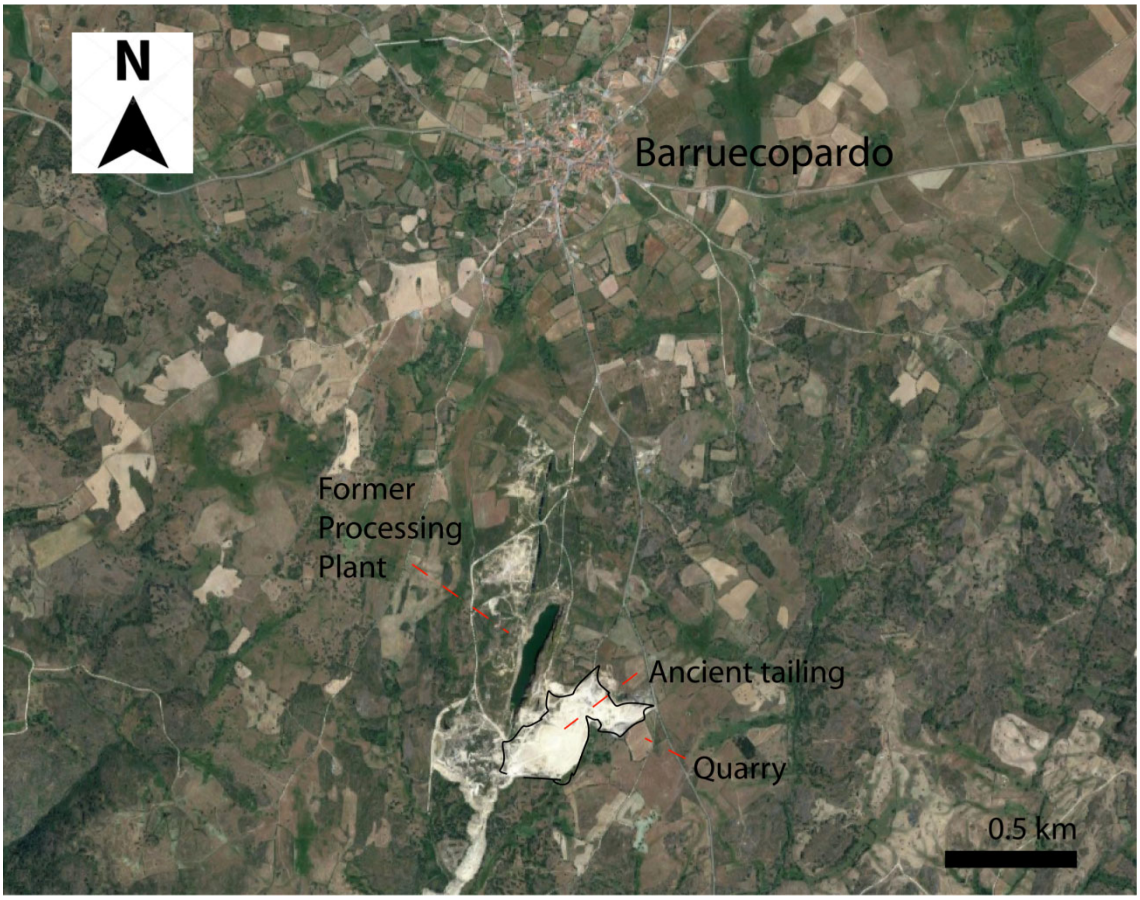

Figure 21. Geographical situation of the Barruecopardo tailings.

The material is taken from the slurry deposit near of the former processing plant (Figure 22A) by the quarry stuff. The tailing material is transported to the classification screening (Figure 22B) where the material is split in different size classes, maximum less than 2 mm diameter approximate (Figure

22C). Several pallets with big-bags of 1 m^3 were taken from the quarry and sent to the University laboratory. As each test needs more than 250 kg of material, in order to be representative, the exact quantity of material was prepared and packed in drums to be sent to Germany (Figure 22D). The chosen sizes were +9-11 mm; +11-14 mm, +14-16mm, +16-19 and 0-19 mm. The company Köppern manufacturer received the samples to be tested in their pilot plant with industrial scale HPGR (Figure 22E). A total of 1300 kg were sent for tests (Table 3).

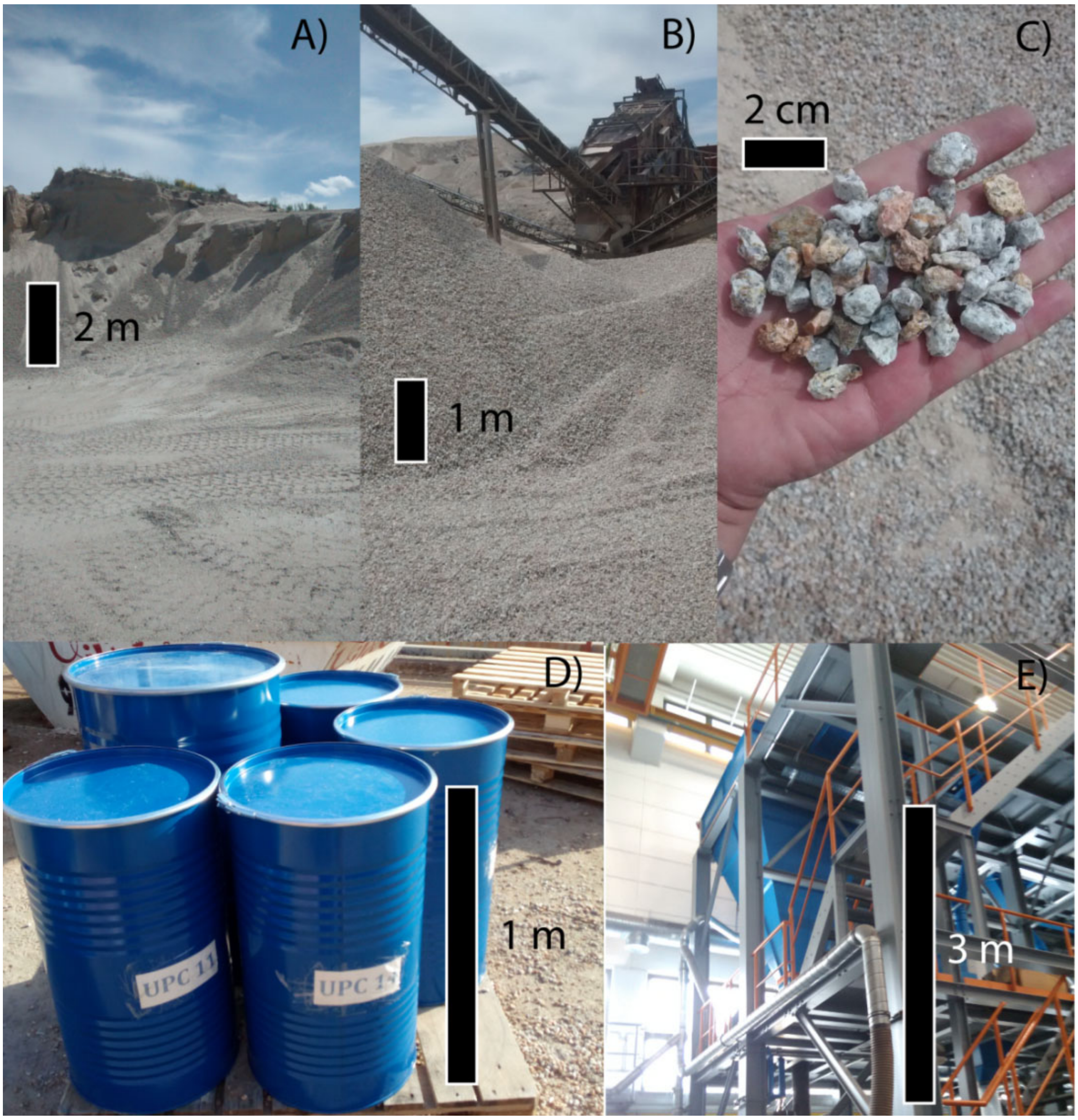

Figure 22. Sampling process in Barruecopardo. A) View of the ancient tailing, B) Quarry machinery, in this case, the screening. C) Top-size of the tested material. D) Material packed in drums. Each one is used for only one test. E) Pilot plant in Freiberg University, with an industrial scale HPGR.

Table 3. Relation of drums denomination, size range and quantity of material to be tested in Freiberg.

Sample number	Size range [mm]	Quantity [kg]
0 to 5	0-3	250
6 to 10	3-8	250
11 to 15	8-14	250
16 to 20	14-22	250
21 to 25	0-22	250
26 to 28	0-3	50
Total sampling quantity [kg]		1300

5. METHODS

5.1. Methodology description

The methodology was divided in different stages, all linked each other. After sampling, there was a material characterization and lab-test works. The aim was to relate mineral association with the mechanical behaviour when the particles break under previous selected pressing conditions, which is the main comminution action in a HPGR. The description of this mechanical behaviour of the material was done through the breakage distribution function; an innovated procedure for function parameters determination was developed, the piston die test. A simultaneous stage was to probe the breakage mechanism under pressing conditions by means of experiments in lab-scale environment. Once the model had been determined and the model function parameters were defined, the model generation was performed using the mathematical tools with different software, the new parameters generated and the recorded operative conditions from the lab-scale stage. The validation step was performed with a third different material, in different conditions, using an industrial scale HPGR (Figure 23).

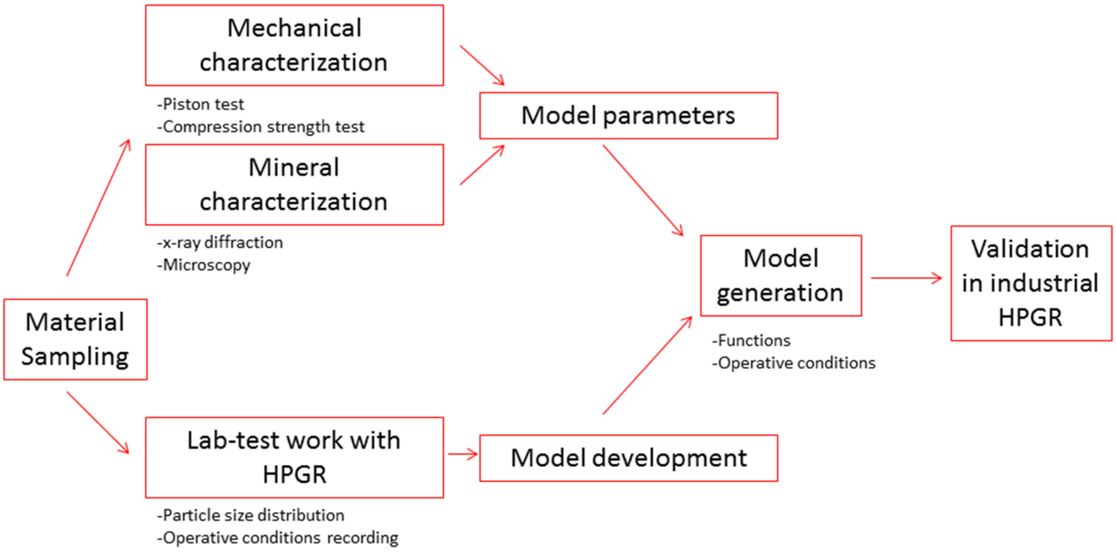

Figure 23. Methodology scheme used in this study.

It is also relevant to explain in detail the characterization methodology, since it was done simultaneously and for the inlets and outlets of the mechanical tests. The samples were seen under microscopy and they were also analysed based in previous works. After the test, the particle size distribution was determined, and several size ranges were also analysed with x-ray diffraction, in order to relate mechanical parameter with their mineral composition for different particles size classes (Figure 24).

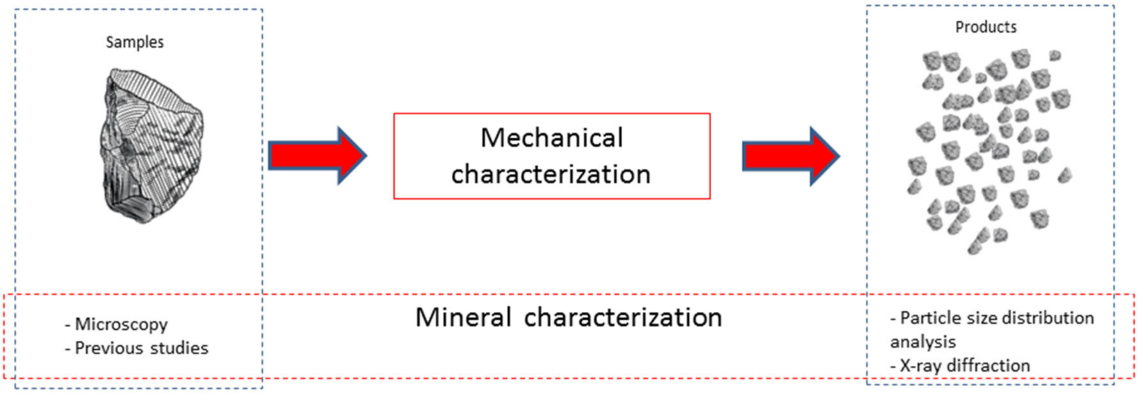

Figure 24. Zooming of the characterization of the samples

As the piston die test (explain further) is executed under high compression condition, thus, the x-ray diffraction was performed on the different size ranges, in order to observe composition variations with the particle size distribution. The selected size ranges were -0+0.2, -0.2+0.4, -.0.4+0.7, -0.7+1.0, -1.0+2.0, -2.0+4.0, -4.0+6.3, -6.3+8.0, all sizes in mm.

5.2. Mineral characterization

The mineralogy of the different samples was determined by X-ray powder diffraction (XRD). The spectra were measured from powdered samples in a Bragg-Brentano PANAnalyticalX'Pert Diffractometer system located at the Centres Cientifics i Tecnològics de la Universitat de Barcelona, Spain (CCiT, UB) (equipped with a graphite mono-chromator, automatic gap, Kα-radiation of Cu at $\lambda = 1.54061$ Å, powered at 45 kV and 40 mA, scanning range 4–100° with a 0.017º 2θ step scan and a 50 s measuring time). Identification and semi-quantitative evaluation of phases was made on PANanalyticalX'Pert High-Score software. The semi-quantitative determination was based on the Rietveld (1969) method.

Textures were observed by optical and electronic microscopy. The equipment was a Hitachi 1000 tabletop electron microscope with an energy-dispersive X-ray spectrometer (EDS) provided by the Hitachi company. This equipment is located at the Departament d'Enginyeria Minera, Industrial i TIC, UPC.

5.3. Single compression strength test

To define the specific pressing force (Fsp) in which the materials are single compressed, a series of single compression strength test were done. The standard UNE-EN 1926 (1999) defines the relation between the rupture load and the transversal surface before the test. 25 cm^2 probes were cut and dried until 70 ªC (± 5ªC) with a constant mass. Once the probes are dried, they are kept in 20ªC until reach a thermic equilibrium. The assays have to be done before 24 hours. The transversal surface is measured and a load from 1 MPa is pressed until reach first rupture. Two materials were tested under this methodology, the leucogranite from the Penouta mine (Figure 11) and the calc-silicate from the Mittersill mine (Table 4)

Table 4. Characteristics of the test pieces for the standard single compression strength measurements.

Material	Sample Number	Surface (cm^2)	Weight (g)
Leucogranite	1	25.0	115.6
	2	25.0	115.7
	3	24.3	139.8
	4	23.9	122.1
Calc-silicate	1	17.0	54.2
	2	16.5	50.4
	3	16.2	46.6
	4	16.4	47.0

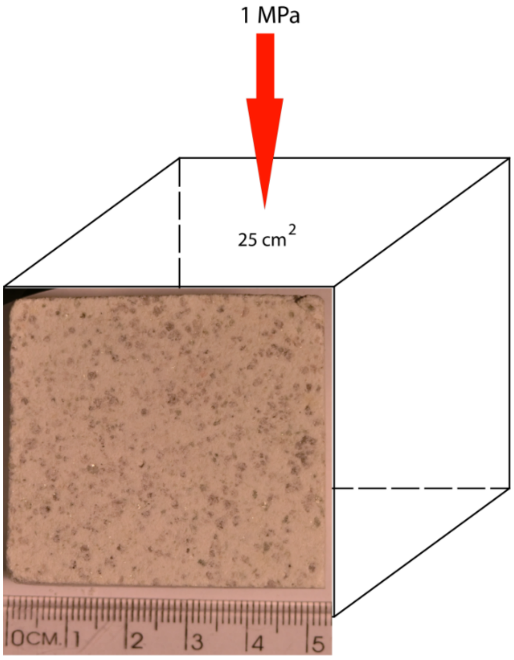

Figure 25. Leucogranite cube sample for single compression strength test.

5.4. Piston die test

The comminution in rolls pressure environment mainly occurs in compression conditions. Thus, the breakage distribution function should be related to the mechanical response of the material under different specific pressing force (Fsp). It is also relevant to determine the material response to comminution in different operative forms; single compression and bed compression.

The piston die-test is presented to characterize the material in terms of mechanical response to compression by means of breakage distribution determination. The test uses an apparatus which was manufacturer in the mechanical department of the UPC, especially designed for this study. It consists in a hydraulic press which runs in a pressure range of 0–12 tonnes. This test is executed with different dimension pistons, for scaling purposes: when is for a laboratory device modelling and when is used for industrial scale HPGR. One of the pistons corresponds to a 40-mm diameter and 50 mm sleeve, giving and effective volume of 65 cm³ (Figure 26A). The other piston has larger dimensions, reaching 70 mm diameter and also 50 mm sleeve. This piston has an effective volume of 192 cm³ (Figure 26B).

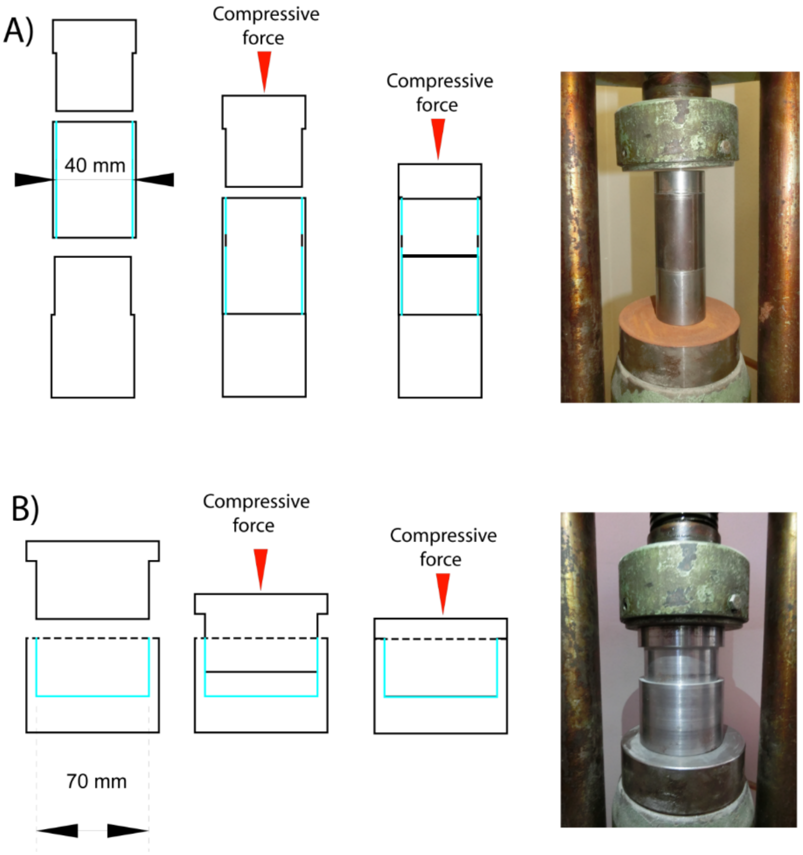

Figure 26. Two piston dimensions were used for breakage function characterization A) 40 mm diameter x 50 mm sleeve and B) 70 mm diameter x 50 mm sleeve.

Previous to tests, there is a sample preparation stage. The raw material coming from the mine site was previously crushed by a KHD Humboldt Wedag double toggle jaw crusher (OSS 12 mm; Figure 27A). After that, the crushing product was screened and classified into narrow particle size fractions (Figure 27B). For the 40 mm diameter piston, the altered granite and the calc-silicate were used (Table 5). In the case of the 70 mm diameter piston, a granite material was tested (Table 6).

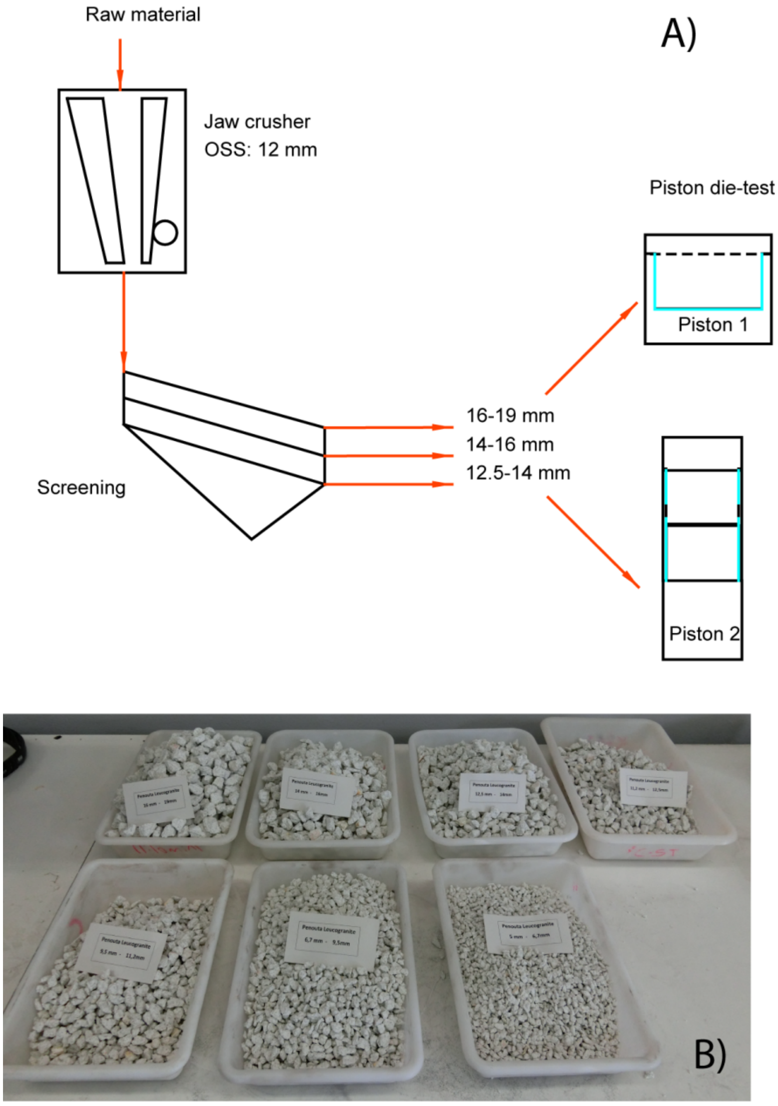

Figure 27. A) Sample preparation for piston-die test. B) Mono-size range particles of the Penouta material, designated to compression characterization.

Regarding the specific pressing force, in the case of single particle compression condition, a maximum Fsp was determined, and is when the single particle collapses and breaks. For bed particle compression, the piston die test was executed in the same maximum Fsp, but after several discoveries about the relation between Fsp and the breakage function parameter, the test was design with different specific pressing force ranges. These differences are reflected in Table 6, compared with

Table 5. Table 5 shows single compression and bed compression conditions. Table 6 shows bed compression using different specific pressing forces, furthermore the single compression condition.

Table 5. Material size and quantity for the mechanical characterization using the 40 mm diameter piston.

Conditions	Mesh Size (mm)	Granite (g)	Calc-Silicate (g)
SC	2.0–4.0	42.2	39.4
	4.0–4.8	50.2	69.9
	4.8–6.7	81.7	11.32
	6.7–9.5	88.2	38.5
	9.5–11.2	141.3	49.2
	11.2–12.5	194	58.3
	12.5–14.0	257.9	63.4
	14.0–16.0	343.8	93.7
	16.0–19.0	489.8	-
BC	0.71–1.0	73	35.6
	1.0–2.0	88.1	88.3
	2.0–4.0	101.7	43.3
	4.0–4.8	86.9	33
	6.7–9.5	90.2	35

Table 6. Material size and quantity (g) for the mechanical characterization using the 70 mm diameter piston.

Mesh size (mm)	Fsp (N/mm^2)			Single compression
	2.5	3.5	4.7	
-4 +3.2	141.4	141.1	138.4	-
6.3 +4	171.9	173.1	162.2	-
-8 +6.3	168.1	174.5	162.9	-
-9.5 +8	151.5	148.7	150.8	-
-12.5 +9.5	159.8	179	162.8	-
-14 +12.5	165.2	164.8	152.6	211.2

The procedure of the test varies depending on the operative condition in which is tested. Thus, for the single particle compression condition, a set of single particles were placed into the piston chamber, one to one. The aim is to have two or few contact points under pressure, between piston surfaces. In order to observe normalization, different set of mono-sizes particles were used (Figure 28A). A force was applied progressively up to reaching a first fracture, indicated by the abrupt fall of the hydraulic oil pressure gauge. The quantity of particles used for the test is presented as a total mass in grams, and represents the moment when the trend of the rupture function stabilizes, so that no more material is needed to obtain this function. For the bed particle compression condition, a group of particles were confined in the piston chamber with several inter-contact points between them and the piston surface (Figure 28B). For this reason, a set of mono-size particles ranging from 0.71 to 4.8 mm were used in the bed compression configuration (Table 5 and 6). Based on the lab-test work in which the HPGR was set with around 0.9 N/mm^2 specific pressing force, bed compression tests were performed with the same pressure range. In the case of the larger piston, the specific pressing force was varied in order to stablish a relation between this pressure parameter and the function parameters.

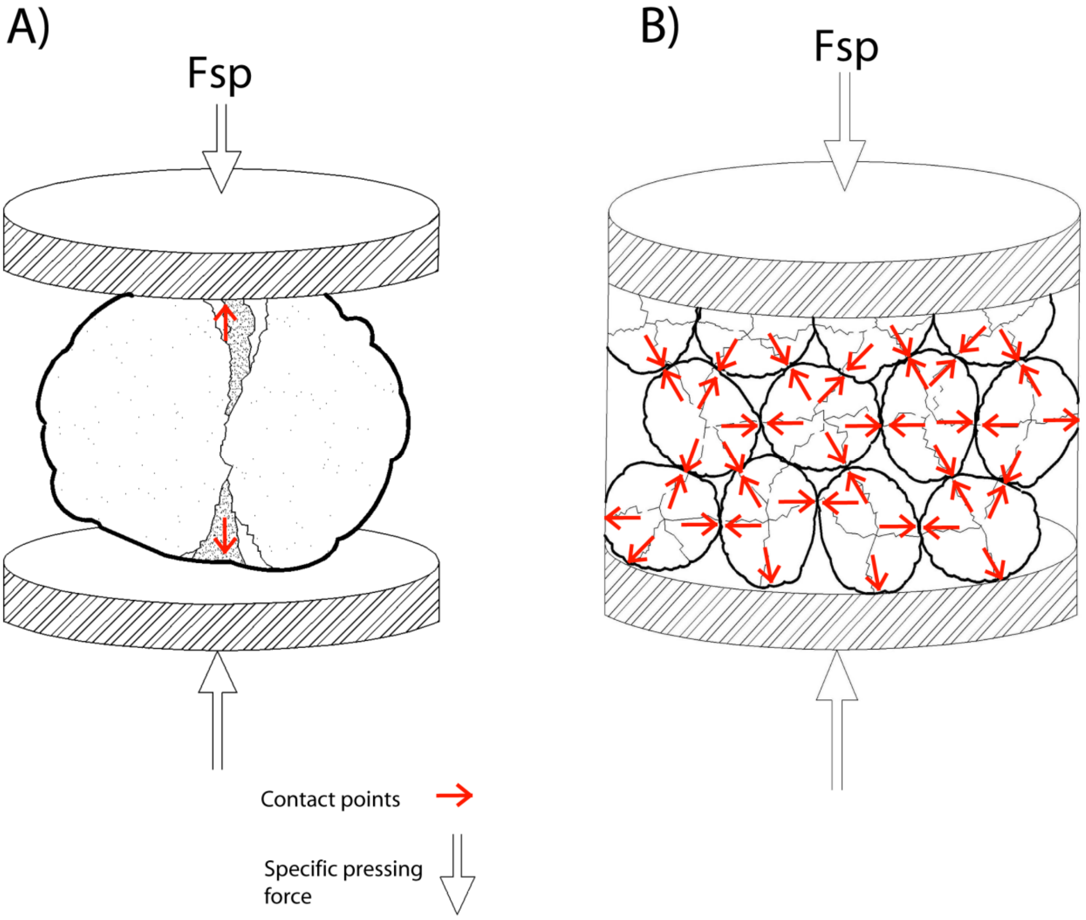

Figure 28. Sketch of the piston chamber were the particles are place to A) single particle compression, with only two contact points or B) bed particle compression, with multiple contact points between particles and the piston surface.

Once the test is carried out, the comminuted material was sieved and the cumulative particle size distribution was plotted against the relative size reduction ratio dp_i/dp_j, where dpi is the progeny particle and dpj is the parent particle. The plotted points were normalized in order to determine the breakage function parameters using the referenced Equations (1) and (2) (King, 2001).

$$B_{ij} = k\left(\frac{dp_i}{Dp_j}\right)^{n_1} + (1-k)\left(\frac{dp_i}{Dp_j}\right)^{n_2} \qquad \text{for } dp_i \geq y_0 \tag{1}$$

$$B_{ij} = k\left(\frac{dp_i}{Y_0}\right)^{n_3}\left(\frac{dp_i}{Dp_j}\right)^{n_1} + (1-k)\left(\frac{dp_i}{Dp_j}\right)^{n_2} \qquad \text{for } dp_i < y_0 \tag{2}$$

Where k, n_1, n_2, n_3 are function parameters and Y_0 is the largest chip size which must be smaller than the parent size Dp_j. It usually takes values of 0.05 m to achieve the ball mill breakage function (King, 2001).

5.5. Test work

The lab-test work was performed at the UPC laboratory using two materials, previously described: the leucogranite from the Penouta mine, and the calc-silicate from the Mittersill mine. The machinery used for experiments was especially designed to have high-pressure environment and the experiments were determined in order to observe the particle behaviour in different operative conditions.

5.5.1. Lab-scale experiments for modelling

Machinery design

The laboratory-scale device is a modified roll crusher adapted with a high-pressure hydraulic system. The mechanical overload protection springs were replaced by two 60 mm internal diameter pistons, which ones were specially design to fit in the former spring site and to obtain high pressure on the floating roll. The pistons were manufacturer at Codina Limited, local company dedicated to mechanical parts (Figure 29A). The hydraulic system was also designed at UPC, but commanded to an external manufacturer as well. It consists in an oil deposit, oil pump, pressure gauge control, and the pistons connected to the floating roll shaft (Figure 29B). For replacement of the piston in the spring's site, it was necessary to drill one of the steel shafts that hold the spring to introduce the piston sleeve across this steel shaft (Figure 29C). Finally, the pressure gain of the system ranges between 0 to 300 bar.

A) Hydraulic piston schemme

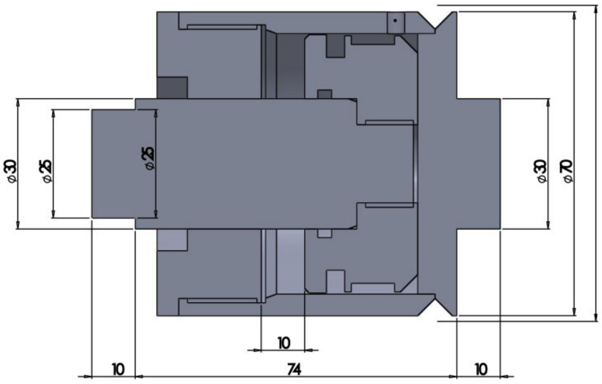

B) Hydraulic system for high pressure

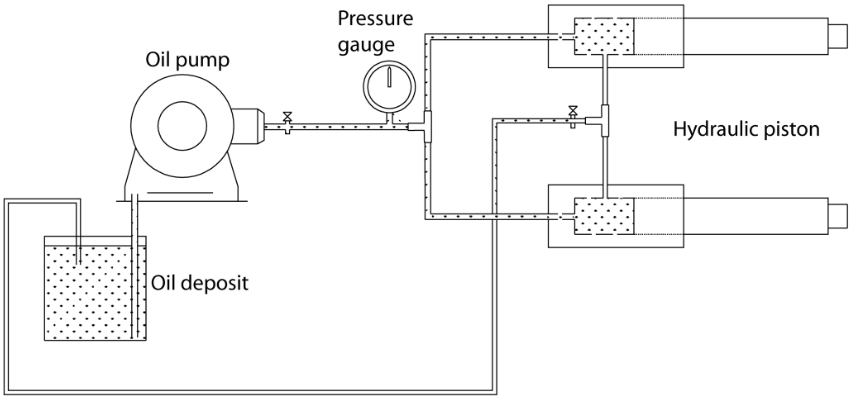

C) Piston situation

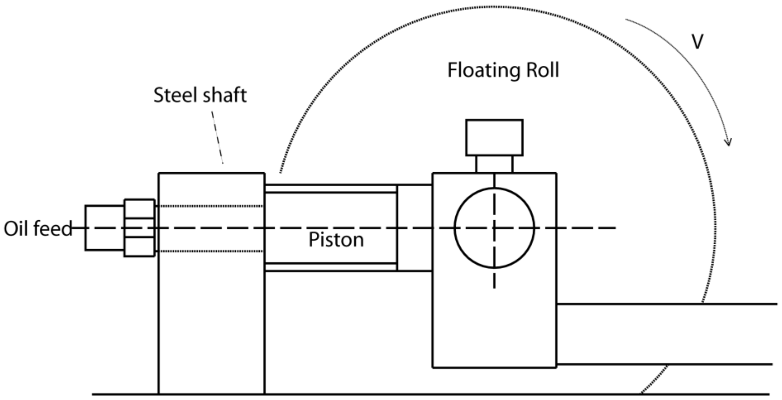

Figure 29. High-pressure design. A) Piston design, B) Hydraulic system, C) Position of the piston related to the floating roll.

As torque is direct proportional to the horizontal force acting on the material (Morrel et al., 1997), in order to increase this force, the original 3.7 kW motor was replaced with a 15 kW Siemens engine (Figure 30A), maintaining the system of transmission belts towards the rollers. The equipment uses smooth rolls with dimensions of 250 mm in diameter and 50 mm in width (Figure 30B). Other features of the device are: internal material deposit, adjustable frequency drive (AFD) and a crank to vary the zero gap. A transparent cover was built in order to observe the mechanical response of the material, and a slow-motion camera captured the moment of the particles under the roll breakage action. The horizontal displacement and speed of the rolls were also monitored.

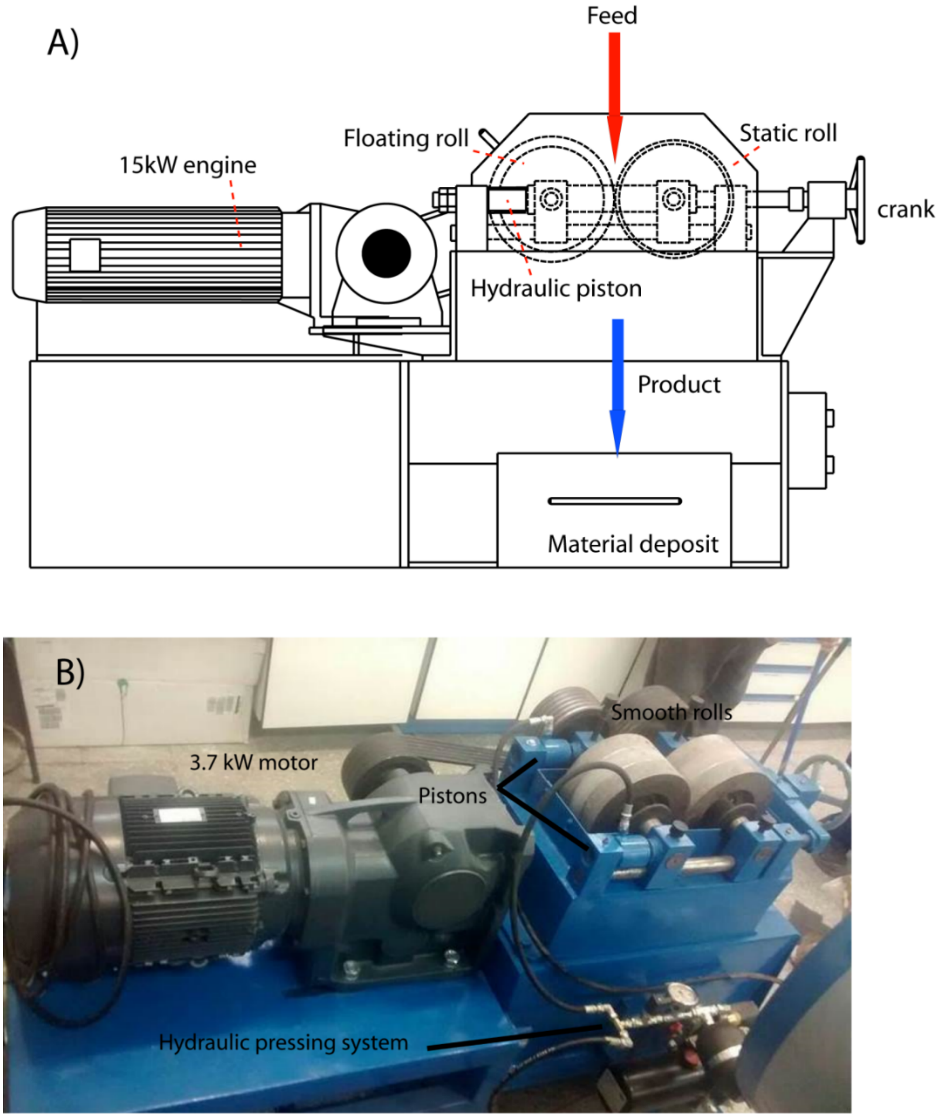

Figure 30. Reformed roll crusher into a high pressure roll crusher, lab-scale at UPC facilities, B) Lab-scale HPGR Köppern manufacturer at Freiberg university facilities.

A brief summary of the reformed roll crusher transformed into a high-pressure roll crusher is presented in Table 7.

Table 7. High-pressure roll crusher features.

Feature	UPC lab-device
Roll diameter (mm)	250
Roll length (mm)	50
Roll surface	Smooth
Rotational speed (m/s)	0-1
Specific pressing force (N/mm²)	0-4.5
Specific power draw (kWh/t)	1-1.2

Experimental design

The experiments were design under five main criteria: (1) to test material with controlled feed size distribution, (2) to observe the comminution when the roll speed is varied, (3) to analyse the product when the zero gap is varied, (4) to study the specific pressing force on the comminution process and (5) to test the material under similar specific pressing force in which the piston die procedure was executed.

Table 8 shows all operative parameters for the test performed with the lab-scale of the UPC device, using the Penouta and Mittersill materials. The different feed size range was tested under controlled specific force and surface speed. The feed top-size is given by Gupta (2006), where the ratio Feed-size/Working-gap should be up to 1.5. With the Mittersill material, the minimum ratio is 1.86, thus, this requirement is accomplished.

For accurate observations, the operative target condition was set-up on different values; meanwhile the rest of conditions remained static. The compression strength test results were used to set-up the specific pressing force, in order to avoid any displacement of the rolls during comminution.

Finally, for each material, a heterogeneous particle size distribution was used, with the aim of to verify the model consistency.

Table 8. All operative conditions of experiment on the high pressure roll crusher.

Category	Test number	Feed size range [mm] F	Specific Pressing Force [N/mm²] Fsp	Rolls Speed [m/s] U	Working Gap [mm] S_o
Penouta	PV-1	+9.5– 12.0	2.5	0.73	3.0
	PV-2	+9.5–12.0	2.5	0.58	3.0
	PV-3	+9.5–12.0	2.5	0.44	3.0
	PV-4	+9.5–12.0	2.5	0.29	3.0
	PF-1	+6.7–9.5	2.5	0.58	3.0
	PF-2	+12.5–14.0	2.5	0.58	3.0
	PF-3	+4.5–6.7	2.5	0.58	3.0
	PF-4	+16.0–19.0	2.5	0.58	3.0
	PP-1	+6.7–9.5	2.5	0.58	3.0
	PP-2	+6.7–9.5	1.5	0.58	3.0
	PP-3	+12.5–14.0	1.3	0.58	3.0
	PG-1	+6.7–9.5	1.3	0.58	2.0
	PG-2	+6.7–9.5	2.5	0.58	3.0
	PG-3	+6.7–9.5	2.5	0.58	4.0
	PT-1	PSD	2.5	0.58	5.0
Mittersill	MV-1	+4.5–6.7	2.5	0.73	3.0
	MV-2	+4.5–6.7	2.5	0.58	3.0
	MV-3	+4.5–6.7	2.5	0.65	3.0
	MV-4	+4.5–6.7	2.5	0.51	3.0
	MP-1	+4.5–6.7	1.25	0.73	3.0
	MP-2	+4.5–6.7	1.75	0.73	3.0
	MP-3	+4.5–6.7	2.5	0.73	3.0
	MP-4	+4.5–6.7	3.25	0.73	3.0
	MP-5	+4.5–6.7	4.5	0.73	3.0
	MT-1	PSD	2.5	0.73	5.0

5.5.2. Validation using industrial HPGR

Machinery design

The validation test work was carried out at the Köppern Aufbereitungstechnik GmbH & Co.KG pilot plant, located at the Technische Universität Bergakademie Freiberg facilities, Germany, using the Barruecopardo granite material.

The machinery used for model validation consists of two robust devices. The first is lab-scale type machinery (Figure 31A). It has 0.3 m diameter of and 0.07 m width smooth rolls (Figure 31B). The other is an industrial type device (Figure 31C), of 1.0 m diameter with 0.23 m wide rolls (Figure 31D). They are supported in the frame by spherical roll bearings, which are inherently self-aligned and very robust. The floating roll uses a hydro-pneumatic system that allows horizontal movements, leading same pressurizing condition to all the feed material that pass through the rolls (www.koeppern.de). Both models have studded liners roller surface, and use four eccentrically nitrogen fed pistons, applying a range of pressure from 0 to 4.7 N/mm² (Table 9). Some wear resistant linings features are: welded hard-facings, cast metal linings, composite steel and HEXADUR, and especial Köppern proprietary wear protection.

Table 9. High pressure grinding rolls features.

	Köppern lab-device	Köppern industrial device
Roll diameters (mm)	300	1000
Roll length (mm)	70	230
Roll surface	Smooth	Stooded
Rotational speed (m/s)	0-0.134	0-1
Specific pressing force (N/mm²)	0-1.307	0-4.7
Specific power draw (kWh/t)	1.2-1.4	1.2-2.1

In terms of test monitoring ability, the device has several sensors able to measure some key parameters of the process (Table 10).

Table 10. Sensor ability of the industrial Köppern HPGR.

Condition or parameter	Unit
Circumferential Speed	m/s
Nitrogen Pressure	bar
Working Pressure	bar
Spec. Press. Force	N/mm^2
Working gap	mm
Wt	kWh/t

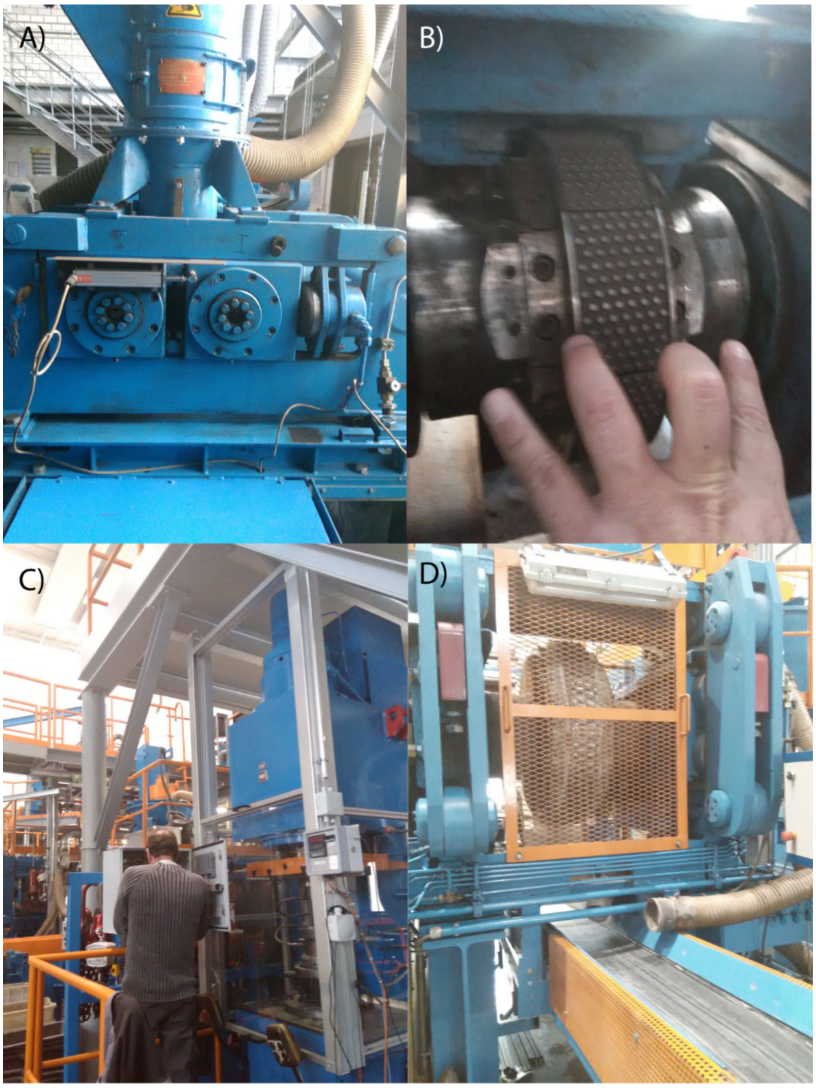

Figure 31. Validation stage at Köppern manufacturer pilot plant. A) View of the lab-scale HPGR, B) Dimensions of the roll of the lab-scale device, C) View of the industrial scale HPGR, D) Studded roll of the industrial HPGR model.

Test design

The validation using Köppern manufacturer HPGR was carried out based on same criteria for experimental stage described on the pervious chapter. However, the number of tests was increased, taking into account a greater number of possibilities of affection of operating conditions and characteristics of the input material. The feed top-size was the main input that could affect the product characteristic, for this reason, five size classes were used. After that, the specific pressing force was set-up in three values: 2.5, 3.5 and 4.7 N/mm². The affection of the roll speed on the resulted particle size distribution is minimum (Gupta, 2006) and only affect the process throughput. However, it was introduced in the tests program, but it was studied with only one particular specific pressing force.

Thus, the feed size was tested under three specific pressing forces, and one specific pressing force was tested under three roll speeds. When the target parameter is set-up and is varied controlled, the other conditions remain constant (Figure 32). A heterogeneous particle size distribution was used in order to validate the model with a common material used in the industry (Table 11). Finally, three tests on the Köppern lab-scale device were performed in order to be compared with the UPC lab-scale high pressure roll crusher model.

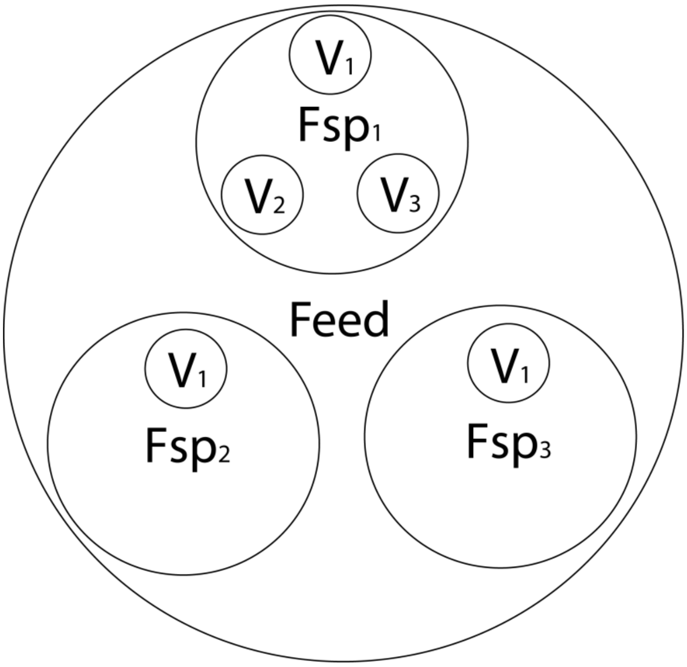

Figure 32. Experimental design fundamental.

Table 11. Al operative conditions of the HPGR in Köppern manufacturer.

Category	Test number	Feed size range	Specific Pressing Force	Roll speed	Working Gap
		[mm]	[N/mm²]	[m/s]	[mm]
		F	Fsp	U	S_o
I	1	+0.0-3.0	2.5	0.56	18.0
	2	+0.0-3.0	2.5	0.78	18.4
	3	+0.0-3.0	2.5	1.00	18.8
	4	+0.0-3.0	3.5	0.56	16.9
	5	+0.0-3.0	4.7	0.56	16.2
II	6	+3.0-8.0	2.5	0.56	18.5
	7	+3.0-8.0	2.5	0.78	18.8
	8	+3.0-8.0	2.5	1.00	19.0
	9	+3.0-8.0	3.5	0.56	17.0
	10	+3.0-8.0	4.6	0.56	16.2
III	11	+8.0-14.0	2.5	0.56	19.8
	12	+8.0-14.0	2.5	0.78	20.0
	13	+8.0-14.0	2.5	1.00	19.7
	14	+8.0-14.0	3.5	0.56	17.8
	15	+8.0-14.0	4.5	0.56	17.3
IV	16	+14.0-22.0	2.5	0.56	19.8
	17	+14.0-22.0	2.5	0.78	19.6
	18	+14.0-22.0	2.5	1.00	18.8
	19	+14.0-22.0	3.5	0.56	18.5
	20	+14.0-22.0	4.5	0.56	17.5
V	21	PSD	2.5	0.56	26.4
	22	PSD	2.5	0.78	25.4
	23	PSD	2.5	1.00	25.5
	24	PSD	3.5	0.56	23.8
	25	PSD	4.5	0.56	23.0
VI	26	+0.0-3.0	2.5	0.17	5.8
	27	+3.0-8.0	2.5	0.17	6.7
	28	+0.0-8.0	2.5	0.17	7.5

The categories I to VI are related to the feed size range. As the material come from a quarry, that classifies the material into these different size classes, to be sold, the sample preparation was not necessary in this case. The detailed particle size distribution of the tests 21 to 25 are shown in the next *results* chapters. Despite the working gap is an output (the zero gap is fixed in 10cm), it was added to the operative parameter table in order to be comparable with the previous experimental operative conditions (Table 11)

5.6. Modelling

The literature shows several approaches to model HPGR particle size distribution. However, two of this approaches highlight for this type of machinery; when a single particle compression is combined with a batch grinding solution (Torres and Casali, 2009; Saramak, 2011) or by means of the calculation of several matrices between the differential feed and the breakage distribution function (Austin et al., 1993; Kodali et al., 2011). This study is based on the Austin (1993) model, but with modifications compared with the original expression:

- The breakage distribution function parameters have different values when running under single particle compression compared to running under bed compression. The mechanical characterization probed how the breakage distribution function is non-normalizable when the process is under single particle compression or when is under bed compression condition.
- The breakage distribution function parameters are also influenced by the specific pressing force, and the model takes this operative condition.
- This improved approach uses a selection function that is able to discriminate particles that are large enough to be nipped under the rolls from the remaining particles, which can be subjected to the bed compression effect. Thus, the selection function is governable based on the feed particle size distribution, the internal products of the model, the geometric dimensions of the device and other characteristics, such as the material density and operational gap.

A block model was developed based under these premises (Figure 33).

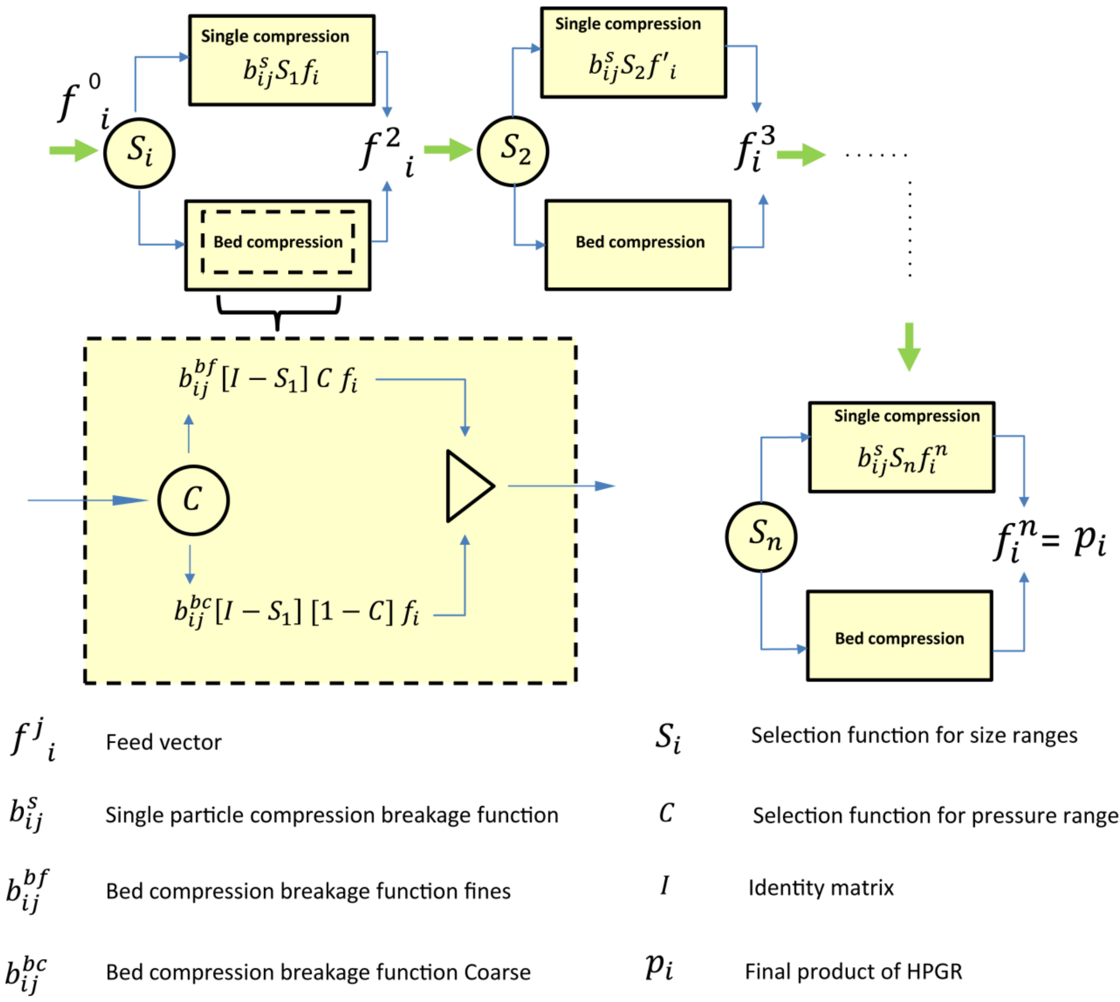

Figure 33. Block scheme of the new model base on Austin (1993) approach but added the new finding of this investigation.

The matrices b_{ij}^{s}, for single particle compression, b_{ij}^{bf} and b_{ij}^{bc} for bed compression, represent the differential matrices extracted from the cumulative form of B distribution (King, 2001) but using different parameter values when the sample is under single particle compression compared to when it is under the bed compression effect. These parameters also change when varying the specific pressing force. The feed f_i enters the pre-crushing zone, where the particles are discriminated by the selection function S_i. Over a certain cut-size, some of them go to the single particle compression and the remaining ones go to the bed compression. The product p_i is the sum of the results of both sub-processes after n stages of comminution. The selection function used in this case belongs to the formulation reported by Whiten et al. (1979), used mainly for cone and jaw crushers (Evertsson and Bearman, 1997; Nikolov, 2004); here it was applied for HPGR. Equation (3) describes this physical process in the steps at which single particle compression occurs. This function has the particularity of fixing upper and lower edges, which is related to the device geometry and the mineral characteristics.

$$S_{n,i} = 1 - \left(\frac{dp_i - x_n}{d_1 - x_n}\right)^{\gamma} \; for \; d_1 < dp < x_n$$

$$S_{n,i} = 0 \; for \; dp < d_1$$

$$S_{n,i} = 1 \; for \; dp > x_n \tag{3}$$

The parameter x_n in Equation (3) represents the upper limit of the function and is given by the distance between rolls when the nipping action begins and d_1 is the lower limit where the particles cannot be subjected to comminution under the single particle compression condition due to their size. Therefore, they tend to form in the bed compression zone, due to the interaction between coarse and fine particles. The parameter γ is related to the mineral characteristics (Evertsson and Bearman, 1997) and describes the shape of the curve of the selection function Sn. The parameter x_n is function of the nip angle (Equation 4) and represents the relationship among all geometric characteristics of the device, material feed size and other features such as the material density, gaps and roll diameter (Equation 5; Torres and Casali, 2009).

$$x_n(\alpha_n) = S_0 + D(1 - \cos(\alpha_n)) \tag{4}$$

$$cos(\alpha_{nip}) = \frac{1}{D}\left[(S_0 + D) + \sqrt{(S_0 + D)^2 - \frac{4S_0\delta D}{\rho}}\right] \tag{5}$$

The parameter ρ (t/m^3) in Equation (5) is the bulk density at the feed zone and δ (t/m^3) is the bulk density at the extrusion zone, which is to say, the product density. Furthermore, D (m) is the roll diameter, and S_0 (m) is the gap. The values of the vector S_n depend on x_n, which is a function of the angle α (Figure 34). N_t denotes the number of single particle compression stages necessary to simulate the breakage of the material until almost all particles reach the gap size and they can be considered as a final product (Torres and Casali, 2009). The angles used to evaluate the function x_n are defined as in Equation (6).

$$\alpha_n = \frac{N_t - (n-1)}{N_t} \alpha_{nip} \, , n = 1 \ldots N_t \tag{6}$$

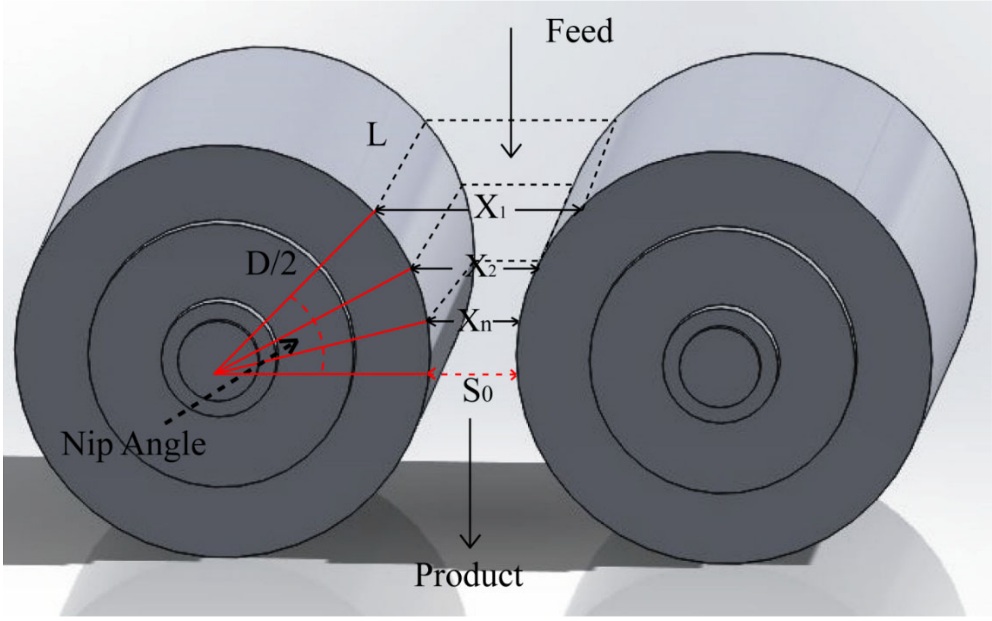

Figure 34. Calculation methodology for the Xn parameter which is useful for the selection function.

In order to evaluate the value of N_t in the crushing stages, several simulations of single particle compression were performed, using the breakage function parameters found (Anticoi et al., 2018a). Equation (8) is presented to determine that lumps larger than the gap that must undergo repetitive breakage in order to be realized as a final product.

$$b_{ij}^{s} x\, f_i = {P_i}^1$$

$$b_{ij}^{s} x\, {P_i}^1 = {P_i}^2$$

$$b_{ij}^{s} x\, {P_i}^2 = {P_i}^3$$

$$b_{ij}^{s} x\, {P_i}^{N_t - 1} = {P_i}^{N_t} \tag{7}$$

Equation (7) is a loop of matrices' product x that stops when no more particles larger than the gap size are generated, and N_t is determined by the number of steps necessary to reach this size. In this work, the way in which the value of N_t is determined is compared with other characteristics of the material, such as the shape of the particles and the distance of the rollers for each rupture stage.

The throughput G_s [t/h] was calculated using Equation (8), in which is dependent on the material density, the previous calculated gap and some geometric features of the device.

$$G_S = 3600\, \rho\, S\, L\, U \cos(\alpha) \tag{8}$$

5.7. Notation and error evaluation

All calculations for both breakage functions parameters determination and particle size distribution prediction was programmed using MATLAB® script (R2016a) and different solver functions from the tool-box of the software. This software combines desktop environment tuned for iterative analysis and design processes with a programing language that expresses directly matrix and array mathematics. For this study, some expressions are naturally matrices, but other functions are transformed in matrix expression for optimal performance of the calculation programme (Figure 35)

$$b_{i,j} = \begin{bmatrix} b_{1,1} & 0 & 0 & \dots & 0 \\ b_{1,2} & b_{2,2} & 0 & \dots & 0 \\ b_{1,3} & b_{2,3} & b_{3,3} & \dots & 0 \\ \dots & \dots & \dots & \dots & 0 \\ b_{1,m} & b_{2,m} & b_{3,m} & \dots & b_{m,m} \end{bmatrix} \qquad S_{n,i} = \begin{bmatrix} S_{n,1} & 0 & 0 & \dots & 0 \\ 0 & S_{n,2} & 0 & \dots & 0 \\ 0 & 0 & S_{n,3} & \dots & 0 \\ \dots & \dots & \dots & \dots & 0 \\ 0 & 0 & 0 & \dots & S_{n,m} \end{bmatrix} \qquad I = \begin{bmatrix} 1 & 0 & 0 & \dots & 0 \\ 0 & 1 & 0 & \dots & 0 \\ 0 & 0 & 1 & \dots & 0 \\ \dots & \dots & \dots & \dots & 0 \\ 0 & 0 & 0 & \dots & 1 \end{bmatrix}$$

Figure 35. The form B_{ij} of the breakage distribution function and the selection function, among others, expressed in their matrix form. I = 1….m, j = 1….m and n = 1…. Nt, with m being the pi vector length.

The model fitting has to evaluate in order to check the robustness and the capacity of it. Matlab has incorporated different solver and error evaluator, and the scope is to measure the agreement between the experimental data and the model's predictions. Although the mean absolute error (MAE) is simpler and direct (Willmott and Matsuura, 2005), the best tool to appraise this difference is the Root Mean Square Error (RMSE) (Equation 8) mainly due to the fact that most of the model errors were produced on key parameters of a typical particle size distribution (PSD) such as the P_{80} or P_{50}. RMSE gives higher weight to large errors rather than lower errors in the formalism (Roy et al., 2016). In this case, the evaluation of results is more adverse and, therefore, more demanding.

$$RMSE = \sqrt{\frac{1}{N}\sum_{i=1}^{N}(p_i - y_i)^2} \tag{9}$$

The parameter N in Equation (8) is the length of the input vector, p_i represents the experimental values of the vector and y_i represents the simulated values. In order to evaluate local values, as the differences between P_{80} and P_{50}, the percentage variation was used (Equation 9).

$$\% = 100\ x\ \frac{|V_i - V_f|}{|V_i|} \tag{10}$$

In Equation (10), V_i is the experimental value and V_f is the final model predicted value.

CHAPTER IV

Results

6. RESULTS

6.1. Mineralogical Characteristics

The mineralogical characterization is presented in such a way to be compared with the mechanical characterization. The patterns in the response of the material in front of compression and the mineral composition are the basis for the mathematical model presented in the methodology. Thus, the results of the lab-test work and the validation test are presented in the same way to be comparable with the previous characterization stage. Error calculation confirm the consistency of the laboratory results within the model calculation, thus they are presented previous any particle size distribution prediction.

6.1.1. Mineralogical Characteristics of the raw materials

The samples were analysed before compression tests using optical microscopy and XRD. The altered granite (from the Penouta mine) that hosts the tantalum and tin ores, is mainly constituted by quartz (SiO_2), albite ($NaAlSi_3O_8$), K-feldspar (microcline, $KAlSi_3O_8$), muscovite ($KAl_2(AlSi_3O_{10})(OH)_2$) and kaolinite ($Al_2Si_2O_5(OH)_4$). The ore minerals are cassiterite (SnO_2) and columbite-group minerals, with minor microlite ($(Na,Ca,U,Pb,REE)_2(Ta,Nb)_2O_6(O,OH,F)$) and wodginite ($MnSnTa_2O_8$) contents (Alfonso et al., 2018). Regarding its texture, it is inequigranular; remarkable sized quartz grains of 1-3 mm in diameter were found surrounded by a matrix of micas and the altered feldspars (Figure 36). Quartz was also found in fine gains (smaller than 500 µm). The quantitative composition of the present minerals indicated a high content of easily alterable minerals, such as albite and the occurrence of kaolinite, which represents the altered product (Figure 37).

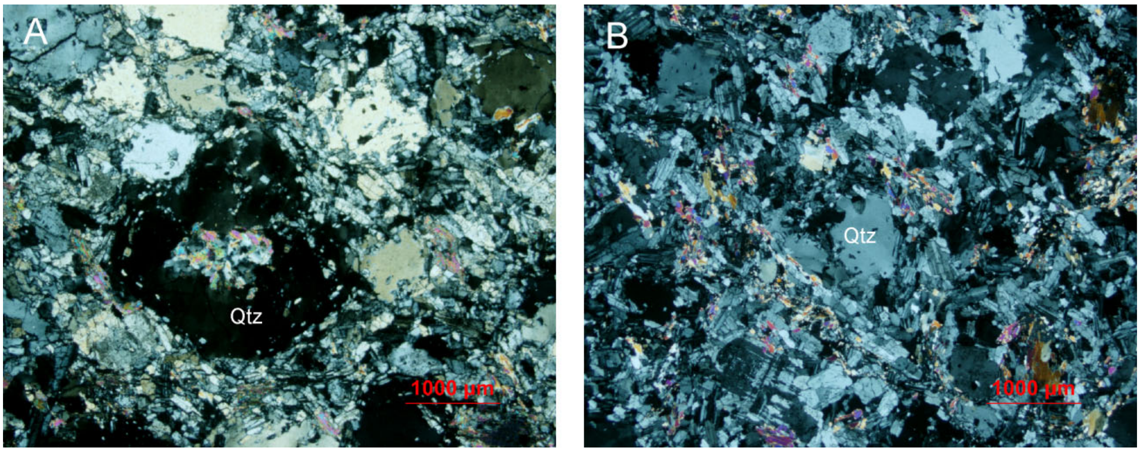

Figure 36. Optical micrographs showing the mineralogy of the altered granite, where the largest grains are quartz (Qtz) surrounded by micas and albite with kaolinite. (A) Quartz with mineral inclusions, (B) Muscovite (colourful) surrounds quartz grey grains (Anticoi et al., 2018a).

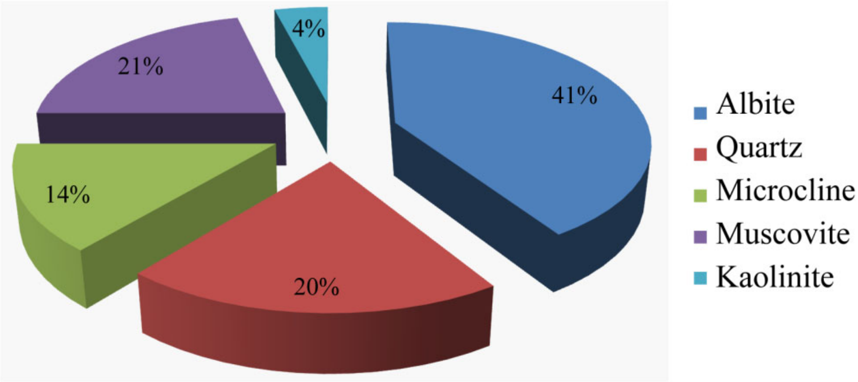

Figure 37. Mineral composition of the material used in the experiments determined by XRD of the granite from Penouta mine.

The calc-silicate ore from the Mittersill mine is an amphibolite rock mainly composed of quartz (SiO_2), plagioclase of albite type ($Na(AlSi_3O_8)$), hornblende ($Ca_2(Mg, Fe, Al)_5$ $(Al, Si)_8O_{22}(OH)_2$), actinolite ($Ca_2(Mg,Fe^{2+})_5Si_8O_{22}(OH)_2$), K-feldspar, and biotite ($K(Mg,Fe)_3(AlSi_3O_{10})(F,OH)_2$), as well as muscovite ($KAl_2(AlSi_3O_{10})(OH)_2$) and epidote ($Ca_2Fe^{3+}Al_2(Si_2O_7)(SiO_4)O(OH)$) in minor amounts (Figure 38). The ore is scheelite ($CaWO_4$) and its content is around 0.3 wt%

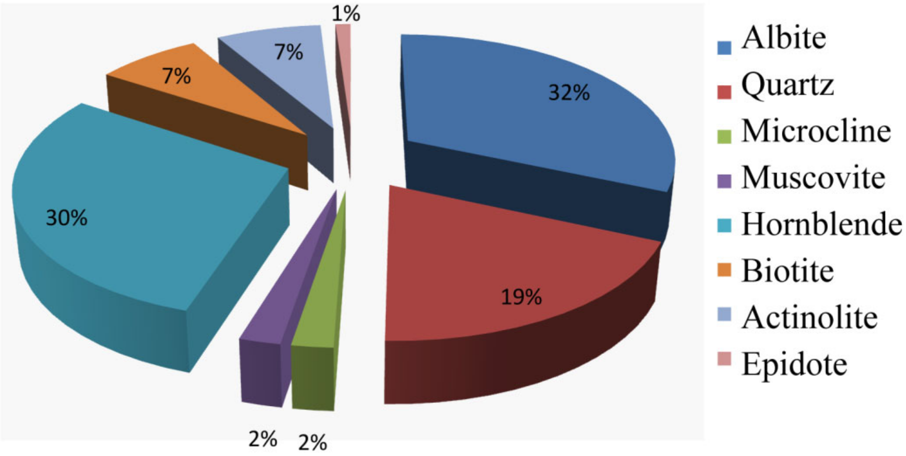

Figure 38. Mineral composition of the material used in the experiments determined by XRD of the calc-silicate from Mittersill mine.

The granite from Barruecopardo is mainly composed by quartz, albite, muscovite and microcline, with a lesser content of kaolinite and hematite (Figure 39). The main ore, scheelita, is around 0.12 wt% to 0.14% wt.%.

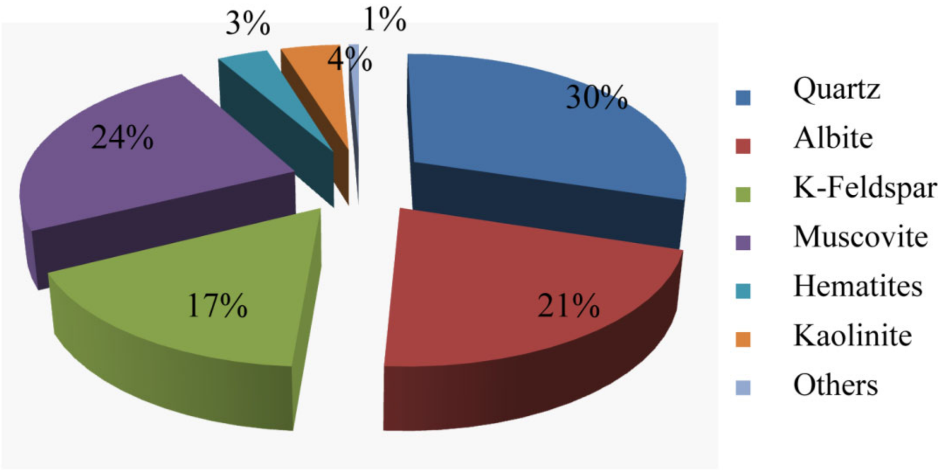

Figure 39. Mineral composition of the material used in the experiments determined by XRD of the granite from Barruecopardo.

6.1.2. Mineralogical characterization after compression

The raw material described above was also characterised after the compression test. The results are shown expressed in terms of their size ranges related with their mineral composition respectively. In some cases they are grouped, according their similar mechanical characteristics. The leucogranite material presents a high grade of albitisation, with similar albite content along all their particle size classes. The quartz content behave indirectly proportional with albite content. Quartz has one of the highest strength/specific fracture energy ratio (Kanda et al., 1986): The energy input for size reduction is inefficient in the compression action, thus the large size particles are more abundant in quartz. In the smallest sizes, micas retain their maximum content, that is in the 0.6 mm particle size range (Figure 40).

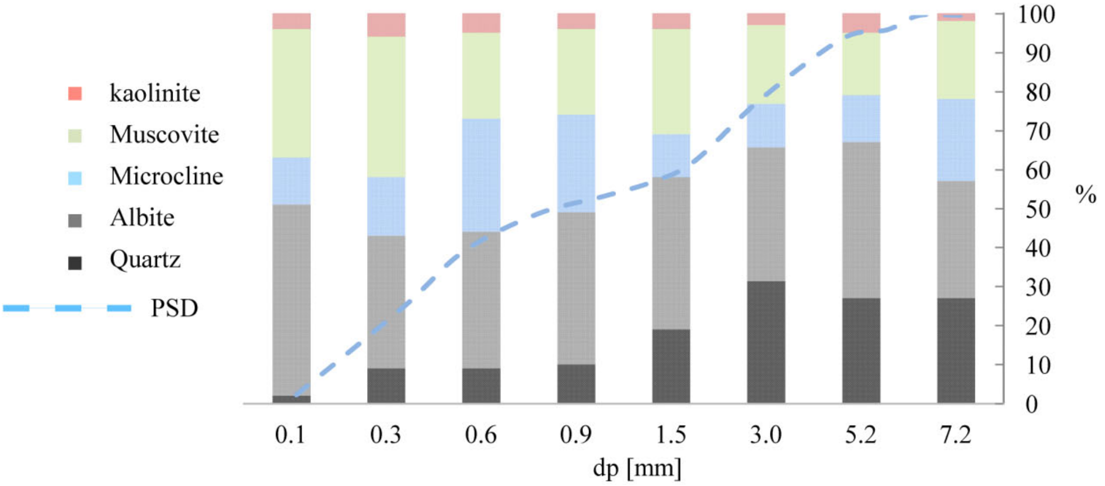

Figure 40. Particle size distribution of the altered leucogranite of the Penouta mine, compared with it mineral composition for each size rang

The Mittersill calc-silicate material was ordered in amphiboles (hornblende + actinolite), the group of phyllosilicates (biotite + chamosite) and the feldspar (plagioclase albite + KFeldspar) (Figure 41). It is observed how the amphiboles (hornblende + actinolite) are abundant in larger sizes, especially in dp=7.2 mm range, and it decreases with the particle size. The highest quartz content is found in the middle size range, 1.5 mm, and is lower in the rest of size ranges. The phyllosilicates content remains more or less constant, except in the dp=5.2 mm range, where there is a slightly difference with the rest of sizes population. The feldspar content is indirectly proportional to the amphibole content, being the size range dp=1.5 mm the more content one.

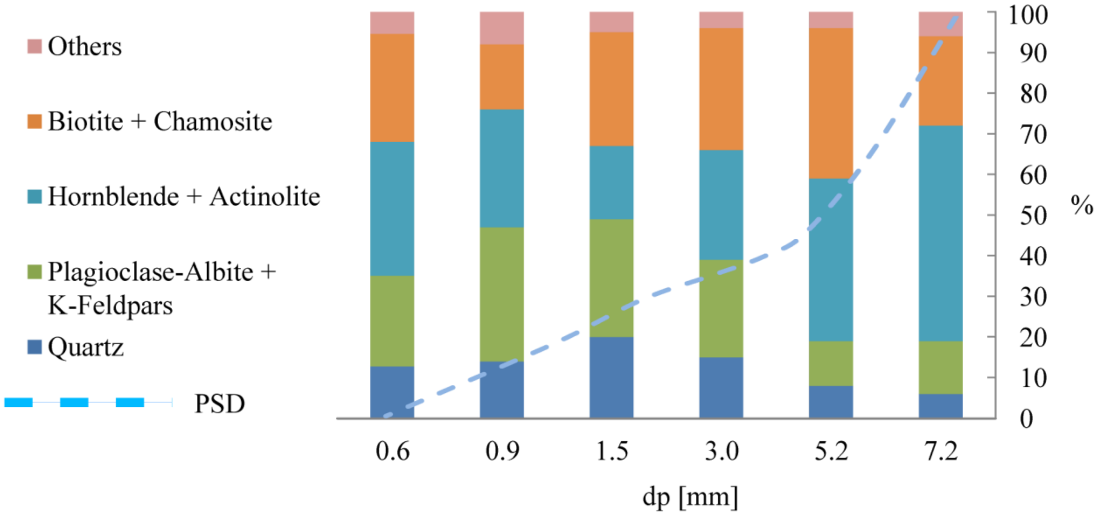

Figure 41. Particle size distribution results related with their minerals composition of the calc-silicate material from the Mittersill mine.

The material from the tailing of Barruecopardo is more consistent, from the mechanical point of view. Kaolinite and albite content feed the fines phases. Quartz is present in all size classes, but it is remarkable high in the coarse particle size class. The K-Feldspar content is low in smaller particles, being in similar contents in the rest of size classes (Figure 42).

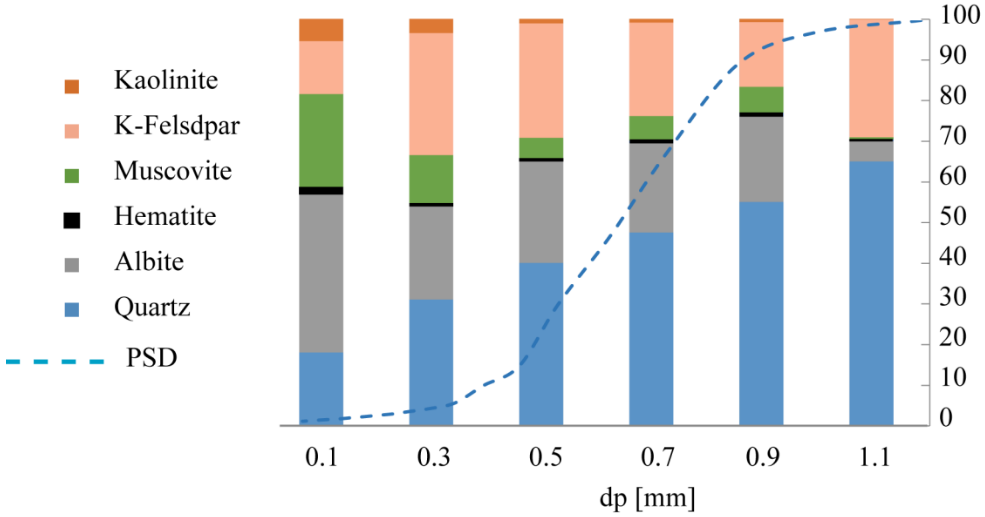

Figure 42. Particle size distribution results related with their minerals composition of the calc-silicate material from the Barruecopardo tailings.

6.2. Single compression strength test results

The results of the single compression tests are shown in Table 12. The leucogranite has a resistance to single compression between 181 kg/cm² to 528 kg/cm² and this value for the calc-silicate ranges from 440 kg/cm² to 900 kg/cm².

Table 12. Resistance to compression of the leucogranite from Penouta mine and the calc-silicate of the Mittersill mine.

Materials	Sample	Resistance to compression (Kg/cm²)	Density (t/m³)
Leucogranite	L1	245	1.5
	L2	528	1.5
	L3	400	1.5
	L4	181	1.5
Calc-silicate	C1	900	1.8
	C2	440	1.8
	C3	720	1.8
	C4	880	1.8

These results have been transformed into specific pressing force (Fsp), which is the standard operative parameter for HPGR. All values are under the boundary 5 N/mm². This obtained value is used as a landmark in the operative condition on the experimental stage. Thus, all the experimental tests with the high pressure roll crusher was set-up under this specific pressing force limit (Figure 43). The red square and the blue square in the Figure 8 shows referenced average range values for calc-silicates and granites respectively, when their resistance to compression is also transformed into specific pressing force. The differences in their values are clear and consistency with the materials tested and the test procedure.

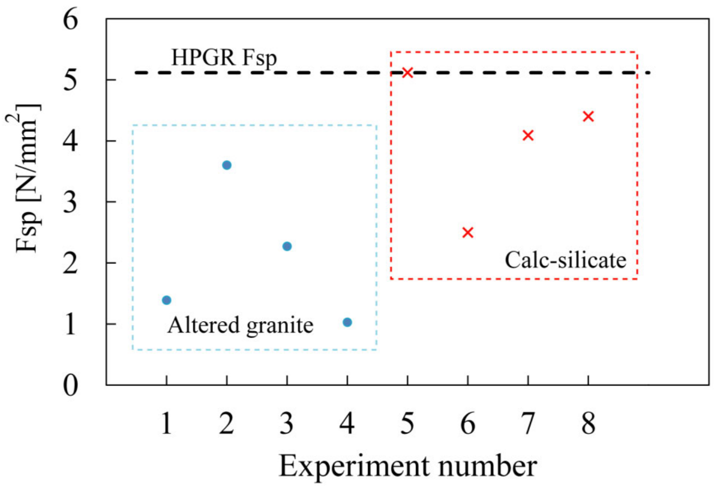

Figure 43. Specific pressing force (Fsp) calculated for all lab-scale device tests.

Figure 44 shows several samples after being compressed in the pressurized press. In Figure 44A and B probes made with the Penouta material, can be observed and Figures 44C and D show tested probes of the Calc-silicate material. No test was done on the Barruecopardo material, since it did not comply with the standard size for strength compression test.

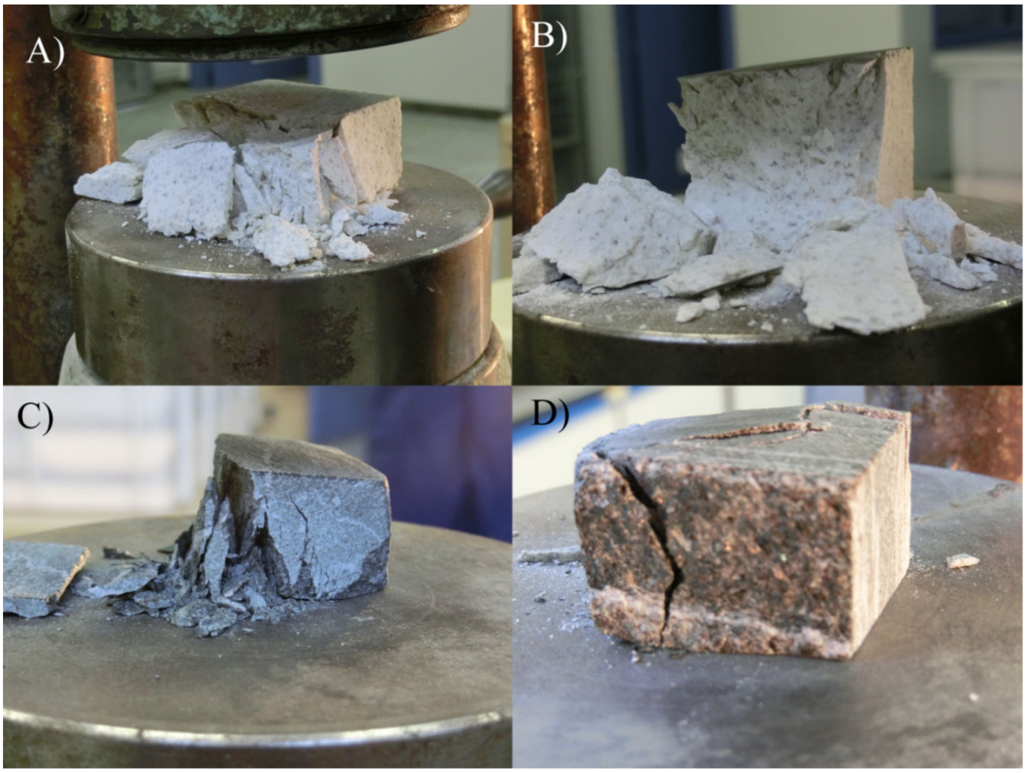

Figure 44. Samples after single compression strength test. A) and B) Leucogranite from Penouta, C) and D) Calc-silicate from Mittersill.

6.3. Breakage distribution function

The piston die test was conceived to simulate a pressurising environment, and to determine the breakage characteristics of the material that is comminuted in a high pressure grinding rolls (Figure 45).

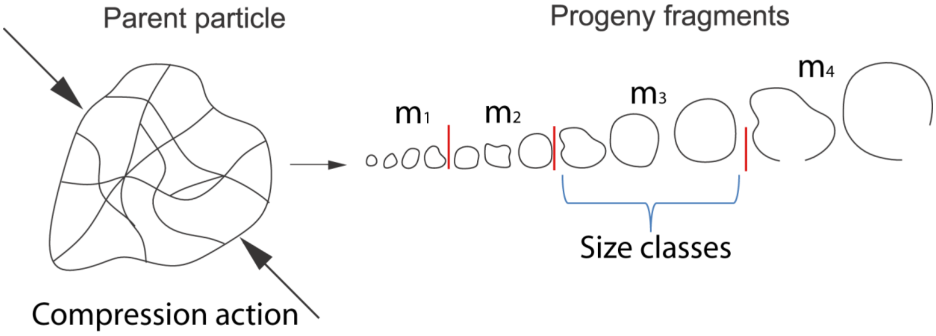

Figure 45. Progeny particle classification after compression.

Some gross results are shown in Table 13, where the comminuted mass inside the piston can be observed, for each size range. These results have to be transformed into relative size reduction against cumulative mass.

Table 13. Non-processed results from the piston-die test of the Penouta material, in bed particle compression condition.

		Mass (g)			
Mesh size (mm)		4.75-4	4-2	2-1	1-0.71
4.75	4	28.1	0	0	0
4	2	35.5	60.2	0	0
2	1	11.4	20.5	61.4	0
1	0.71	2.3	4.2	8	40.2
0.71	0.5	1.5	2.7	3.8	10.9
0.5	0.3	1.6	2.8	3.5	5.8
0.3	0.15	2.2	5.3	3.9	5.7
0.15	0.09	1.9	4.6	3.5	4.8
0.09	0.053	1.6	1.1	2.5	3.5
0.053	0	0.8	0.3	1.5	2.1

As an example, in Table 14, only one single test is shown (with mono-size particle 4.75-4 mm). The mesh sizes have been transformed into arithmetic mean Dp, and the size range particle test 4.75-4 mm has been changed into dp= 4.4 mm, also arithmetic mean. The relative size reduction is the dp/Dp ratio. The total mass was transformed into relative mass and cumulative mass.

Table 14. Piston-die test results performed with the material dp= 4.4 mm, showing the differential mass and the cumulative mass, and the relative size reduction dp/DP.

Dp (mm)	dp_i/Dp_j	Differential mass	Cumulative mass (%)
8.10	0.00	0.00	100
5.70	0.00	0.00	100
4.40	1.00	0.32	100
3.00	0.69	0.41	67.70
1.50	0.34	0.13	26.80
0.90	0.20	0.03	13.70
0.60	0.14	0.02	11.00
0.40	0.09	0.02	9.30
0.20	0.05	0.03	7.50
0.12	0.03	0.02	4.90
0.07	0.02	0.02	2.80
0.03	0.01	0.01	0.90

Plotting more results in the same graph, with a wide range of parent particle Dp, the shape of the breakage distribution function trends to be the same, thus it has been normalized (Figure 46). They are showed in their formal cumulative mass form against size reduction ratio dp_i/Dp_j. The calc-silicate material accomplished the typical curve of the breakage distribution function (Figure 46A). Thus, with the reference methodology (King, 2001) it is possible to find the function parameters. The straight line defines the parameters n_1 as its slope in the log-log coordinates. The difference between the original curve (a) and the first straight line (b) is itself a curve rather than a straight line, with n_2 slope. Both interceptions with the y axis define the k parameter value.

The leucogranite material behaves as bimodal function (King, 2001), and the methodology to find the function parameters is slightly extensive: there are two more constants, n_3 and y_0, which depend on the fines reduction ratio area of the distribution function plot (Figure 46B).

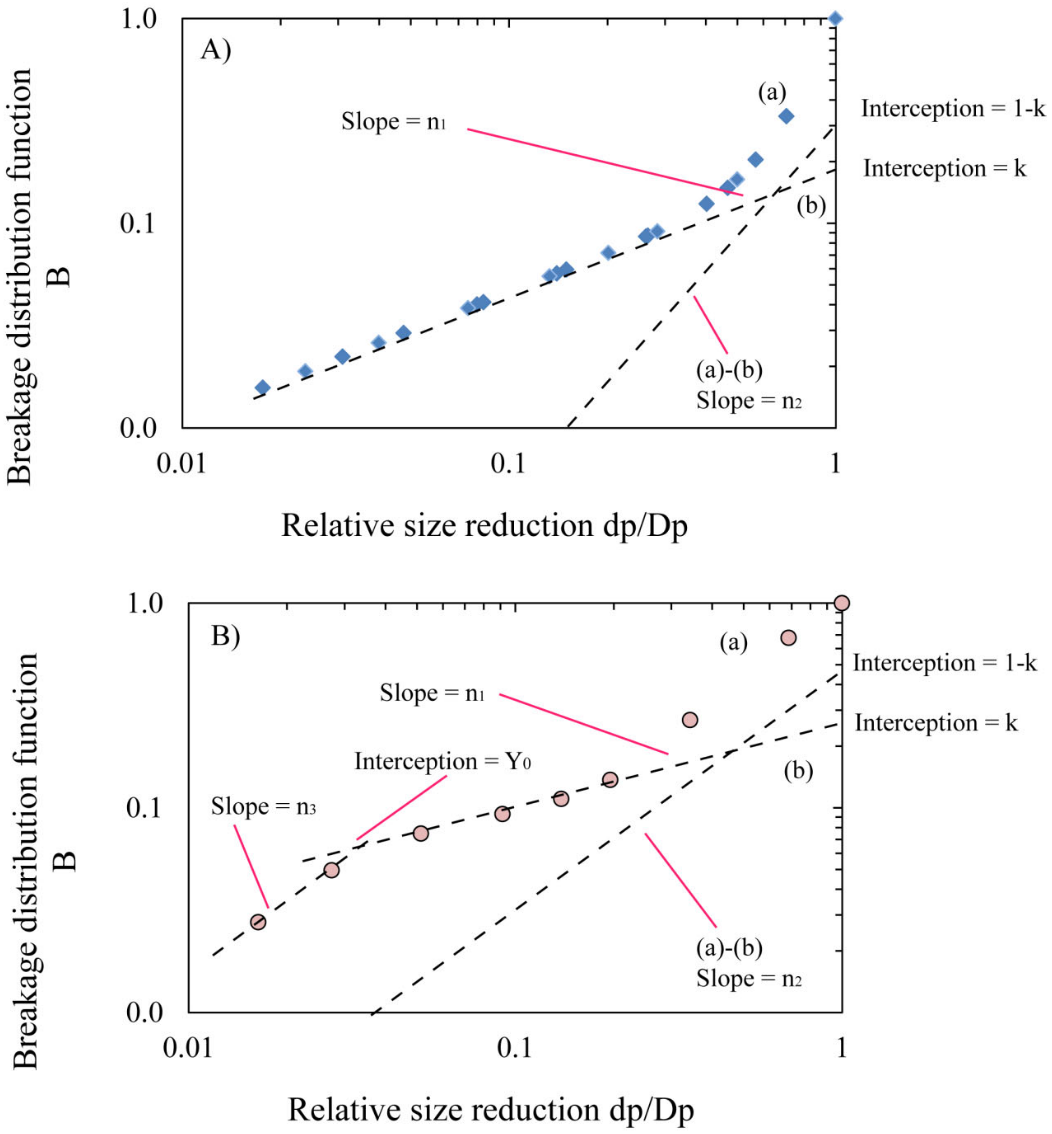

Figure 46. Breakage distribution function of different test in only one graph. A) calc-silicate material B) leucogranite.

Based on the breakage distribution function parameterization, the resulted values found with the graphical methodology (king, 2010) are shown in Table 15 for the two compression condition: Single particle compression (SPC) and bed particle compression (BPC), for the leucogranite and the calc-silicate material.

Table 15. Breakage distribution parameters obtained by the piston-die methodology for the leucogranite from Penouta and the calc-silicate from Mittersill. k, n_1, n_2 and n_3 are dimensionless. Y_0 is in m.

Material	Condition	k	n_1	n_2	n_3	Y_0
Granite	SPC	0.68	0.37	1.95	0.64	0.0036
	BPC	0.47	0.66	2.16	0.45	0.0045
Calc-silicate	SPC	0.60	0.61	2.32	-	-
	BPC	0.19	0.62	4.37	-	-

The granite from Barruecopardo was also tested under the piston-die test. This material behaves in the standard form of the breakage function (Figure 47). The differences with the other materials are shown by the k interception values. This difference should be observed in the final parameters determination.

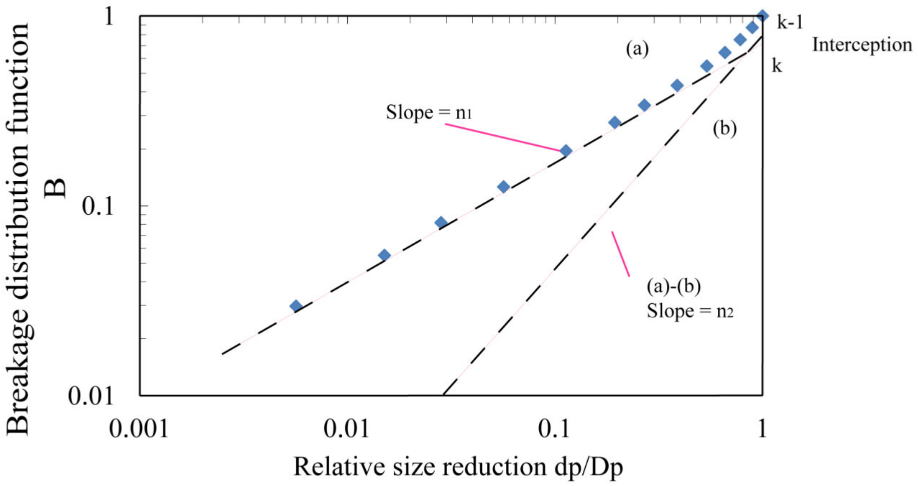

Figure 47. Results of the piston-die test of the Barruecopardo granite.

This material was also tested varying the specific pressing force, in order to find or to confirm patterns in the mechanical response of the material in front of different operational conditions. Granites have boundaries resistance to compression, with a maximum of 4 MPa and minimum around 1 MPa. For this reason, the results (the tests were planned based in this fact) are presented trying to observed variation on the breakage distribution function with specific pressing force variation. As an example, for a test with one particle dp range between 4.00 mm and 3.15 mm (Figure

48A) the differences on curves are visible and conclusive: the dependency on the breakage characteristic is evident. Same results for all size ranges particle test (Figure 48B to 48F).

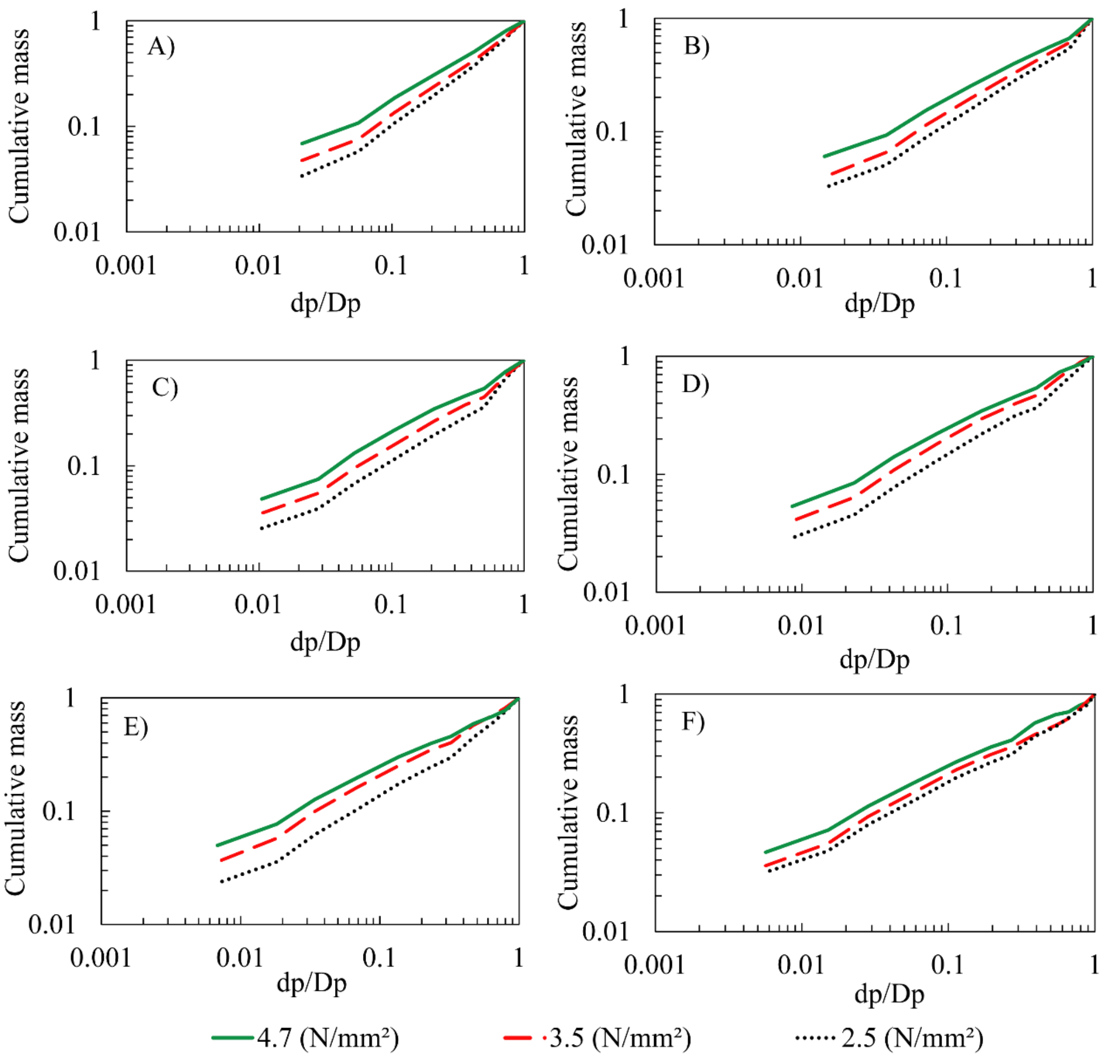

Figure 48. Results of the piston-die test at three specific pressure forces (Fsp), with different narrow ranges of particle sizes; A) -4+3.15 mm size range, B) -6.3+4 mm size range, C) -8+6.3 mm size range, D) -9.5+8 mm size range, E) -12.5+9.5 mm size range and F) -14+12.5 mm size range.

The observation of the curves when the compression test is executed under different specific pressing force seems to be similar for all mono-size particles in which the test was performed (Figure 49). In order to check the behaviour of the curves, they are plotted grouping all particle size with same specific pressing force. It is slightly perceptible the existence of three families of curves with 2.5 N/mm² of Fsp (Figure 49B). In higher ranges of Fsp (Figure 49C-49D) the family of curves are reduced into two types.

Despite these discreet finding in the breakage behaviour, in the calculation procedure it has been detected that these differences let to noticeable parameter differences in the breakage distribution function. Table 16 shows these obtained values, divided in specific pressing force (Fsp) and in the particle size range (mm) in which the test was performed.

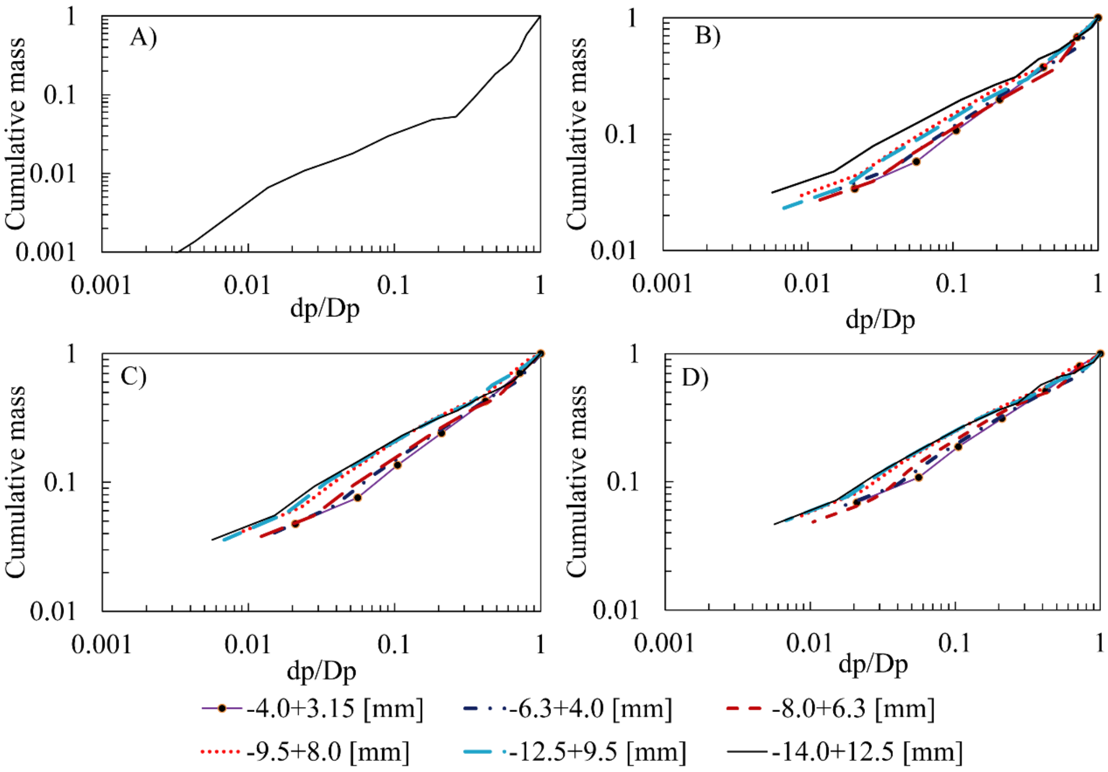

Figure 49. Results of the piston-die test at three specific pressure forces (Fsp), A) in single particle compression with 3.5 N/mm², B) bed particle compression with 2.5 N/mm², C) bed particle compression with 3.5 N/mm² and D) bed particle compression with 4.7 N/mm².

Table 16. Breakage distribution parameters obtained by the piston-die methodology for the granite from Barruecopardo for different specific pressing forces. k, n_1, n_2 and n_3 are dimensionless.

Fsp (N/mm²)	Function parameters	Fine particles (-8.0 + 3.0 mm)	Medium particles (-12.5+ 8.0 mm)	Coarse particles (-14.0 +12.5 mm)
2.5	k	0.63	0.71	0.77
	n_1	0.73	0.71	0.63
	n_2	2.36	3.20	3.72
		Fines particles (-8.0 + 3.0 mm)	Medium particles (-14.0 + 8.0 mm)	--
3.5	k	0.76	0.88	-
	n_1	0.71	0.64	
	n_2	3.20	1.93	
4.7	k	0.92	0.96	-
	n_1	0.68	0.61	
	n_2	1.60	1.40	
Single particle compression	k	-	-	0.28
	n_1			0.95
	n_2			4.02

For classification purposes, the particles size ranges between 3 mm and 8 mm were denominated as fines particles, from 8 mm to 12.5 mm as medium size particles and over 12.5 mm as coarse particles. All these denominations were assigned to the test under bed compression condition. In the case of the single particle compression condition, as the test was done in only one size range, it only has the category of coarse particles. Finally, with the values of the parameters, the breakage distribution function is modelled and presented depending on particle size range: fines (Figure 50A), coarse (Figure 50B) and single particle compression (Figure 50C), differentiating in each case for the corresponding specific pressing force range.

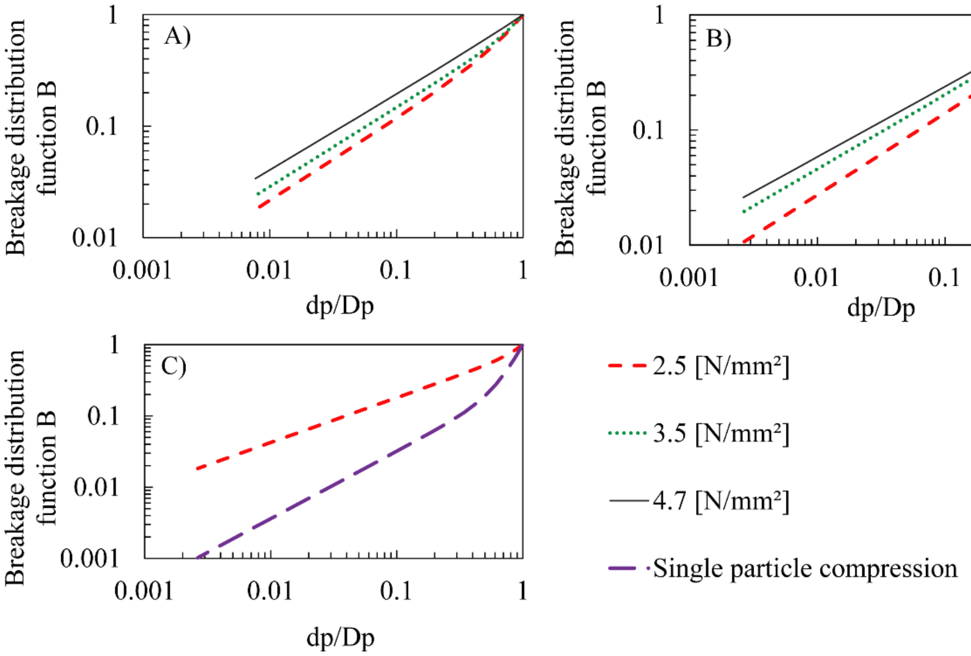

Figure 50. Breakage distribution function modeled using the parameters found with the piston die press test. A) For fines particles, B) for medium size range particles, C) for coarse range particles and for the single particle compression condition.

6.4. Lab-scale high pressure rolls crusher

The results of the experiments in the lab-scale roll crusher are shown in the particle size distribution form for inlets and outlets. The results are organized by their different operative condition in which experiments were tested: roll speed, feed size, specific pressing force and operational gap. When one operative condition is varied, all the other operative conditions are fixed.

In the case of variation of the roll speed, no change is observed in the resulted particles size distribution (Figure 51A). These results are in agreement with the total size reduction evaluation (for two representative parameters: D_{50} and D_{80}) and the relative reduction ratio between the feed and the products, when the roll speed vary (Table 17). As an example, for the experiment PV-1, the reduction is from 8500 µm to 760 µm, which is a 1/11.2 size reduction. All ratios have the same order of magnitude.

When the feed particle size vary, the impact on the resulting size distribution has no variation, in absolute values. No significant differences among the particle size product curves among experiments PF-1, PF-2 and PF-4 were observed, except by a slight displacement of around 8% of the curve PF-3 (Figure 51B). However, the reduction ratio is notable different (Table 18). This is explained by the differences on the feed size distribution.

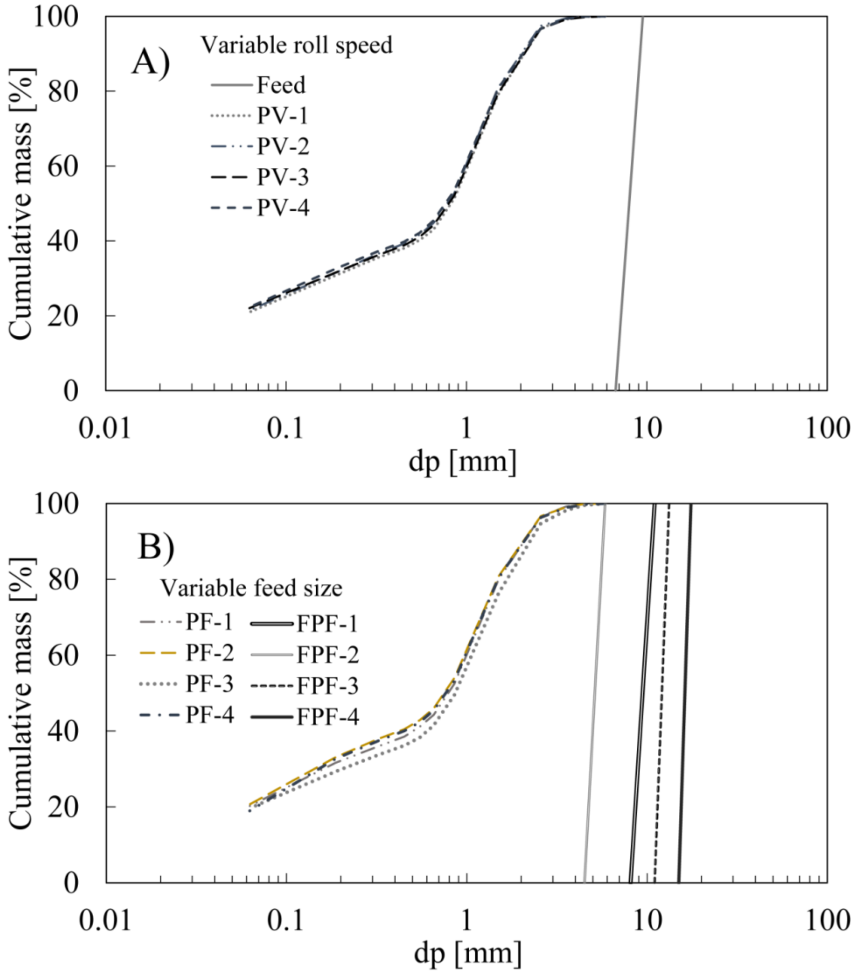

Figure 51. Results of the lab-scale high pressure roll crusher. A) when is varying the roll speed, B) When is varying the particle feed size distribution. In this case, the feed size is represented by " F" before the experiment nomenclature.

Table 17. Total size reduction and relative reduction ratio for experiments varying the roll speed, in the leucogranite material.

	Parameter	Feed	PV-1	PV-2	PV-3	PV-4
Size [µm]	D_{50}	8500	760	790	800	820
	D_{80}		1470	1480	1540	1550
Reduction ratio [1/n]	D_{50}	1/	11.2	10.8	10.6	10.4
	D_{80}		5.8	5.7	5.5	5.5

Table 18. Total size reduction and relative reduction ratio for experiments varying the feed size, with the leucogranite material.

	Parameter	Feed	PF-1	Feed	PF-2	Feed	PF-3	Feed	PF-4
Size [µm]	D_{50}	11500	795	5500	865	12750	755	17000	770
	D_{80}		1500		1480		1710		1490
Reduction ratio [1/n]	D_{50}	1/	14.5	1/	6.4	1/	16.9	1/	22.1
	D_{80}		7.7		3.7		7.5		11.4

The product of the high pressure roll crusher when the specific pressing force was varied show some differences in their curves, but they do not represent an important change in front of this operative variation (Figure 52A). The specific pressing force was set-up according the single compression strength test (Figure 43), and the maximum value of this test was applied on the experimental lab-work experiments. However, the experiment PP-1 showed a slightly better performance with a higher size reduction ratio (Table 19). The variation on the gap overture was the most sensible in terms of particle size distribution generation (Figure 52B). The gap of the experiment PG-3 was remarkable different compared the other set-up conditions.

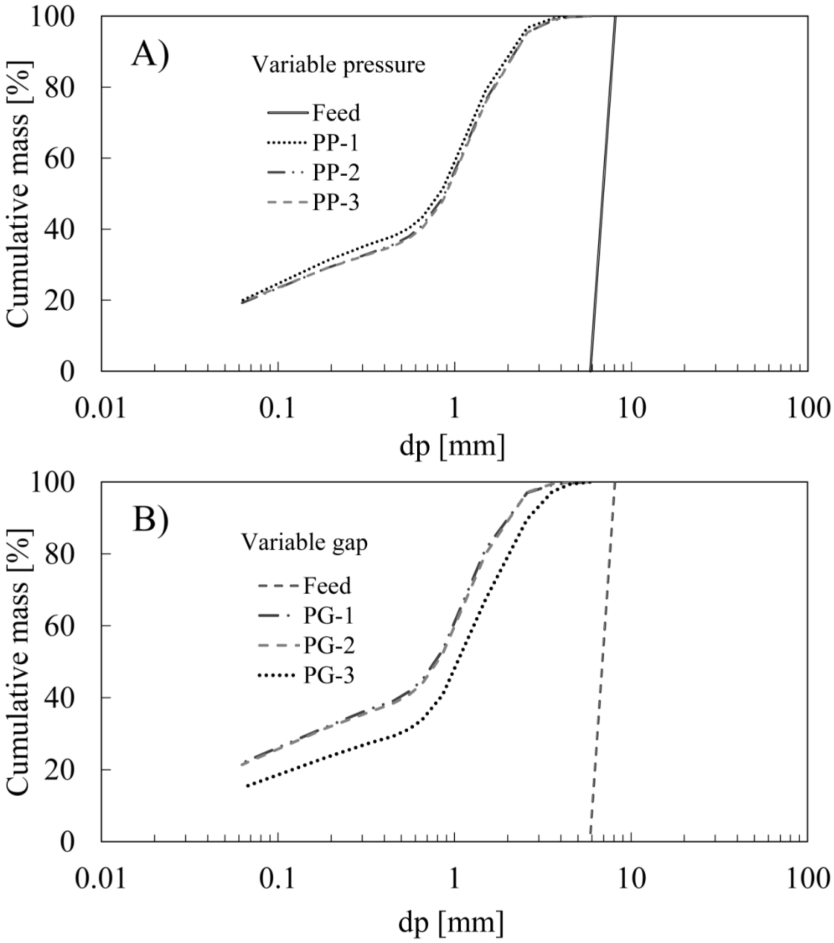

Figure 52. Results of the high pressure roll crusher, A) varying the operative pressure, B) when the feed particle size is also changed.

This differences in the curve displacement was also corroborated when the reduction ratio is compared: Experiment PG-1 and PG-2 showed similar values of the parameter D_{80} (arround 1500 µm) and the experiment PG-3 rise up until 2100 µm (Table 20).

Table 19. Total size reduction and relative reduction ratio for experiments varying the specific pressing force, with the leucogranite material.

	Parameter	Feed	PP-1	PP-2	PP-3
Size [µm]	D_{50}	8500	820	880	900
	D_{80}		1550	1700	1725
Reduction ratio [1/n]	D_{50}	1/	10.4	9.7	9.4
	D_{80}		5.5	5.0	4.9

Table 20. Total size reduction and relative reduction ratio for experiments varying the operative gap, with the leucogranite material.

	Parameter	Feed	PG-1	PG-2	PG-3
Size [µm]	D_{50}	8500	780	800	1080
	D_{80}		1450	1500	2100
Reduction ratio [1/n]	D_{50}	1/	10.9	10.6	7.9
	D_{80}		5.9	5.7	4.0

The heterogenous particle size distribution feed test (Figure 53) was performed in order to apply the observation of the mono-size experiments, with the aim to be used in the prediction model for high pressure roll crusher under a representative material. This is means, a material usually used in processing plants, non in monosize type.

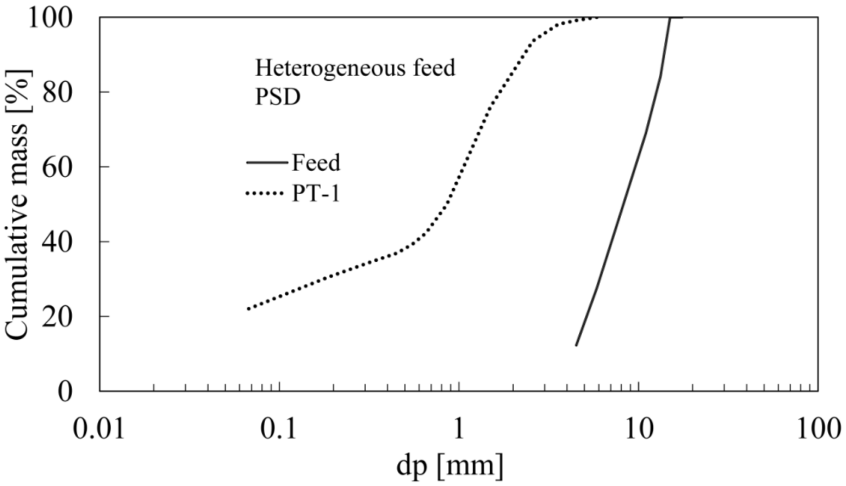

Figure 53. Penouta leucogranite experiment result of the comminution using a heterogeneous feed particle size distribution.

The size reduction was considerably high, reaching ratio values of arround 1:10 for the D_{50} parameter and near 1:7 in the case of the parameter D_{80} (Table 21).

Table 21. Total size reduction and relative reduction ratio for the experiments using a heterogeneous feed size, with the leucogranite material.

	Parameter	Feed	PT-1
Size [µm]	D_{50}	8280	850
	D_{80}	12650	1750
Reduction ratio [1/n]	D_{50}	1/	9.7
	D_{80}		7.2

The results of the experiments with the calc-silicate material from the Mittersill mine are shown in their respective operative conditions. Some variation in the product when the roll speed was varied are observed, but the were not clear enough to determine some trends (Figure 54A). All reduction parameters D_{50} and D_{80}, and also the reduction ratios showed similar values for all experiments under this operative condition variation (Table 22).

In the other hand, it is possible to observe the displacement on the curves when the specific pressing force is increased (Figure 54B).

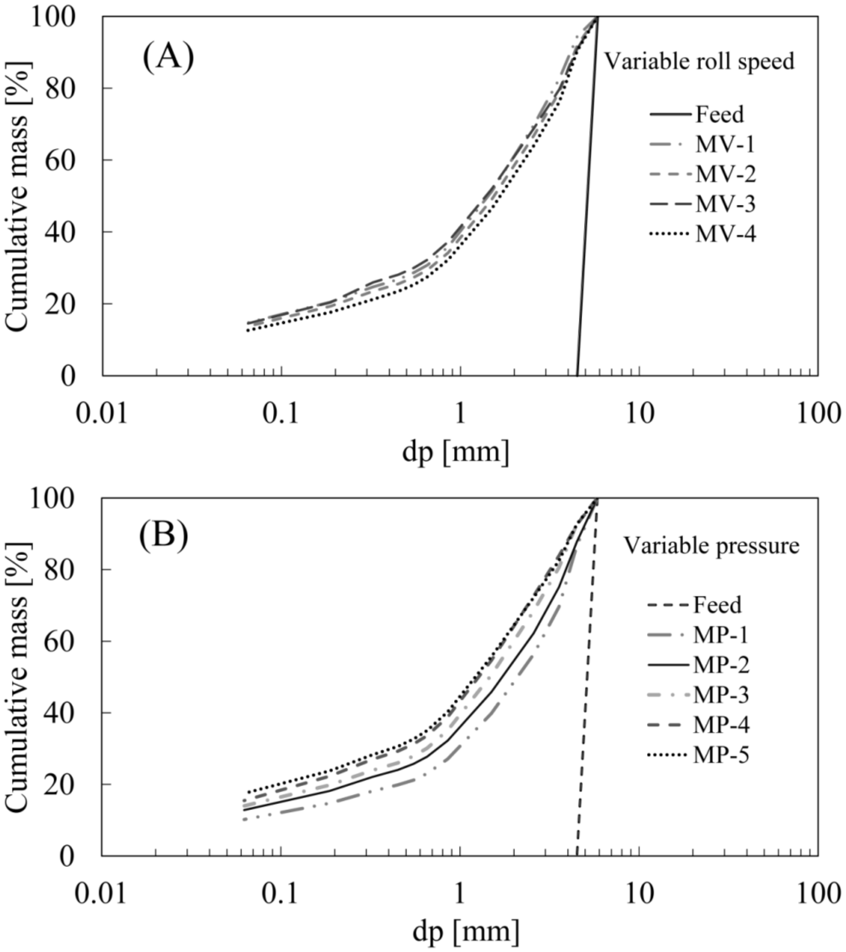

Figure 54. Calc-silicate material, from the Mittersill mine, under pressurized comminution. A) Experiments MP-1 to MP-5 showing the effect of varying the roll speed, B) Experiments MV-1 to MV-4 showing the effect of varying specific pressing force is changed.

Table 22. Total size reduction and relative reduction ratio for experiments varying the roll speed, with the calc-silicate material

	Parameter	Feed	MV-1	MV-2	MV-3	MV-4
Size [µm]	D_{50}	5000	1450	1560	1415	1710
	D_{80}		3370	3650	3600	3820
Reduction ratio [1/n]	D_{50}	1/	3.4	3.2	3.5	2.9
	D_{80}		1.5	1.4	1.4	1.3

The constant variation of the reduction parameters D_{50} and D_{80}, this is at higher values for low specific pressing force, and lower values for higher specific pressing forces respectively are consistent with the particle size distribution plots. The size reduction ratio was obviously incresed in this case (Table 23).

Table 23. Total size reduction and relative reduction ratio for experiments varying specific pressing force, with the calc-silicate material

	Parameter	Feed	MP-1	MP-2	MP-3	MP-4	MP-5
Size [µm]	D_{50}	5000	2180	1780	1570	1310	1250
	D_{80}		4150	3930	3500	3330	1250
Reduction ratio [1/n]	D_{50}	1/	2.3	2.8	3.2	3.8	4.0
	D_{80}		1.2	1.3	1.4	1.5	4.0

The experiment MT-1 was executed under controlled operative conditions, but using different feed characteristic, this is a heterougenous particle size distribution (Figure 55).

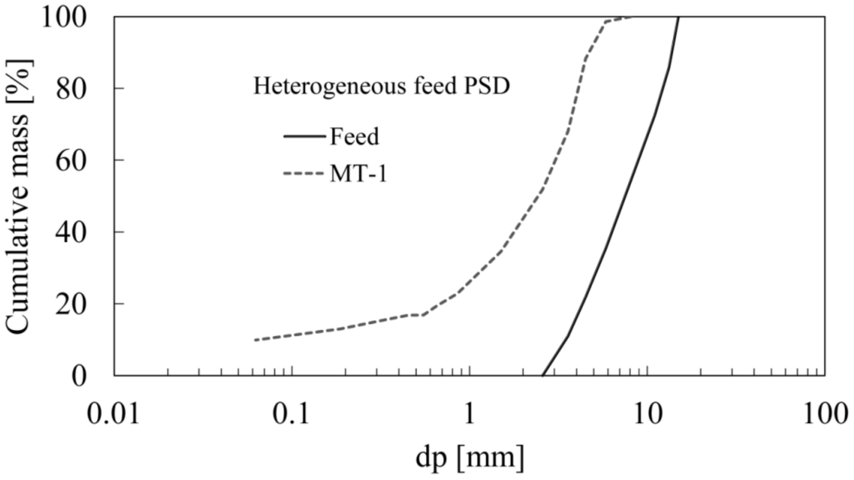

Figure 55. Result of the comminution of a heterogeneous feed particle size distribution using the calc-silicate from Mittersill mine.

The size reduction seemed more constant in all the granulometric curves, reaching similar values of D_{50} and D_{80} reduction ratio, with values of arround 1:3 (Table 24).

Table 24. Total size reduction and relative reduction ratio for the experiments using a heterogeneous feed size, with the calc-silicate material.

	Parameter	Feed	MT-1
Size [µm]	D_{50}	7580	2460
	D_{80}	12250	4120
Reduction ratio [1/n]	D_{50}	1/	3.1
	D_{80}		3.0

6.5. Breakage in industrial HPGR

The results of all sieve analyses of test made using the Köppern pilot plant HPGR in Freiberg (Germany), were grouped into six feed size categories: from group I to group V in the case of large industrial device type and the group VI, tests performed with the lab-scale device. The feed particle size distribution from the group I to IV represents mono-size feed characteristic and a last one, category V, is a heterogeneous particle size distribution type (Figure 56A). The products of these tests are shown in Figure 56B.

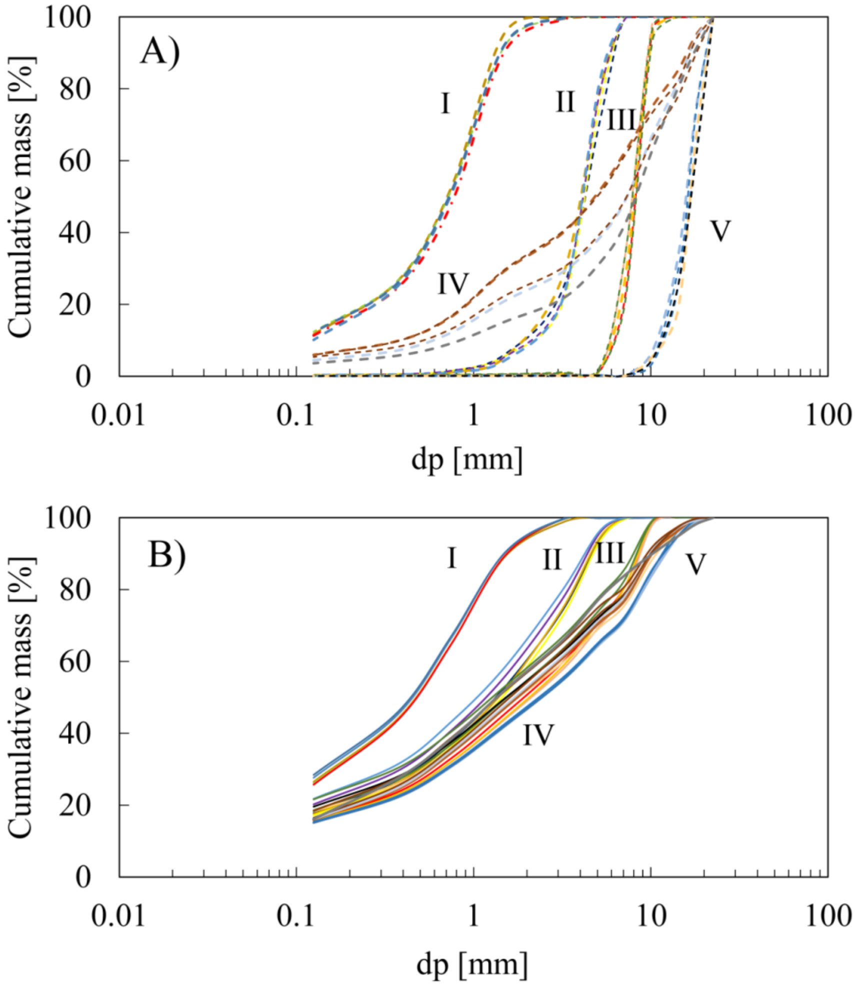

Figure 56. Particle size distribution of the test with the industrial HPGR from the Köppern manufacturer. A) feed of groups I to V, B) product of groups I to V.

In the case of the lab-scale device, the size range of the test 26 and 27 were more homogeneous and the test 28 represented the heterogeneous type (Figure 57A). The products of these tests are presented in Figure 57B.

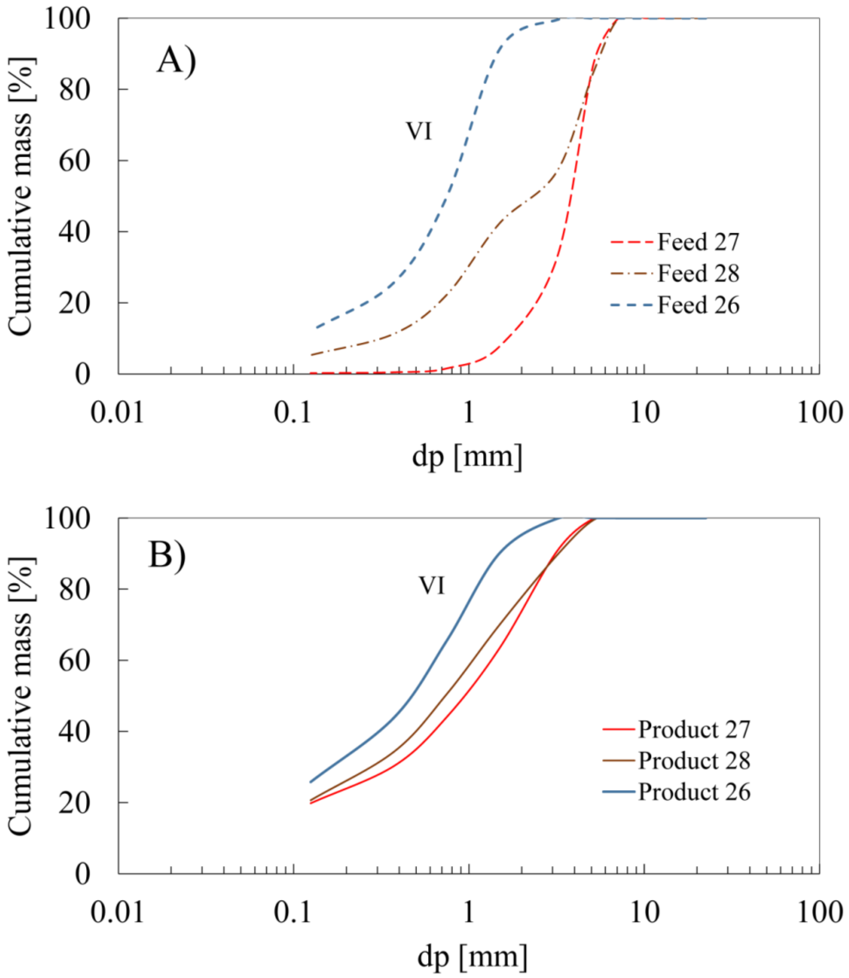

Figure 57. Results of the test executed with the lab-scale Köppern device. A) Feed particle size distribution, B) Product particle size distribution.

The size of the main parameters D_{50} and D_{80}, and their respective reduction ratio are presented in Table 25. The size reduction remains constant when the roll speed was varying. Size reduction is in agreement with this statement, with only one exceptional test 22, mainly due to the feed distribution, slightly larger than the other tests. The product size parameters decreased when the specific pressing force was raised. The reduction ratio was also increased with larger feed particle size distribution, and drastically dropped with a heterogeneous particle size.

Table 25. Main size characterization parameters of the test performed with industrial HPGR.

Category	Test number	Feed		Product		Reduction ratio 1/n
		D_{50}	D_{80}	D_{50}	D_{80}	
I	1	712	1228	480	1216	1.5
	2	723	1276	484	1212	1.5
	3	786	1315	486	1214	1.6
	4	727	1278	457	1175	1.6
	5	729	1273	446	1132	1.6
II	6	4270	5227	1337	3748	3.2
	7	4031	5224	1394	3708	2.9
	8	4245	5525	1452	3883	2.9
	9	4152	5257	1210	3452	3.4
	10	4108	5080	1084	3192	3.8
III	11	8319	9566	2038	6953	4.1
	12	7940	9364	2242	7348	3.5
	13	8196	9552	2179	6985	3.8
	14	8404	9671	1556	6474	5.4
	15	7957	9416	1319	5635	6.0
IV	16	15784	19000	2558	9180	6.2
	17	16604	20116	2553	8943	6.5
	18	16184	19105	2468	8917	6.6
	19	16716	19822	1887	8180	8.9
	20	16865	20204	1537	7433	11.0
V	21	4861	12305	1857	7838	2.6
	22	7358	13764	1780	7578	4.1
	23	4988	13201	1646	7393	3.0
	24	7314	14924	1436	6803	5.1
	25	6527	14206	1267	6032	5.2
VI	26	7510	8290	479	1189	15.7
	27	3807	4886	976	2519	3.9
	28	2378	4803	736	2355	3.2

Regarding the energy outputs, the specific energy demand W_t was obtained by the device sensing system. The throughput and the energy consumption calculation are shown in Table 26. The specific pressing force is an input that it was also measured as a way of checking the test set-up.

Table 26. Measured parameters after test-work.

Parameter	Spec. Press. Force	W spec.	Throughput	Energy consumption
Test number	N/mm²	kWh/t	t/h	kW
1	2.5	1.2	39	47.0
2	2.5	1.2	57	70.3
3	2.5	1.3	78	97.8
4	3.5	1.6	36	58.5
5	4.7	2.0	36	70.5
6	2.5	1.1	44	49.8
7	2.5	1.2	60	74.6
8	2.5	1.2	82	102.0
9	3.5	1.7	39	64.6
10	4.6	2.0	36	71.9
11	2.5	1.2	49	61.1
12	2.4	1.2	66	82.5
13	2.4	1.2	83	102.8
14	3.5	1.7	46	78.0
15	4.5	1.9	40	77.6
16	2.4	1.5	49	72.5
17	2.4	1.3	67	86.2
18	2.5	1.4	95	129.7
19	3.5	1.7	46	78.9
20	4.5	2.1	46	113.5
21	2.6	1.1	55	75.1
22	2.5	1.1	69	77.0
23	2.5	1.1	69	78.7
24	3.6	1.5	48	72.0
25	4.5	1.7	48	81.6

6.6. Lab-scale model simulation

The model was constructed with the results of the breakage distribution function and the data obtained from the lab-scale experiments with the high pressure roll crusher and the industrial high pressure grinding roll. Some other model parameters were determined empirically and, in some cases, using back-calculation techniques for better adjustment.

In a first stage, the breakage distribution function for single particle compression was analysed to define the number of N_t stages to run the model. Several simple compression stages were calculated in order to achieve this task, regardless of the selection function and avoiding the simultaneous steps of bed compression (Equation 8), and using the experimentally determined parameters of the breakage distribution function (Table 15). Figure 58 shows an example in which the top-size particles ranged from 12.5 mm to 14 mm. Since the particles have an ellipsoid shape, they tend to fit in the nip zone through their smaller radius side.

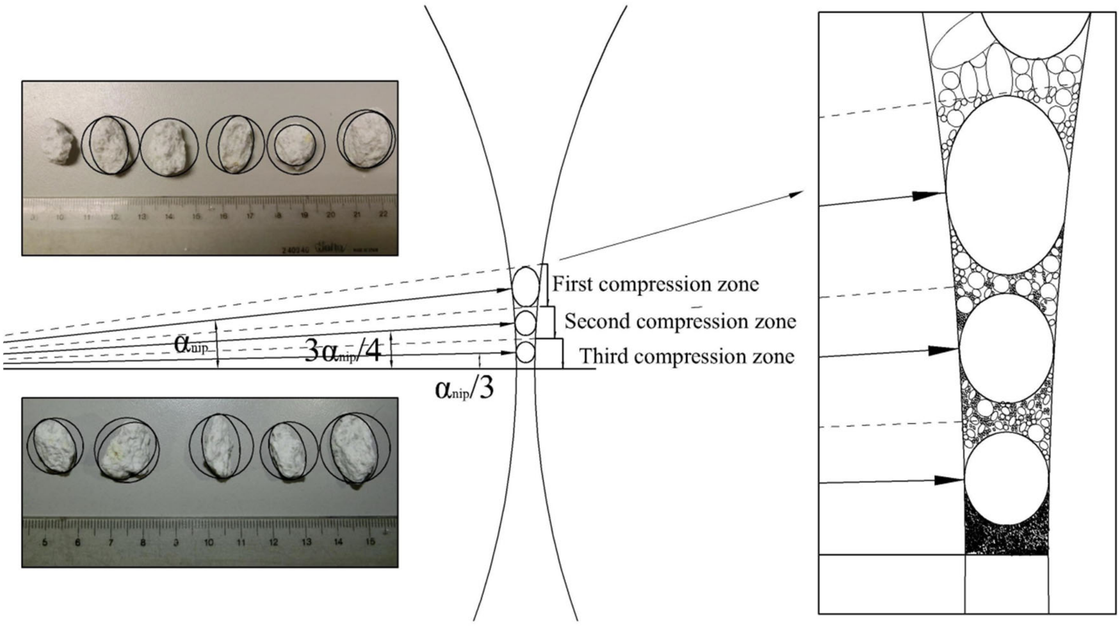

Figure 58. Shape of the particles that enters into the compression zone between roll, in the lab-scale high pressure roll crusher (Anticoi et al., 2018b).

Once the first rupture was simulated with the product P^1, more than 61% of the particles were still larger than the gap size (Figure 59), thus, it was necessary to run a second stage of compression (P^2). After three stages (P^3), the calculations showed that less than 5% of the particles were nominally larger than the gap size, and given the shape factor, most of these particles could pass through the gap between the rolls.

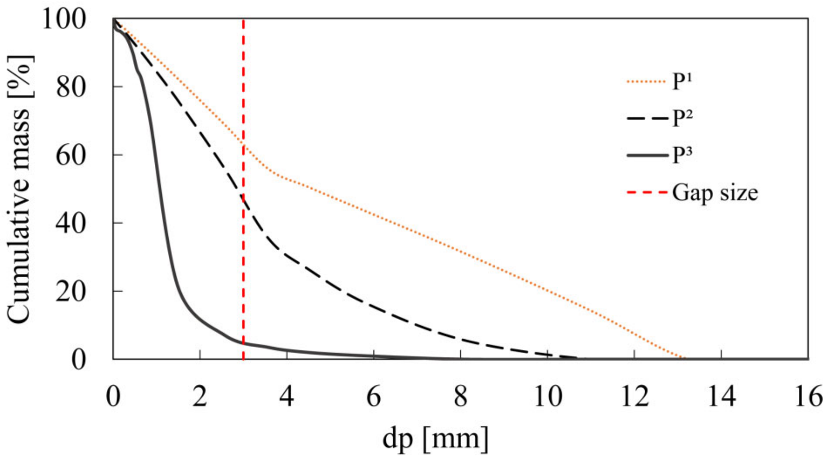

Figure 59. Loop calculation from Equation 7, leaving particles under the gap size.

The same analysis was performed on the other size-ranges for this material, with the same results; the granite had to undergo three stages of single particle compression simulation. For the calc-silicate material, as the top-feed size ranged from 4.5 mm to 6.7 mm, only two stages were necessary to reach the gap size of the product. The shape factor was also relevant to this material; angular particles have low sphericity in the near-gap size range (Figure 60). This unusual particle shape allowed a certain percentage of the population to avoid compression and still pass through to the end as a product of grinding, where the particles are even nominally larger than the operational gap, although they were not subjected to any compression or crushing action. In industrial HPGR, this is a key factor in controlling the top-size product.

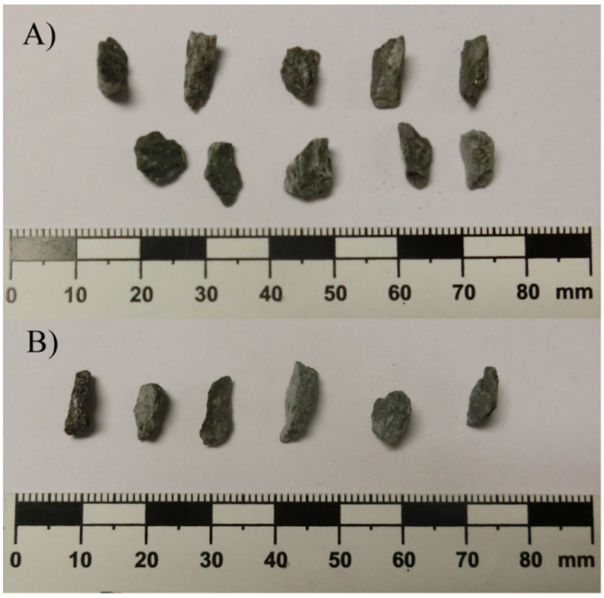

Figure 60. Size and shape of the particles that fed the high pressure roll crusher.

The model lies in the probability of particles being under single compression condition or in bed particle compression, acting both simultaneously. This phenomenon was observed during experiments, where the mono size feed (Figure 61A-B) generated a kind of cake after compression (Figure 61 C-D), which is composed by larger particles probably subjected under single particle compression and the fine phases, where the bed compression is the main comminution action.

Taking into account this statement and the previous determination of the parameter N_t, the model was executed with parameters selected from the breakage function tests, which are summarized in Table 4, using $N_t = 3$ for the altered granite and $N_t = 2$ in the case of the calc-silicate. The model variables α, x_n were calculated using the previously presented equations (Equations 4–6). The parameters d_1 and γ were adjusted according to experimental data.

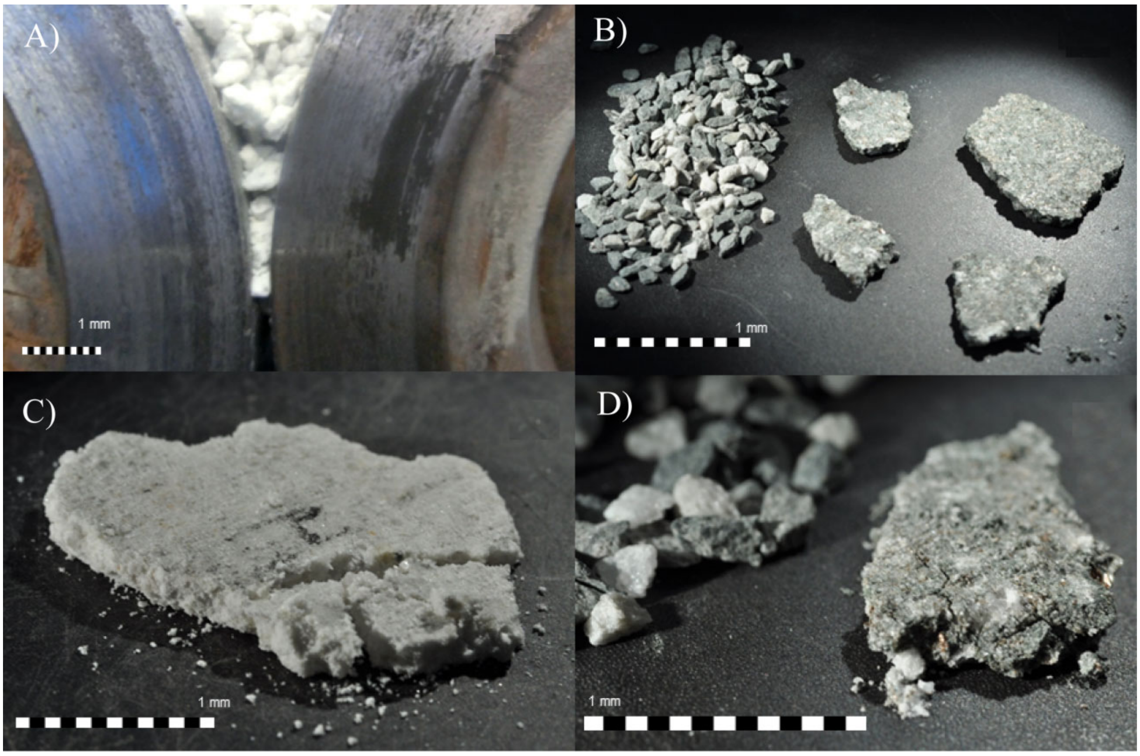

Figure 61. The cake after compression under high pressure show the interaction between single compression and bed compression action (Anticoi et al., 2018b).

Thus, the selection function was executed using the calculated parameters from Table 15 and it indicates the probability function the experiment PF-1 (Figure 62). It was observed that the first stage S^1, showed an 80% probability of single particle compression for particles over 5.7 mm, 4.1 mm for the second stage S^2, and then, this probability was applied to particles below 3.2 mm in the third stage S^3 (Figure 62). This means that all particles larger than the distance x_n had a maximum probability of being broken under single particle compression. The displacement of the curves indicated the decrease in the possibility of being submitted under the pre-grinding zone and going directly to the compression condition of the particle bed. This is the main difference with the roll crusher model, where the finer particles bypass each step and become direct products of the primary crushing.

Table 27. Calculated parameters for the high-pressure roll crusher model and the selection function for the PF-1 test. The angles are in degrees and the factor γ is dimensionless.

α	x_n (mm)	d_1 (mm)	γ
6.9	4.8	1.5	0.1
4.6	3.8	1.5	0.1
2.3	3.2	1.5	0.1

Regarding the selection function topology, as it was explained in the methodology (Equation 3), it depends on the gap, and certain boundaries conditions (parameters d_1) and mineral characteristics, γ, which gave the slope of the different stages of the function.

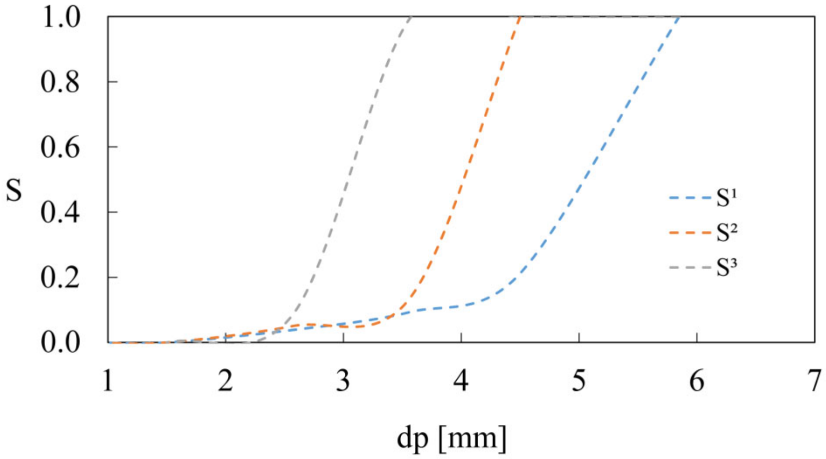

Figure 62. Selection function performance for the PF-1 experiments, using the variables previously calculated (Table 15; Anticoi et al., 2018b).

The predicted product particle size distributions for PV-2 experiment was plotted against the experimental results (Figure 63A), which shows that there is an excellent fit with the coarse phase, reaching 2.2 RMSE, despite the relative high RMSE of the fines particles, the overall error is quite good, with 6.8 RMSE (Table 28). The coarse particle prediction zone was especially accurate for the experiment PP-1, reaching only 1.1 RMSE. The calculation for the fine particle zone was also acceptable, with some discordance in the last stage of the curve, with an error of 9.0. In the case of the PP-1 experiment (Figure 63B), the RMSE comparing the predicated and the experimental result was 6.7 RMSE. For the coarse particles, the error is near to only 1.1, but in the fine particle range, the RMSE increased by about 9.0.

Table 28. RMSE for all experiment, using the Penouta leucogranite

Experiment	Total	Fines	Coarse
PV-1	6.8	9.3	2.2
PV-2	7.2	9.8	2.8
PV-3	7.1	9.8	2.2
PV-4	7.5	10.3	2.5
PP-1	6.7	9.0	1.1
PP-2	6.6	8.8	2.0
PP-3	6.9	9.2	2.2
PF-1	6.4	8.5	3.2
PF-2	7.8	11.1	3.6
PF-3	7.9	8.2	7.7
PF-4	8.6	11.7	5.4
PG-1	6.9	9.3	1.0
PG-2	6.9	9.3	1.1
PG-3	8.4	10.3	5.3
PT-1	6.5	9.4	1.6

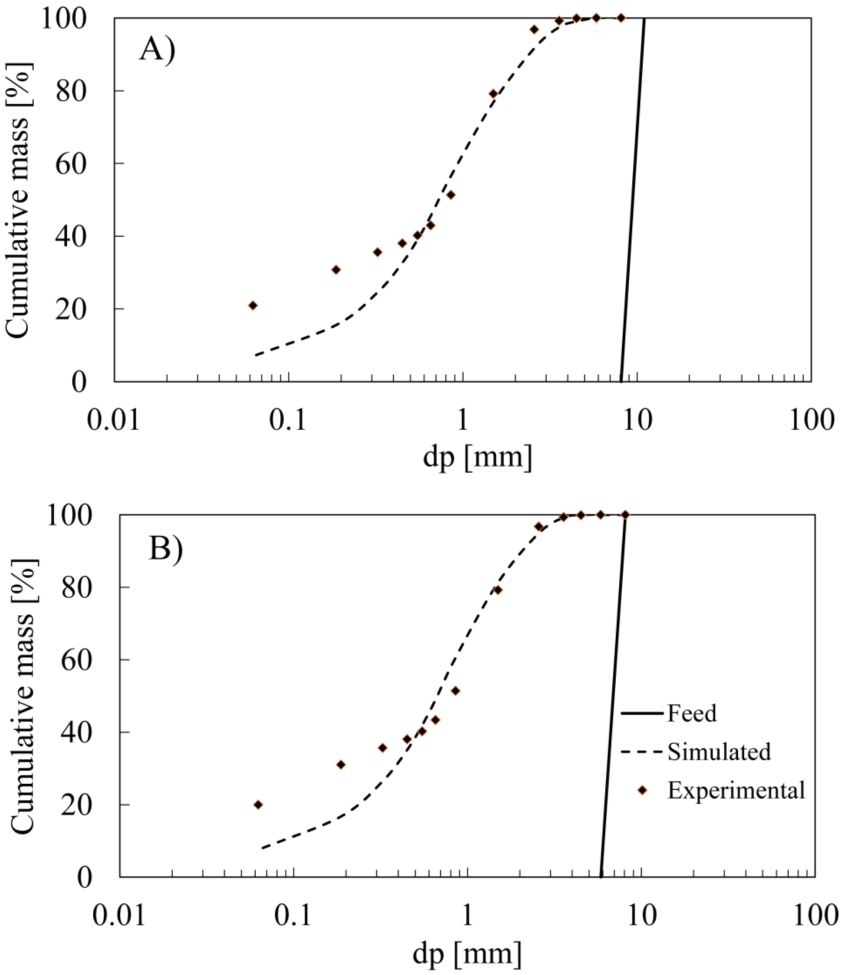

Figure 63.Comparative between model simulation and experimental results A) Experiment PV-2, B) Experiment PP-1.

With the HPGR it is possible to control the product size and material characteristics for further processing in the plant, taking into account certain needs of the process flowsheet. One key point to obtain a product with controlled characteristics is the size of the gap. Higher distance between the rolls leaves higher possibilities to have single particle compression or bed particle compression. The present model uses the gap size to predict the outlet particle size distribution. Experiment PG-1 (Figure 29A) was set with a 2 mm working gap (Table 8). The coarse particles zone prediction reached only 1.1 RMSE, being the overall measured error around 6.9 RMSE. On the other hand, the experiment PG-3 has not obtained a better fit (Figure 26B), but it was still good enough, with overall 8.4 RMSE, considering in mineral processing that the standard is between 10 % to 20 % fit error.

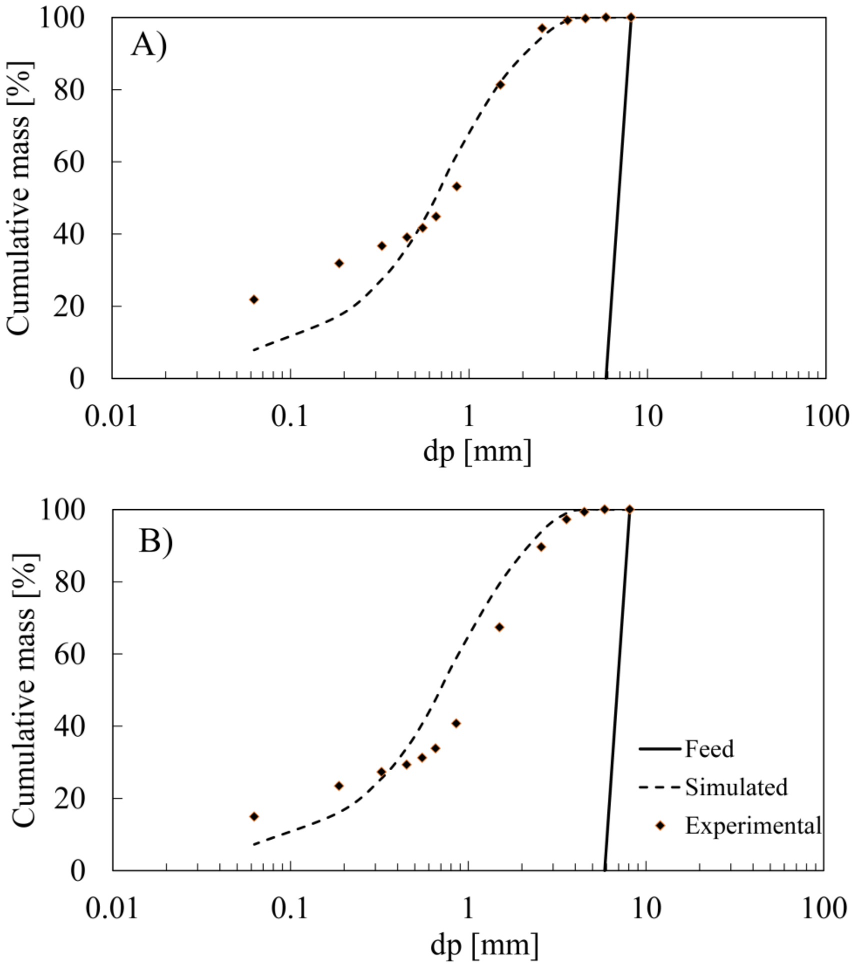

Figure 64 Comparative between model simulation and experimental results A) Experiment PG-1, B) Experiment PG-3.

Another of way to control the size of the product of the HPGR is to keep in certain size boundaries the inlets particle size distribution: controlling the feed is possible to obtain a desirable material characteristic. When the high pressure roll crushing was fed with different inlets size distribution, the model responded with a predicted product with 7.8 RMSE in the overall results, and with a coarse generation with only 3.6 RMSE (Figure 30A).

However, the challenge was to test the material with a heterogeneous material in terms of particle size distribution feed. The fit was extraordinary good for fines phases, reaching only 1.6 RMSE, despite the relative large error in the fines (9.4 RMSE), obtaining an overall difference between experimental and predicted data of 6.5 RMSE (Figure 30B).

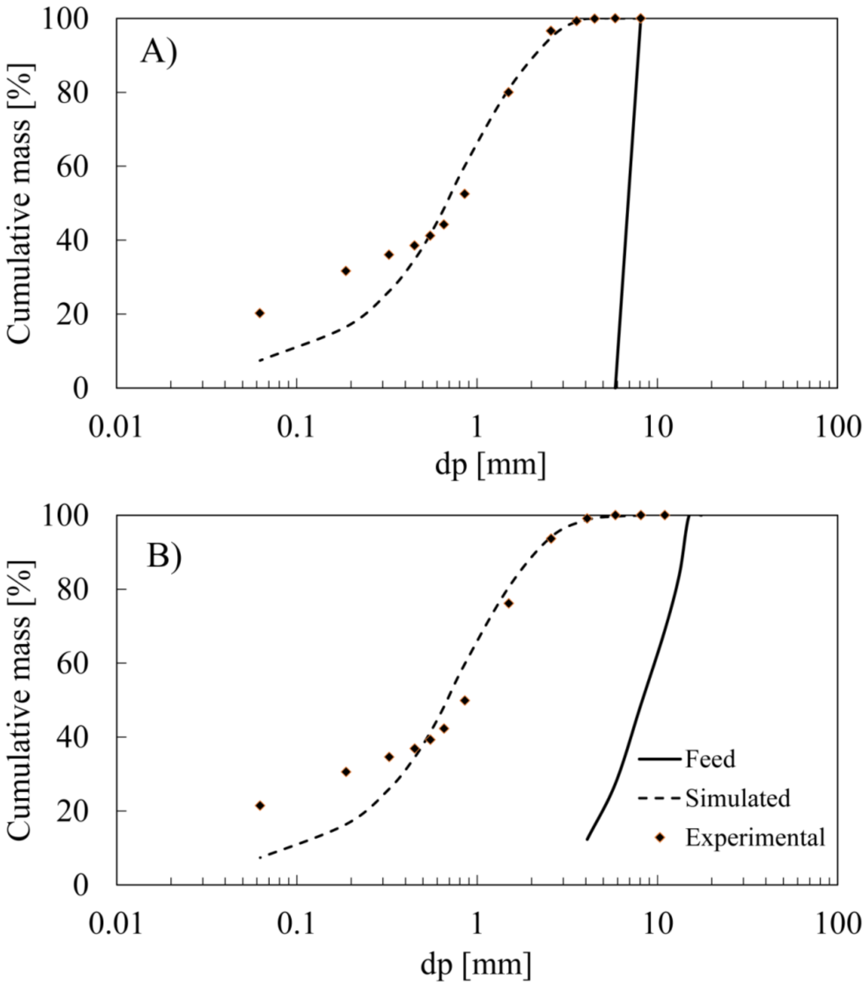

Figure 65. Comparative between model simulation and experimental results: A) Experiment PF-2, B) Experiment PT-1.

The calc-silicate material from Mittersill was used for simulation purposes. This material behaves quite different compared with the leucogranite. In terms of mechanical response, early results of the compression strength test showed relative higher values, near 900 Kg/cm², almost twice of the Penouta material values (Table 1). However, the compression strength does not give any information about the daughter particles distribution after a comminution action, but it does the breakage distribution function, which will be discussed in the next chapter. In terms of simulation, large error can be found in the coarse generation. As the speed of the roll was increased, the errors were arisen (Table 18).

The experiment MV-2 showed low error values for fines phases, near 4.1 RMSE and overall 8.0 RMSE (Figure 31A). Similar situation was observed for the experiment MV-3, which overall error reaches 7.1 (Figure 31B). In any case, the errors were under 10 RMSE, which is considered acceptable values in model prediction.

Table 29. RMSE for all experiments using the calc-silicate material from the Mittersill mine

Experiment	Total	Fines	Coarse
MV-1	6.4	3.5	8.9
MV-2	8.0	4.1	11.5
MV-3	7.1	3.1	10.3
MV-4	9.7	5.3	13.6
MP-1	14.1	8.7	19.3
MP-2	10.4	5.2	15.0
MP-3	7.2	3.7	10.2
MP-4	5.5	3.5	7.5
MP-5	6.1	4.5	7.8
MT-1	3.8	1.9	5.1

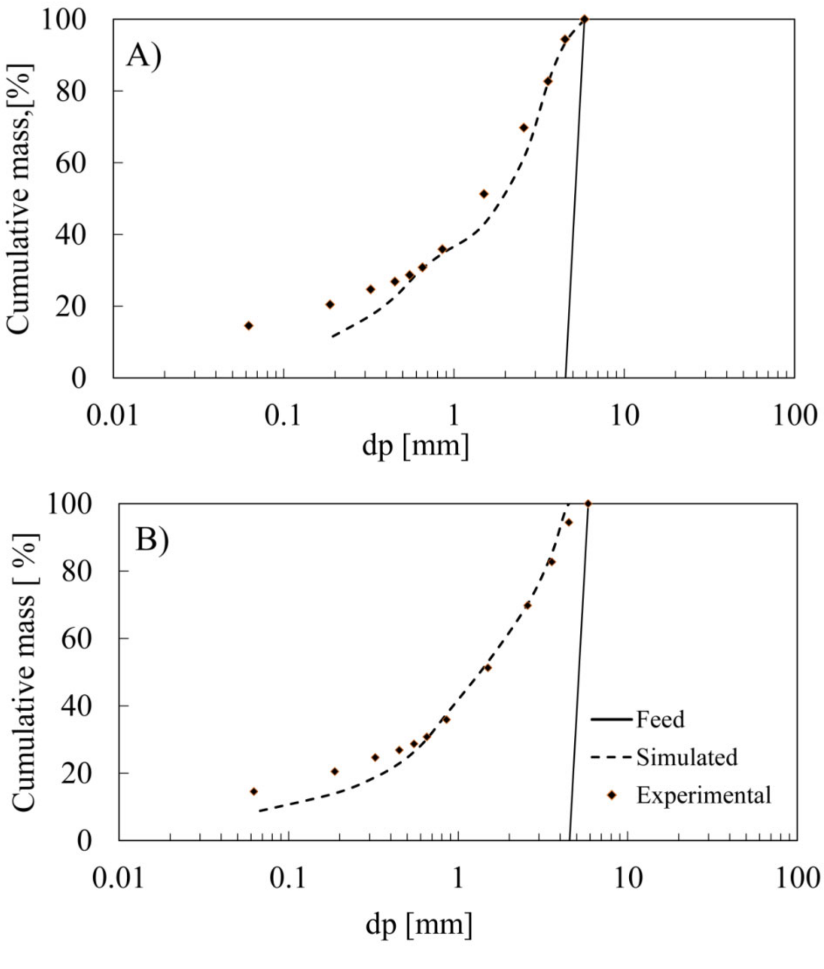

Figure 66. Comparative between model simulations and experimental results A) Experiment MV-2, B) Experiment MV-3.

However, the comparison between predicted and experimental data shows a gap for experiments when the specific pressing force is varied. In the experiment MP-1 to MP-4, the specific pressing force was gradually increased (Table 8) and this increment is indirectly proportional to the measured error: with higher values of specific pressing force, there are lesser errors compared the model prediction with the experimental data. The experiment MP-1 starts with an overall 14.1 RMSE, but it reaches near 20 RMSE in the coarse phase prediction (Figure 32A). These values considerably decreased for experiment MP-2 and MP-3 (Figures 32B-32C). The experiment MP-4 gets a minimum level of error, reaching only 5.5 RMSE (Figure 32D) but this error raise again up for the experiment MP-5, but still relatively low, with 6.1 RMSE (Figure 32E).

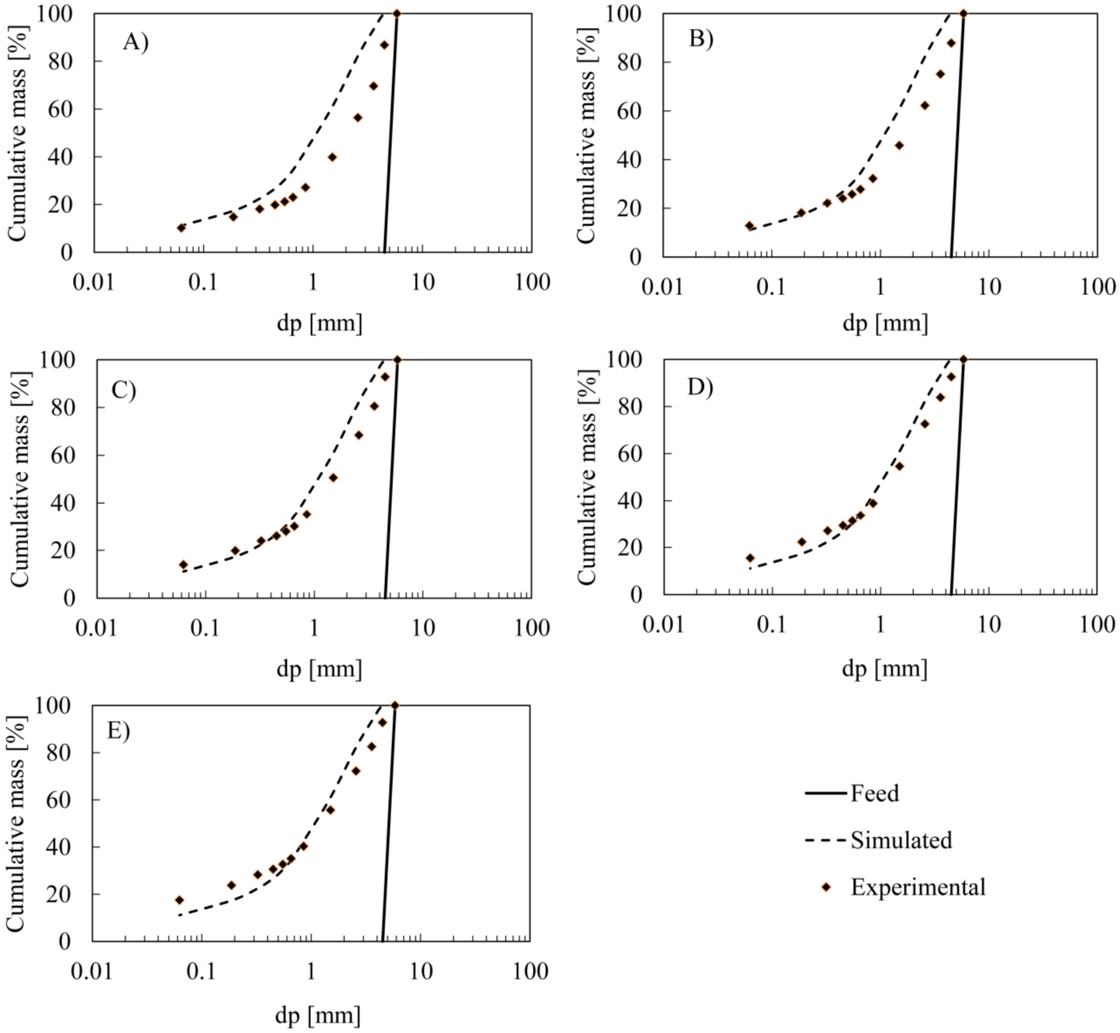

Figure 67. Mittersill calc-silicate material, experiments with lab-scale device, varying the specific pressing force, A) MP-1, B) MP-2, C) MP-3, D) MP-4 and E) MP-5.

The best fitted experiment was the MT-1, in which the feed material was not mono-size. Instead of that, a heterogeneous size distribution was used. The error reached minimum values, only 3.9 RMSE in the overall comparison and 1.9 RMSE in the fines generation. The coarse prediction was still good, with 5.1 RMSE (Figure 33)

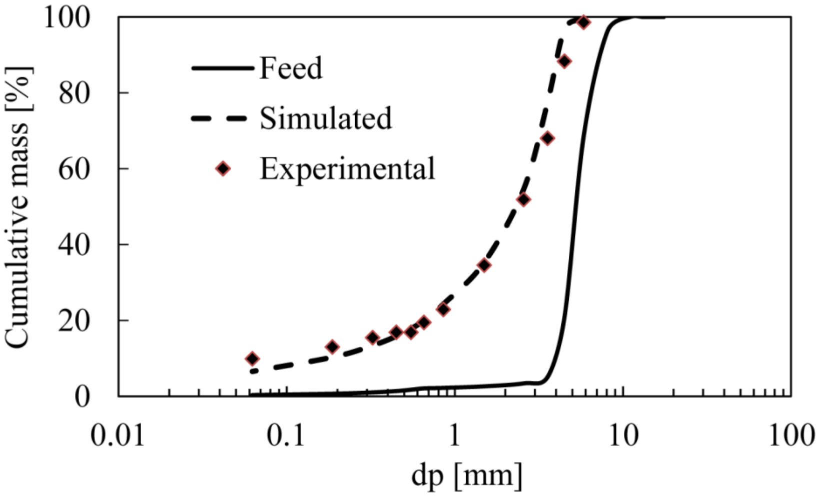

Figure 68. Predicted and experimental particle size distribution of the experiment MT-1.

6.7. Industrial scale model simulation

As a previous conclusion of the lab-scale experimental session, the influence of the specific pressing force was taken into account only to fix boundaries limits in the comminution. However, for the simulation and prediction, the experiment when varying this pressure conditions showed high values of error for higher specific pressing force. This fact impulse the decision to introduce different specific pressing force into the model, through the breakage distribution function by means of piston-die tests at different pressure level. This is why in the breakage function characterization section, two main results were shown: one for lab-scale experiments, and other for industrial scale tests. This statement was confirmed with some test on industrial HPGR when the specific pressing force was varied. The curves of the category II, from the tests 6 to 10 were zoomed (Figure 34). There is a first type of curves, when varying the roll speed. Although there is a distance between these curves, these are not as evident as are the distances between curves with different specific pressing force. This fact reaffirms the usage of different breakage distribution function parameters when the specific pressing force varies. As a result, the block scheme for the particle size distribution model predication shows a categorization according to the particle range that will be submitted under single particle compression and those that will be subjected to bed particle compression conditions (Table 6).

Furthermore, in the bed particle compression stage, the breakage function parameter values, taking into account the narrow size range, were also introduced into the calculation, using a selection function which discriminates the feed vector into the size ranges (Equation 12).

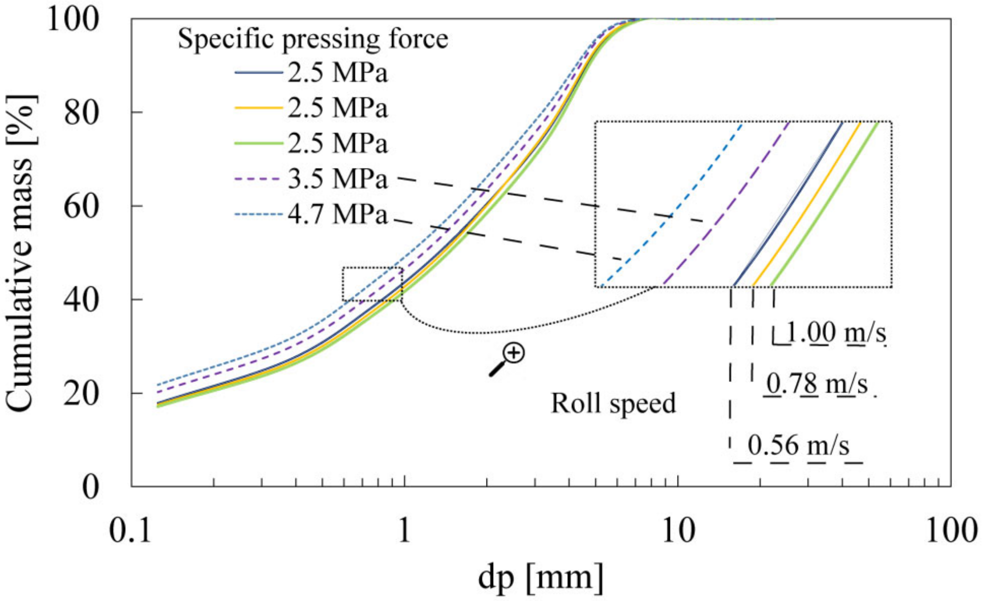

Figure 69. Test with the industrial scale HPGR from the Köppern Company, showing variation in the particle size distribution when varying the specific pressing force and the roll speed.

$$C = \begin{cases} dp < 8 \\ 8 < dp < 12.5 \\ 12.5 < dp \end{cases} \tag{12}$$

Once the model parameters from Table 10 were introduced into the calculation, plus the equation C as an extra selection function, the model was run for particle size distribution prediction. In this case, each test with a determined specific pressing force used breakage function parameter obtained from a piston-die test in that specific pressing force range (Table 5).

The comparison between experimental data and the model prediction is reflected by the Root Mean Square Error calculation (Table 19). In this case, the cut point that divided the coarse phase and the fines particles is 750 µm. The average for all tests was 6.2 RMSE of the total error and 5.4 RMSE for the fines phases.

The analyses, case by case, are also shown. The test 1 and the test 25 are two examples were the specific pressing force was changed (Figure 35A). Test 1 run with 2.5 N/mm^2 Fsp, meanwhile test 25 was set up under 4.5 N/mm^2 Fsp. The calculated error between experimental data and simulation was remarkable good, especially for the test 25, reaching only 2.1 RMSE in the overall calculation. Test 1 was also good fitted, with an overall 5.9 RMSE.

Table 30. Root Mean Square Error (RMSE) for all tests done with the industrial scale HPGR. The fines particles are the ones under 710 µm and the coarse phase is above the cut size.

Test	Total	Fines	Coarse
1	5.8	8.1	4.9
2	3.3	5.2	2.8
3	2.7	3.8	2.6
4	3.6	5.2	2.8
5	5.9	9.4	3.0
6	12.2	18.4	8.6
7	11.5	17.2	7.0
8	10.7	16.3	5.7
9	8.0	18.4	3.6
10	9.1	13.2	4.3
11	9.6	2.3	12.3
12	11.6	3.2	14.8
13	10.2	2.9	13.0
14	10.9	6.2	13.3
15	13.4	11.8	15.1
16	3.2	3.1	3.4
17	3.0	4.5	2.5
18	4.1	5.7	3.6
19	4.4	1.2	5.3
20	3.3	4.3	3.1
21	2.2	3.1	1.9
22	2.3	3.3	1.9
23	2.5	3.3	2.3
24	2.5	3.9	1.9
25	2.1	2.6	2.0
26	2.2	2.0	2.3
27	5.0	2.2	6.2
28	7.2	12.5	1.8

The test 2 and 17 (Figure 35B) were run with same specific pressing force and same roll speed, only varying the feed size. The simulation showed 3.3 and 3.0 RMSE respectively, which also represents great fitting. The prediction was remarkable in the coarse reduction zone, where the curves are almost overlapped, reaching only 2.5 RMSE for test 17. It is interesting to mention that the errors found are higher with finer feed size distribution.

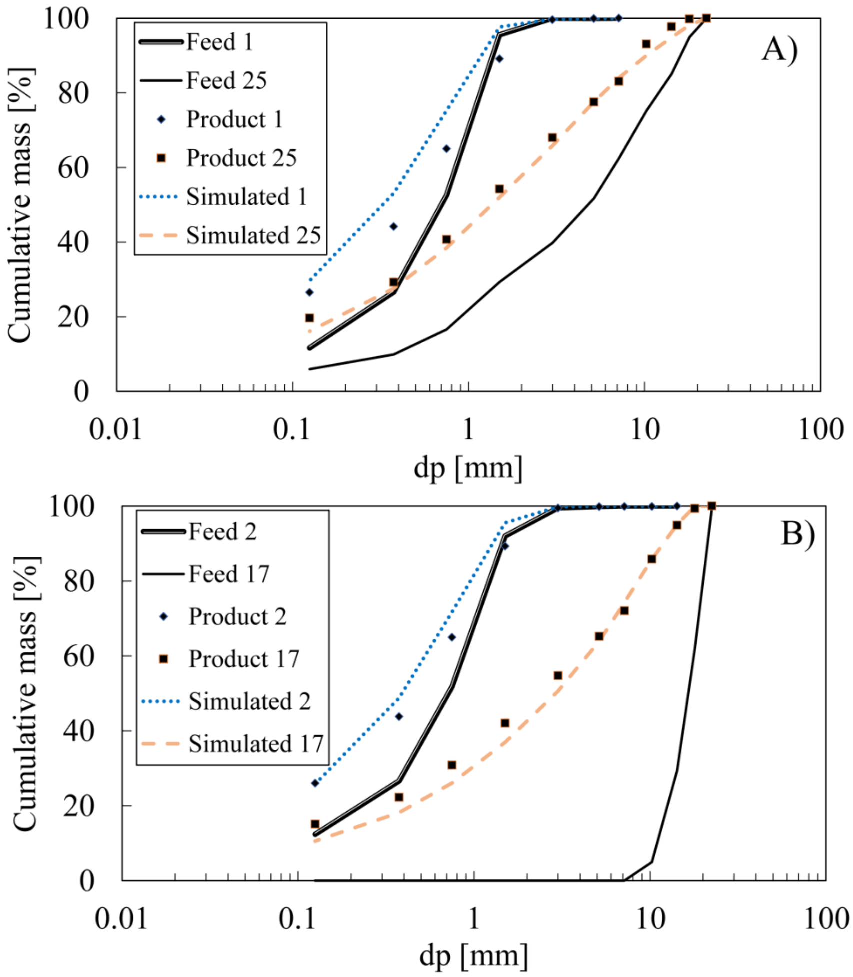

Figure 70. Comparative between model simulation and experimental results of the tests with the industrial scale HPGR, A) Test 1 and 25, B) test 2 and 17.

The test 3 was done varying the roll speed and maintaining in 2.5 N/mm² the specific pressing force. Fitting was also remarkable good, reaching 2.7 RMSE in the overall comparison, and only 2.6 RMSE in the coarse simulation (Figure 36A). When the test was done under a slightly higher specific pressing force, the case of test 4 compared with the test 3, from 2.5 N/mm² to 3.5 N/mm², the fitting was still good, reaching only 3.6 RMSE in the overall evaluation (Figure 36B).

Two main cases of excellent fitting can be observed in Figure 32. First in mono-size feed type, the test 16, which was set under 2.5 N/mm² Fsp and 0.56 m/s roll speed, showed only 3-2 RMSE. But when the feed size distribution is more heterogeneous type, the error was even lesser than the other tests, reaching around 2.2 RMSE in the overall simulation (Figure 36B). This is also observed in the test 25 (Figure 35A), with 2.1 RMSE.

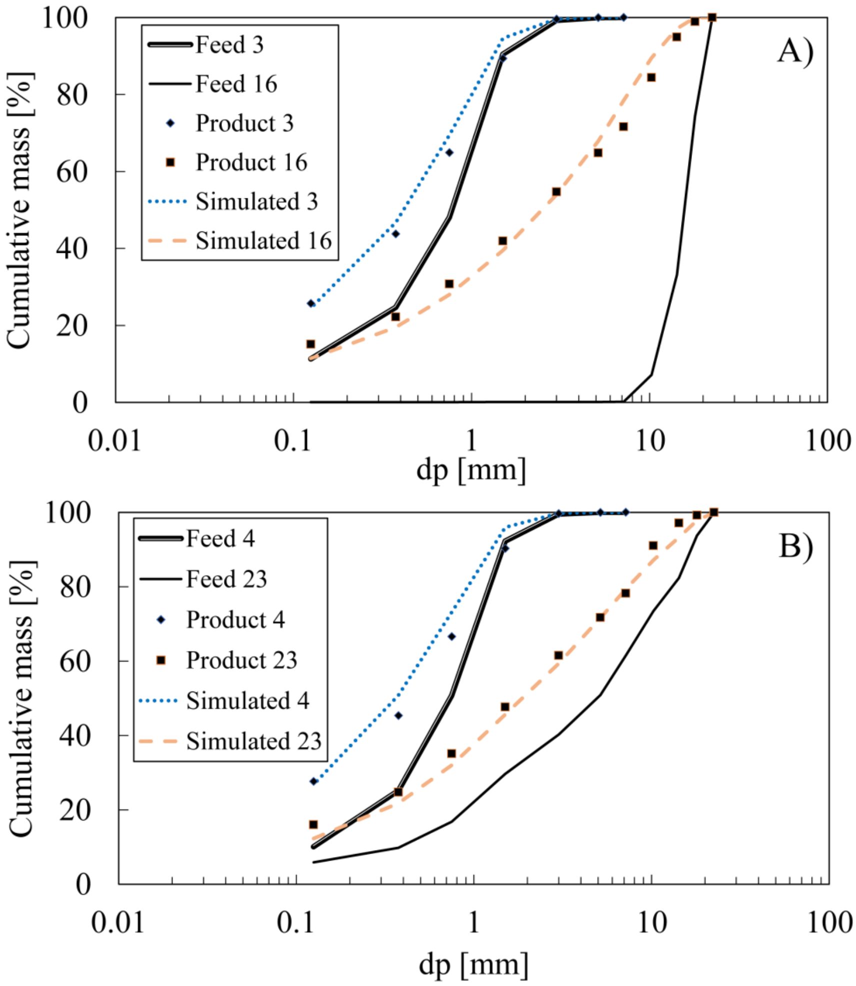

Figure 71. Comparative between model simulation and experimental results of the test with the industrial scale HPGR, A) Test 3 and 16, B) test 4 and 23

The simulation was notable effective in almost all the cases, but in the feed size distribution range from +3mm -8 mm and + 8 – 14 mm the larger errors were produced. Two tests with same operative condition are presented: test 9 and test 19, both using 3.5 N/mm² specific pressing force, 0.56 m/s roll speed. The differences in the plot of the test 9 are evident (Figure 37A). The error measurement corroborates this statement: 8.0 overall RMSE, but the fines particles generation showed over than 18 RMSE. On the other side, the test 19, using same operative conditions, but coarser feed size, range between +14 mm – 22 mm, reached 4.4 RMSE in the overall prediction, and only 1.2 RMSE in the fine generation. These result is discussed further this study.

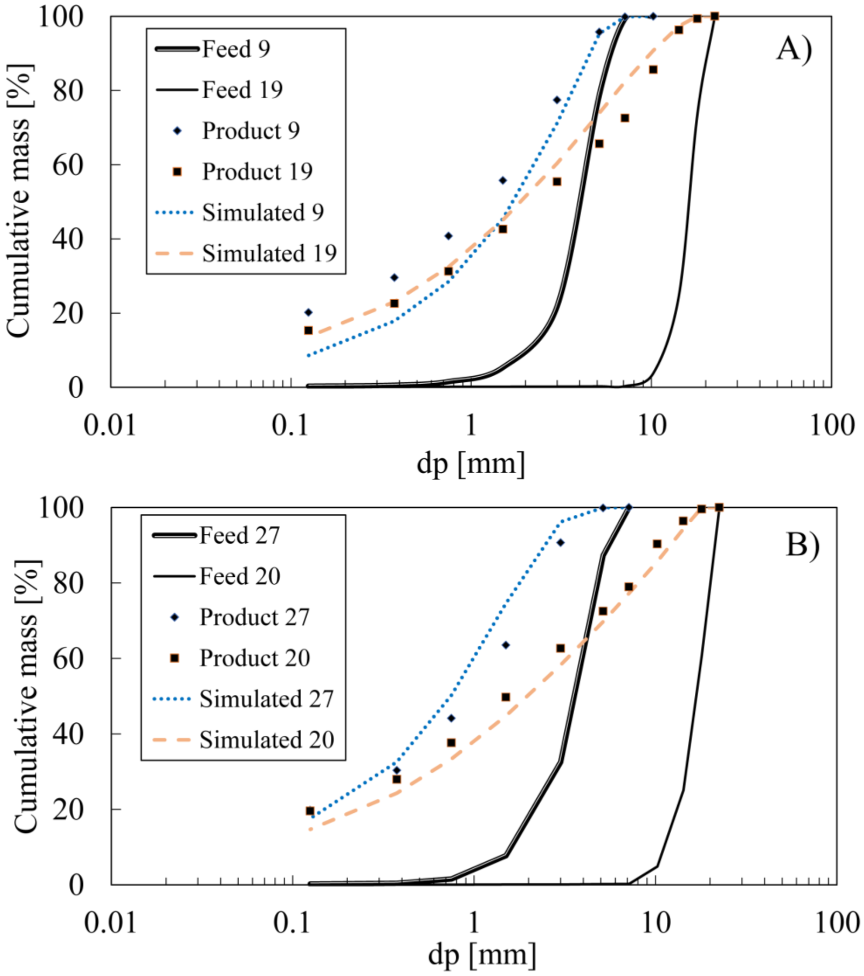

Figure 72. Comparative between model simulation and experimental results of the tests with the industrial scale HPGR, A) Test 9 and 19, B) test 20 and 27.

The prediction of the particle size distribution gains importance when is done in a heterogeneous material, since is the most similar to the material used in a real plant. In this study, several tests in mono-size feed distribution was done in order to study the affection of the operative condition in the HPGR process, but it was also designed to check the capability of the presented model in industrial conditions. Test number 24 was run under 3.5 N/mm² specific pressing force, and 0.56 m/s roll speed (Figure 38A). The feed particle size ranged between 0 and 22 mm in diameter. Overall error reached 2.5 RMSE, but in the coarse simulation was remarkable low, with 1.9 RMSE.

Test number 26 was used to compare the model presented in a similar environment in which the lab-scale experiments were performed. The device used for these tests are similar to the laboratory high pressure roll crusher previously used for model study. The UPC lab-device has 250 mm roll diameter and 50 mm roll length. The Köppern lab-scale device has 300 mm diameter and 70 mm roll length (Table 9). The error measured reached only 2.2 RMSE in the overall comparison, being 2.0 in the fines phases' prediction and 2.3 in the coarse particles simulation (Figure 38A).

Finally, Figure 38B show test 18 and 28, with 4.1 and 7.2 RMSE, representing low error compared with the rest of the tests.

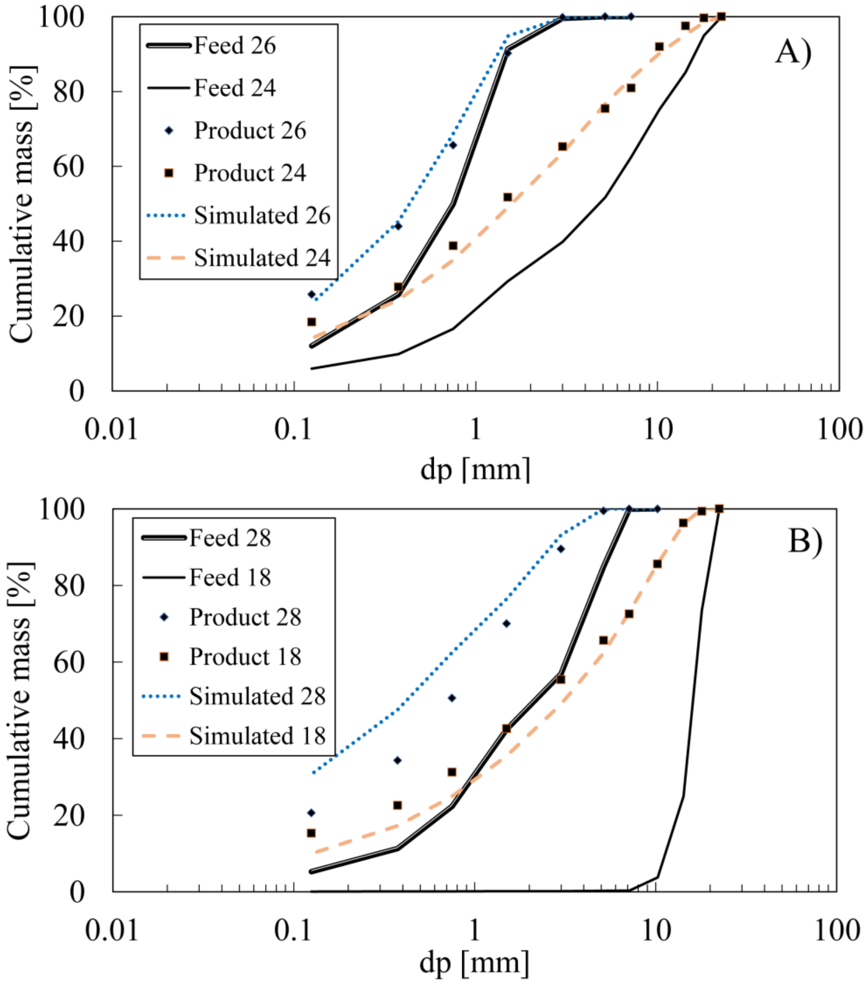

Figure 73. Comparative between model simulation and experimental results of the tests with the industrial scale HPGR, A) Test 24 and 26, B) test 18 and 28.

CHAPTER V

Discussion

7. DISCUSSION

7.1. Model related to characterization

The present study tries to determine the main material breakage characteristics, and from these features, to build a mathematical model in order to simulate or predict the product of comminution in a device in a high pressure environment. The different results were analysed individually or grouped between them in such a way to find pattern that relates mineral characteristic with breakage behaviour, or particles shapes with classification criterion.

Once the breakage distribution function was related to mineral characteristic, the model to particle size distribution prediction was presented and in this chapter is deeply analysed. Some early conclusion regarding operation condition of the piston-die test led to create a model, in this case, to re-formulate the Austin model, being more adjusted to the variation in which particles are comminuted. However, in a first stage, the specific pressing force was not taken into account in the piston-die procedure, but further experiments throughout the study impulse the adding of this specific data into de re-formulated Austin model.

Finally, the process condition was studied in order to determine the influence of several machinery inputs on the mathematical approach for product prediction. This study of model parameter dependency on operative condition was done with the validation data obtained using an industrial scale device, at Köppern manufacturer pilot plant in the University of Freiberg, Germany.

7.2. Breakage behaviour and mineral characteristic of the material

The link between the parameters of the breakage distribution function and mineralogy was established. The piston-die test was done and analysed on three different materials, especially from the mechanical point of view: the altered granite, granite and calc-silicate. Two main breakage mechanisms have been identified and tested; single particle compression and bed particle compression. The breakage function parameters resulted different when this compression condition varies (Table 4, from results). This could lead to think the mineralogy of the product could vary (in their percentage distribution, not in their composition) with the compression condition in which the material was submitted. The altered granite was a good example of this variation. Two test products from the mono-size +6.7–9.5 mm in single compression and bed compression were analysed (Figure 1). As a first clear conclusion, the particle size distribution product of a population under different comminution condition is different, and the dotted lines in single particle compression differ with the one under bed particle compression. In single compression there is an inflexion point at the size

1.5 mm (Figure 1A). On the other hand, the particle size distribution of the product in bed compression shows a linear progression of the particle size (Figure 1B).

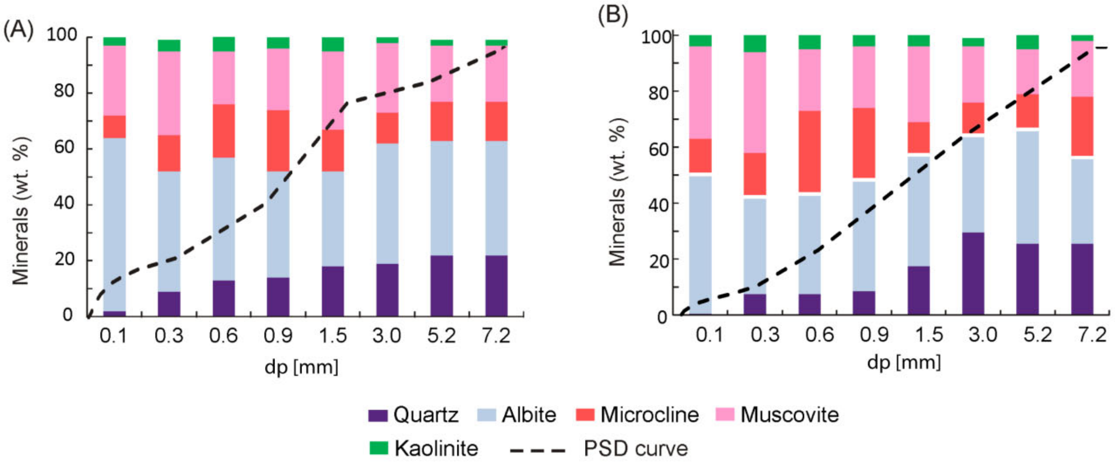

Figure 74. Mineralogy of the products of the altered granite from Penouta mine obtained in experiments under A) single particle compression or B) bed particle compression.

From the mechanical point of view, some considerations about the mineralogy are necessary. Quartz is the only major mineral from both tested materials that is resistant to alteration. It also has the highest hardness (7 in the Mohs scale). Plagioclase and K-feldspar (Mohs hardness 6) can be easily altered to sericite and kaolinite, as occurs in the granite tested ore, whereas in the calc-silicate ore plagioclase appears without alteration.

Biotite and muscovite (hardness 2-2.5) are micas with a sheet structure and perfect cleavage. Hornblende and actinolite (hardness 5-6) are amphiboles of columnar habit and cleavage in two directions.

For the altered granite, three main types of minerals, in terms of mechanical response under compression, were observed; in this case, the strongest material, quartz; the altered phase minerals include albite, microcline and kaolinite; and in the third group are the micas, which have special behaviour due to their structure and morphology. As explained in the mineralogical characterisation section, quartz is present in two main phases: grains with a size of 2 mm, and other phases of grains with sizes below 300 µm (Figure 36). In a simple fracture, larger quartz grains would maintain their size and they can be associated with the remaining altered material attached to these grains. However, there is also a smaller amount of quartz that will feed the fine fractions, but this occurs to a lesser extent. An inflexion point occurred at a size range of 1.5 mm in single particle compression condition. From the size range of 7.2-1.5 mm, the altered minerals are in the same proportion. However, from the size range of 1.5-0.1 mm, the content of the altered minerals considerably increases (Figure 75A), which affects the particle size distribution with a remarkable change in the slope of the curve. This pattern did not happen in bed compression. The higher content in quartz can be observed in the larger particles, there is not a regular distribution of the quartz as happened in the single compression test. The fines phases are fed by the altered minerals as albite and microcline. Muscovite has the same distribution behaviour for both single and bed compression (Figure 75B).

The proportion of fines is also higher in bed compression; thus this can influence the breakage function parameter.

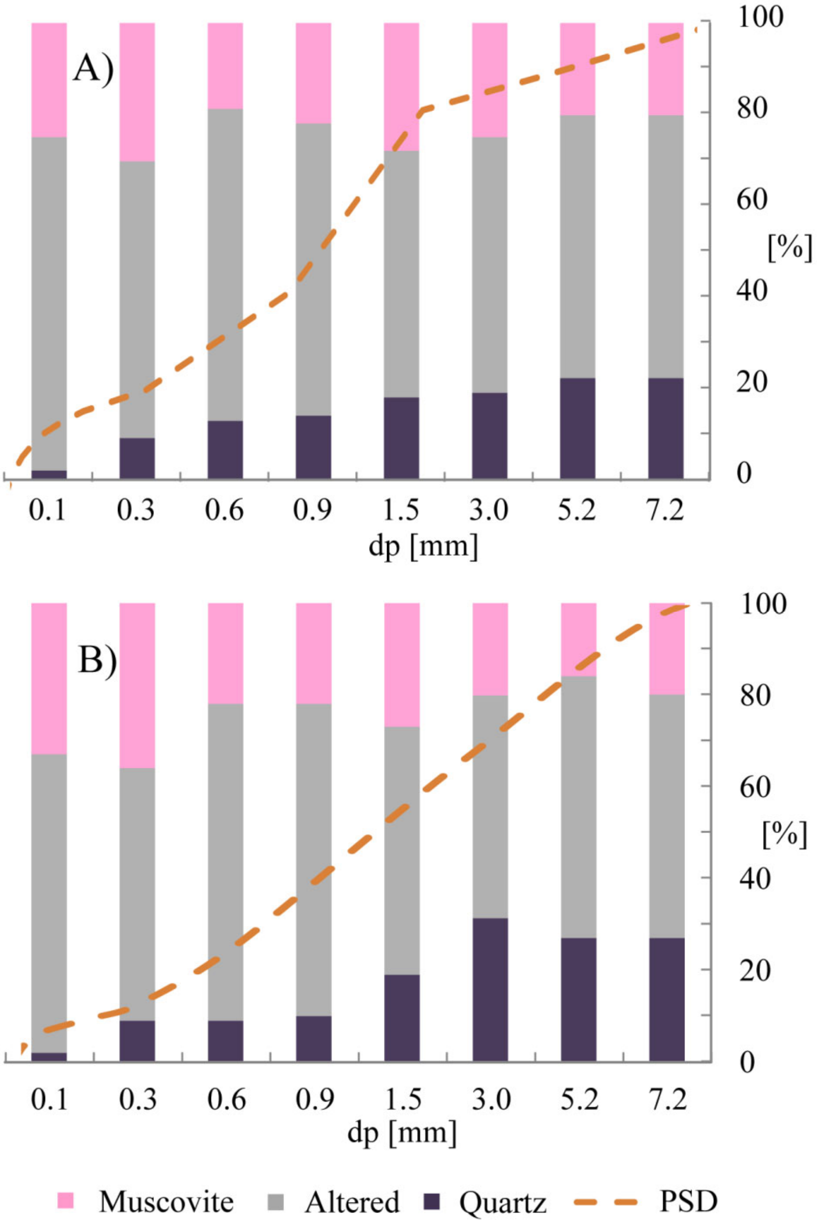

Figure 75. Mineralogy of the product of the altered granite grouped into minerals with similar mechanical response to compression, A) in single particle compression, B) in bed particle compression.

For the cal-silicate material (Figure 76), the minerals have been grouped into four types, according to their cleavage characteristics: (1) quartz, which showed no cleavage, (2) phyllosilicate minerals, mainly constituted by micas (biotite) and chlorite (chamosite) with perfect cleavage; (3) feldspars, constituted by albite and K-feldspar with good cleavage in two orthogonal directions; and (4) amphiboles (hornblende + actinolite) with good cleavage in two directions at 180°. The size distribution of the particles is related to the mechanical response of their minerals. In the coarse size class fraction, the slope of the particle size distribution curve is smoother than the finest particles.

This can be attributed to the hardness of the main minerals present in these size fractions, represented by quartz and feldspars. In the finest size fractions, amphiboles and phyllosilicates are the most abundant minerals.

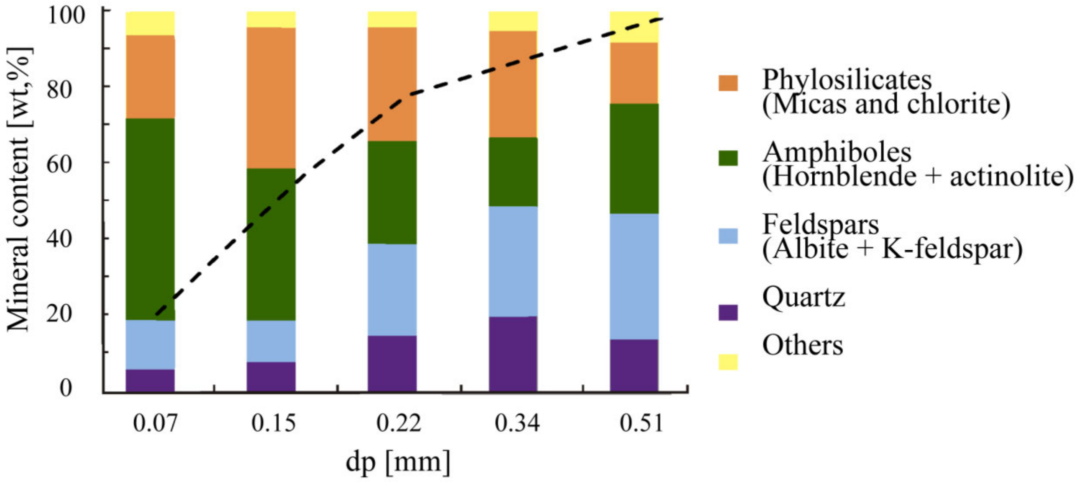

Figure 76. Mineralogy of the Calc-silicate material grouped into minerals with similar mechanical response to compression in single particle compression.

Under the effect of single compression, the evolution of the particles in composition compared with their particle size was studied (Figure 77). This progression was divided into two categories; when the particles are larger than 1.5 mm and those smaller than 1.5 mm. For the first category (Figure 77A), the altered phases and the quartz grade decreased at the same rate, given by the slope of the trend-lines, with both being at a similar order of magnitude (between 0.5 and 0.7). The decrease of these minerals was compensated proportionally with muscovite following the opposite slope progression. For particles under 1.5 mm (Figure 77B), the altered material increased at the same rate as the quartz decreased, where the slopes were almost the same but with opposite signs, one negative and the other positive. The quantity of muscovite was maintained at a constant value.

The mineral composition of the different size ranges of the particle under bed compression were differentiated into two types: In the first category, for coarse particles, the quantity of altered material decreases at the same rate as quartz (Figure 77C), while the muscovite content exhibits a positive slope, which indicates an increase proportional to the other minerals. When the particles are less than 1.5 mm, the fines particles have a lower quartz content compared with the same plot under single compression (Figure 77A-77B). Bed compression is a condition in which the full fracture is not necessary to happen. Instead, the increase in density is given by the internal structure collapse, producing micro-cracks that are not visible to the naked eye. So, the remaining particles under bed compression should have less fine proportions compared with those under single compression (Figure 77C-77D). Regarding micas, in this case, muscovite has a similar content for the different size ranges. This mineral has a sheet structure and forms flat and thin grains, being brittle in the cleavage direction. Perpendicular to the cleavage direction, the sheets can break more or less uniformly, achieving an acceptable degree of comminution. However, when pressure is exerted parallel to the cleavage, only the cleavage process is accelerated, maintaining the original size of the laminate components. Thus, the daughter generation of micas would depend on the compression contact points.

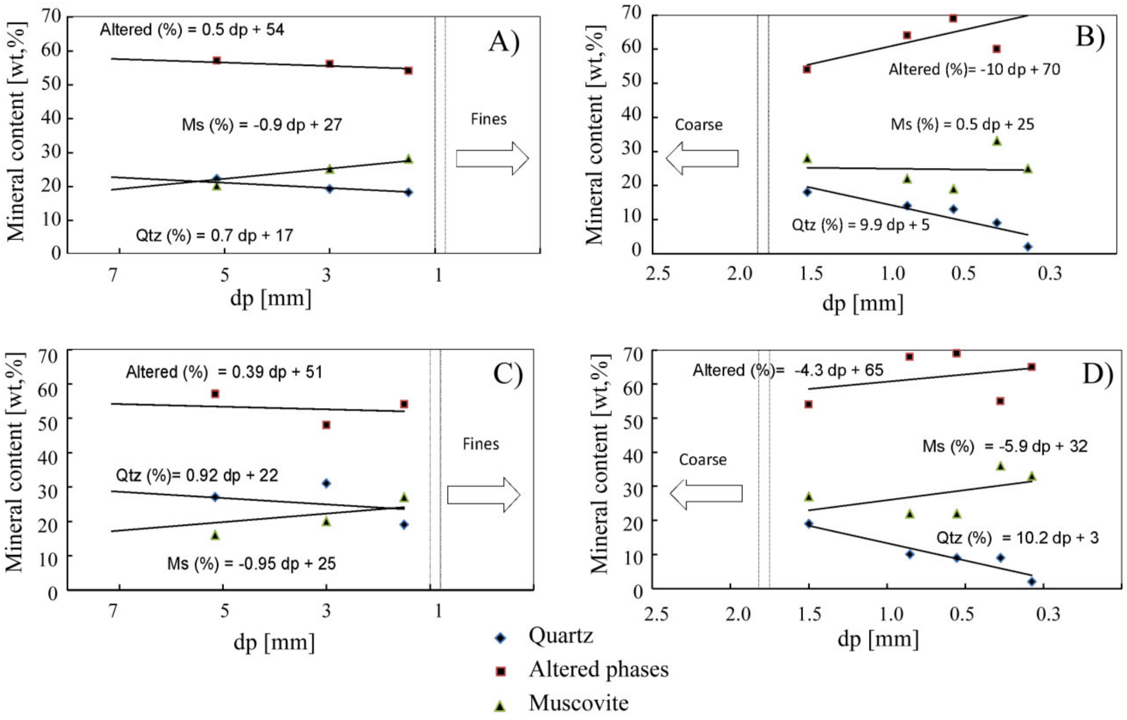

Figure 77. Mineral composition according particle size classes for the altered granite: (A) and (B) are related to the single compression test, (C) and (D) are related to the bed compression test

In terms of breakage function parameters, the referenced literature (King, 2011) discriminates two main parts of this function (Figure 78): The one responsible for the fines daughter particles generation and the other is responsible for coarse daughter particles generation. Since dp_i/dp_j is a relation between daughter and progeny particles, the parameters that characterise the mineral are: k, n_1, and n_2. The factor k has a greater ponderation when it comes to the generation of daughter fines, while n1 is a moderator of this fine generator. Thus, as values of k increase, the fine generation should increase and vice versa for low values of k. As the generation of fines daughter particles is relatively lower for bed compression compared to single compression, the values of the k factor should be slightly higher for single compared to bed compression.

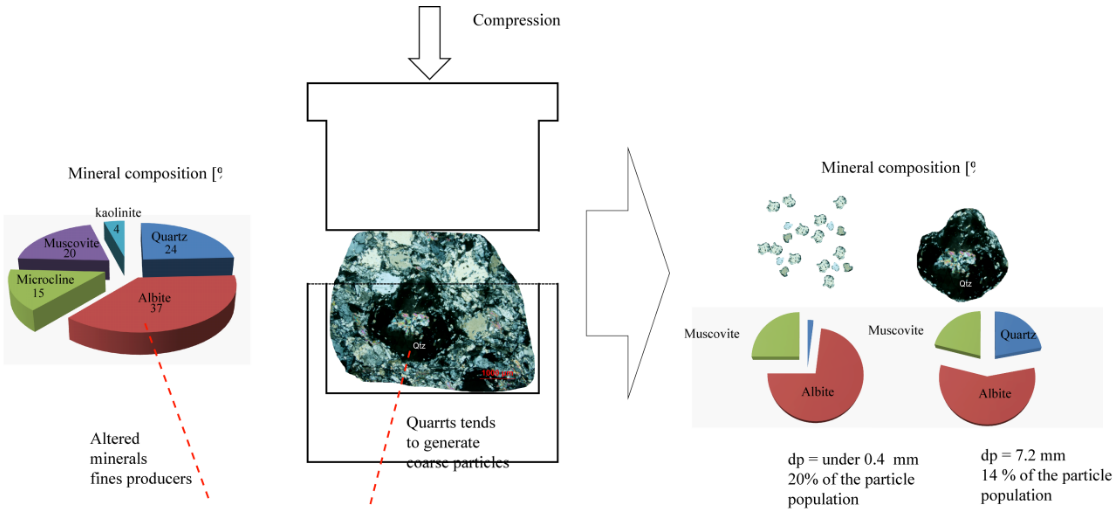

$$B_{ij} = \underbrace{k\left(\frac{dp_i}{dp_j}\right)^{n_1}}_{\textit{Fine generator}} + \underbrace{(1-k)\left(\frac{dp_i}{dp_j}\right)^{n_2}}_{\textit{Coarse generator}}$$

k	n_1	n_2
0.68	0.37	1.95

Figure 78. Breakage function distribution parameters roles in terms of daughter particle size.

Regarding parent particle composition, a significant part of the primary quartz should remain as a coarse component, and the altered phase should generate fine daughter particles. Since the percentage of the altered phase is significantly more than 50% of the whole material, this could suggest that the value of k should be greater than 0.5. It is also noticeable that the fines generation is also supported by the quartz breakage. Therefore, it is possible that this value could be between 0.5 and 1. Since the same value of k must be a little lower when it is under bed compression conditions, the experimentally found values seem to indicate this criterion (Table 15).

The calc-silicate material corresponds to an amphibolite rock. It is a more competent and stable type of rock compared to the granite, with no strong alteration. Silicates with different cleavage planes were observed, which can explain the mechanical behaviour during the compression action. In terms of composition changes for coarse phases, the contents of all minerals show small changes (Figure 79A). The inflection point occurred at approximately 400 µm; when the particle size decreases, the quartz content abruptly dropped at the same time that the amphibole content increased considerably (Figure 79B). Phyllosilicates and feldspars content varied heterogeneously with no clear pattern, despite the fact that under 400 µm, some compositional exchanges are observed (Figure 79C- 79D).

Amphibolite seemed to be more stable when responsible for daughter particles generation. The breakage distribution function curve was typical to this material. Under single compression, the internal fracture should release the minerals with a certain degree of cleavage. Quartz is hard under comminution, but it is also brittle, which means that when it reaches the collapse point, it breaks into multiple size ranges, similar to the shatter effect (Figure 79C). The composition of the particles up to 400 µm remained constant. The rock matrix does not change composition until it reaches below 400 µm, when the fines particles generation finally occurred, due to the cleavage type of the different minerals. The breakage function parameter k could reach medium values when under single compression, but under bed compression conditions should be lesser than under single compression one, generating more internal micro-cracks instead of full fractured material.

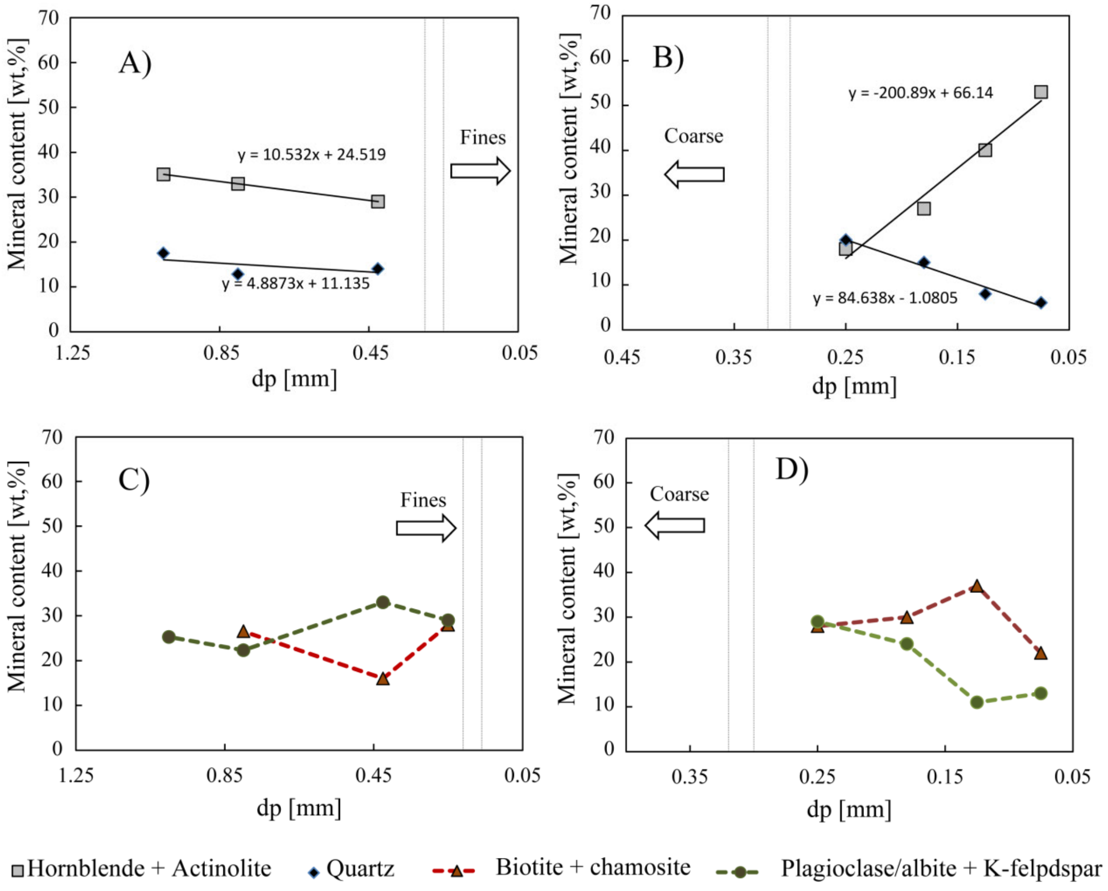

Figure 79. Mineral compositions by particle size of the calc-silicate. A) Content of amphiboles and quartz in coarse size fractions. B) Content of amphiboles and quartz in fine size fractions. ***C)*** *Content of phyllosilicates and feldspar in coarse size fractions****.*** ***D)*** *Content of phyllosilicates and feldspar in fine size fractions.*

Summarizing, three materials breakage function parameters are grouped when their values correspond to single compression condition (Table 31). The k parameter is related to the fines particles generation, and ranges from to 0 to 1. It should be higher to 0.5 for the altered granite from Penouta due to tis high content of albite and kaolinite and low content of quartz. In this case the value of k reaches 0.68. The coarse generation is governed by the same value, (1-k) and the exponent n_2. This exponent should not be higher, so the normal value of 1.95 is adequate.

The comparison with granite is inevitable. Quartz is 10 wt% more abundant and the albite is the half of the altered granite content. The grade of alteration of the leucogranite is the main reason to be a great fines generation, in opposite to the granite. This characteristic is reflected by the low values of the parameter k= 0.28 and a high value of n_2=4.2. Further research is necessary to stablish a mathematical relation between mineralogy and the breakage distribution function.

Table 31. Comparison of breakage function values and the main minerals of the studied materials. k, n_1 and n_2 are dimensionless.

SPC	Leucogranite	Granite	Calc-silicate
k	0.68	0.28	0.6
n_1	0.37	0.95	0.61
n_2	1.95	4.2	4.37
Quartz [%]	20	30	19
K-feldspar [%]	14	17	9
Albite [%]	41	21	32
Kaolinite [%]	4	4	0
Condition	Altered	Not altered	Not altered

7.3. Model construction based on the breakage distribution function

The mathematical approach presented in this study is closely linked with the mechanical characterization of the material. First of all, it was found two main breakage mechanism, single particle compression and bed particle compression. The probability of the material being under one condition or the other is particle size dependent. Then, the model computes these two different particle size populations, and simulates the comminution using the same distribution function approach, but running with different parameters for each condition. The former model, had not taken into account the specific pressing force. It was observed how the piston die test gave some variation on the breakage function parameters when the specific pressing force was varied. This fact was also introduced into the model. Finally, for different particle size range, the material also behaves slightly different, in bed compression condition.

The selection function was used to discriminate the characteristic of the particles that enter into one condition or the other. In a certain size, the particle are compressed individually or grouped in a particle bed (Figure 80).

S_i = Selection function
SPC = Breakage function single particle compression
BPC_i = Breakage function bed particle compression

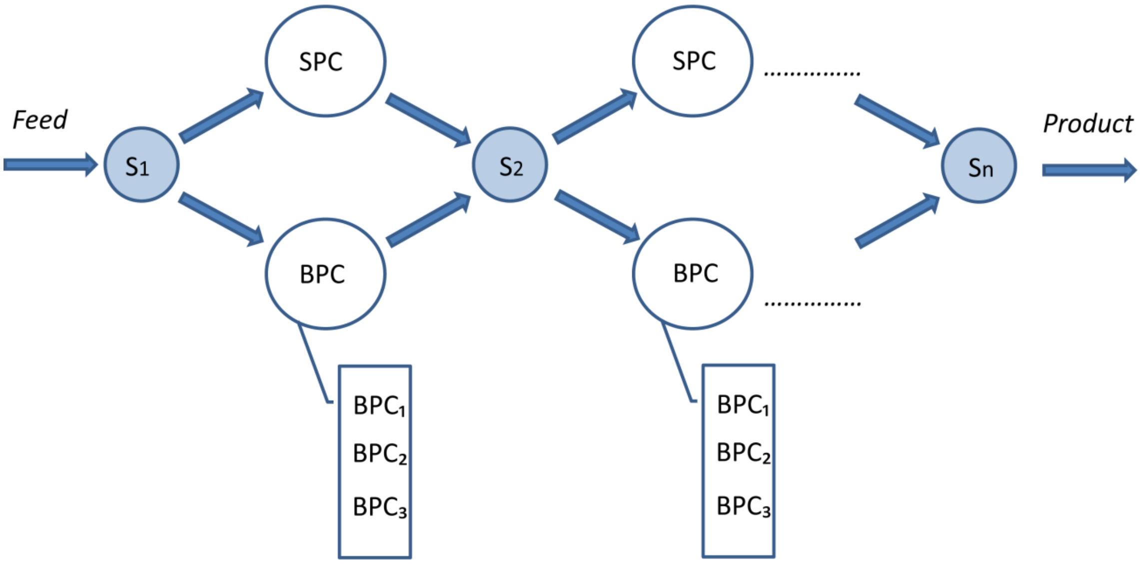

Figure 80. Model to predict particle size distribution in a HPGR.

Two cases are shown to demonstrate the influence of the specific pressing force on the model parameters. Figure 81A show the lab-scale experiment MP-1, performed with the calc-silicate material. The adjusted is clearly poor, with near 20 RMSE. Figure 81B show the experiment MP-5, using the same material, but being run under different specific pressing force. It reaches only 5.5 RMSE. The breakage distribution function was obtained by means of the piston-die test under near 4.8 MPa on the Fsp, and experiment MP-5 was done under 4.5 MPa of Fsp, but the experiment MP-1 was run under 1.25 MPa. The simulation was done with breakage function parameters under different operative condition. Figure 81C and 81D are conclusive. They represent the industrial scale tests number 26 and number 20. Both experiments were run under 2.5 MPa and 4.7 MPa respectively, and the model was simulated using the breakage distribution parameters for each specific pressing force in which the piston-die test was performed, this is 2.5 MPa and 4.5 MPa. Both tests were simulated with their respective parameters under their respective specific pressing conditions. Error in both cases was less than 3.3 RMSE.

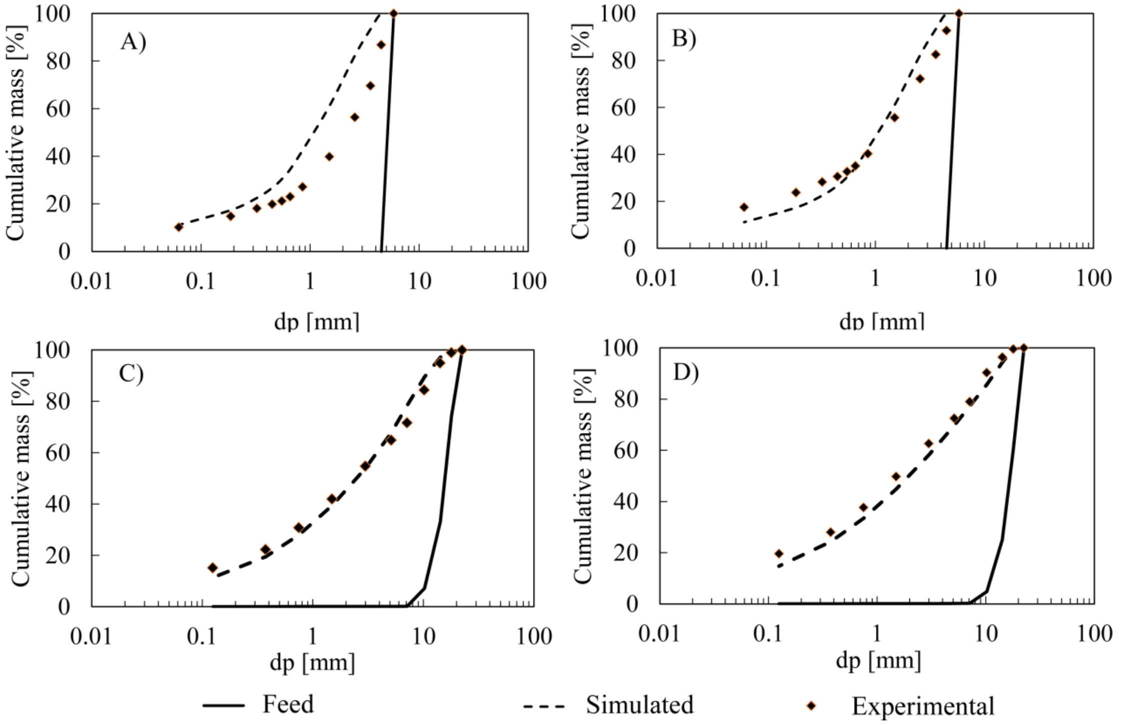

Figure 81. Comparison of different experiments with adjusted Fsp or not adjusted Fsp. A) Lab-scale experiment MP-1, B) Lab-scale experiment MP-5, C) Industrial scale test number 16, D) Industrial scale number 20.

The model show consistency among different pressing input, as it was conceived and presented in the methodology and results chapter. In Figure 82A (Test 8, 9 and 10) is observed how the specific pressing force has an influenced on the resulted particle size distribution. The simulation using the present model translates this behaviour, using the correct breakage distribution function obtained experimentally (Figure 82B). The test 23, 24 and 25 were predicted under this model simulation, and the displacement between the curves represents the capability of the model to process this pressing input.

Among all the tests, those performed using a heterogeneous feed particle size distribution could be considered the most important ones, because they represent what really happen in a real process. These simulations are presented in log plot, showing two size characterization parameters: the D_{50} and the D_{80}, and the percentage error between the simulated value and the real value (Figure 83). They are ordered from the test number 21 to test number 25. From test 21 to test 23, the variated operative condition was the roll speed. In those cases, the variation on the particle size distribution of the product was very similar among them. For example, the test 21 has a D_{80} of around 7000 µm (Figure 83A); meanwhile the test 22 obtained only 7050 µm in its D_{80} value (Figure 83B). The throughput is the variable output in this case: 42.5 t/h in the test 21 (Figure 10A) increased until 78.6 t/h for the test 23 (Figure 83C).

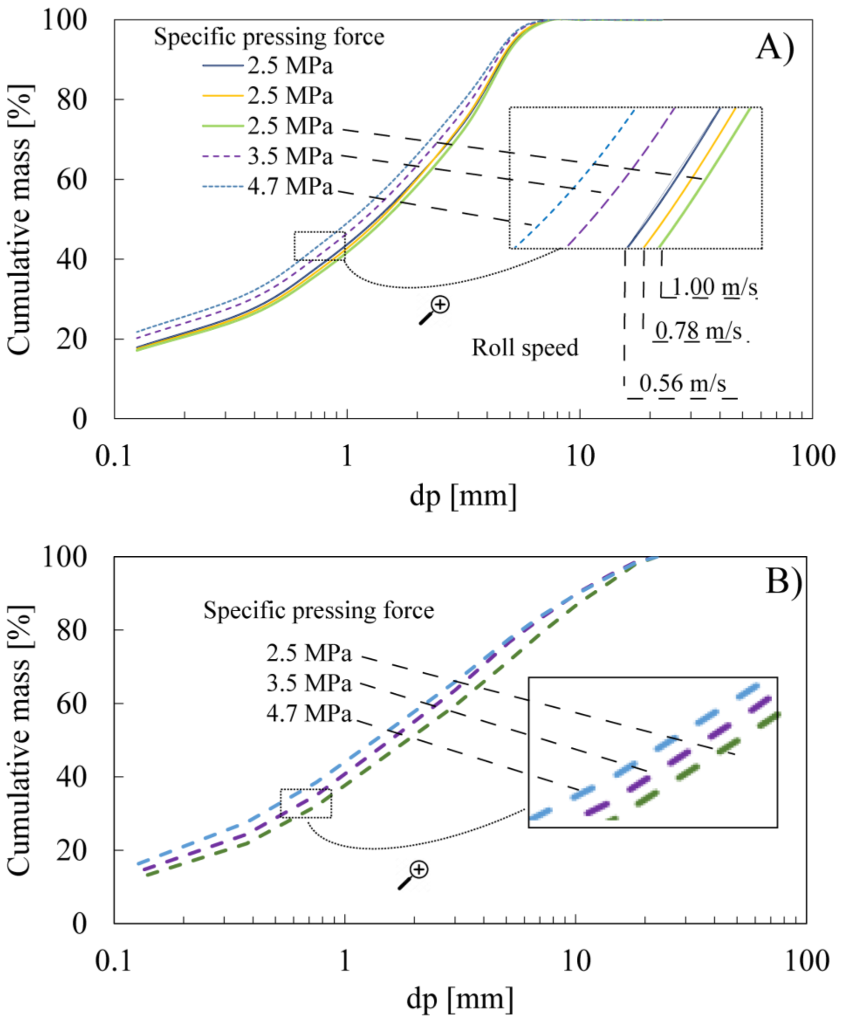

Figure 82. Specific pressing force influenced in the A) Experimental data obtained from the test in the industrial scale HPGR, B) Pure simulated curves using the industrial scale tests inputs.

From test 23 to test 25, the variable was the specific pressing force. The progressive reduction on the characterization size parameters is also evident, showing a D_{80} of around 7400 µm for the test 23 (Figure 83C), being 6100 µm for the test 24 (Figure 83D) and reaching only 6000 µm in the test 25 (Figure 83E). Those variations are considered well simulated, since in mineral processing is pretty common to have near 20 wt% error in product prediction with the current models.

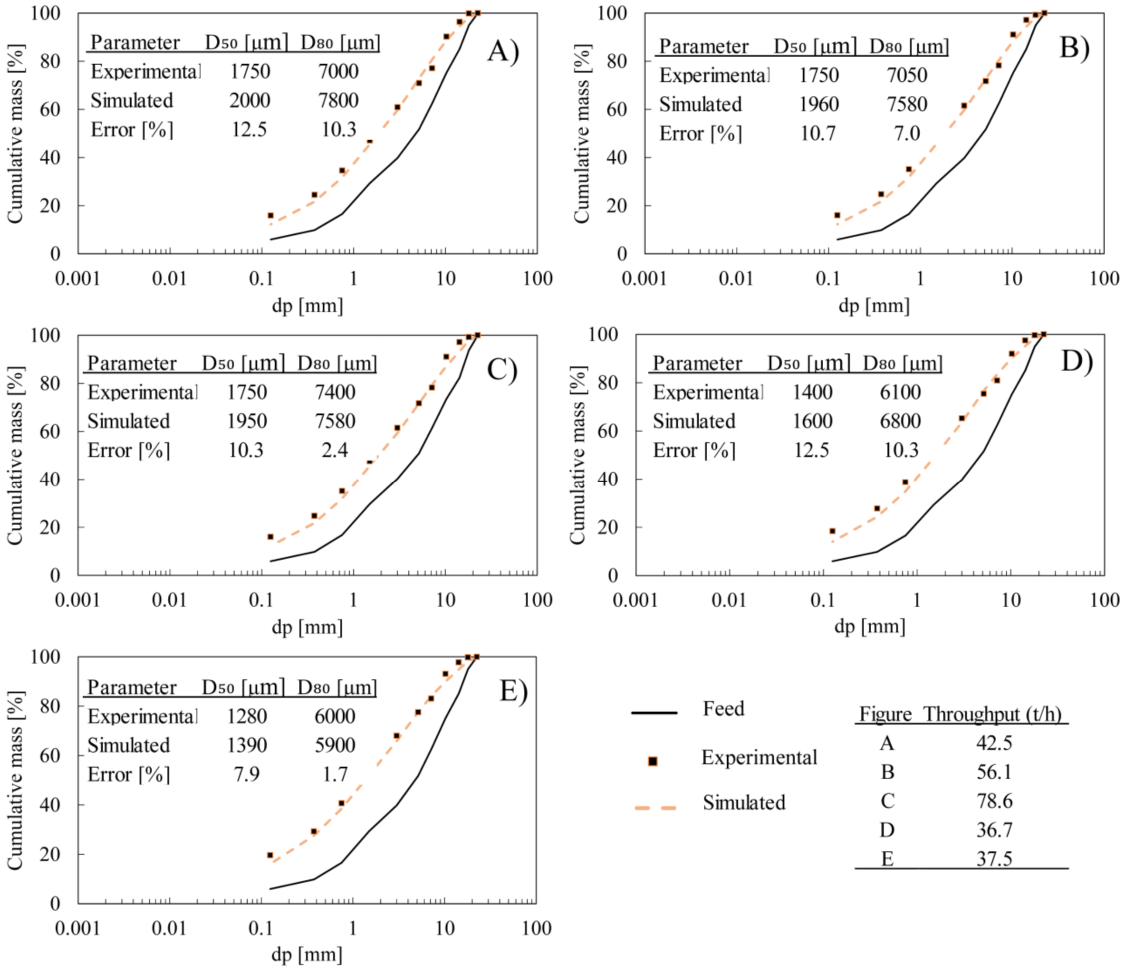

Figure 83. Analysis of test performed with a heterogeneous feed particle size distribution. A) Test 21, B) Test 22, C) Test 23, D) Test 24 and E) Test 25.

7.4. Operative conditions analysis

7.4.1. Breakage function parameters dependent on specific pressing force

The model for HPGR presented in this study is analysed and compared with the operative conditions and how it influences on the breakage distribution function parameters. This link can be observed in Figure 11. The k parameter, which is defined as the main fine phase producer in a breakage event (King, 2001; Anticoi et al., 2018), increases with the specific pressure for all particle size ranges (Figure 84A). The parameter n1 is also responsible for the fine generation, but it has more influence on the quality of the slope of the curve generated by the distribution function (King, 2001). The variation of the parameter n_1 is minimal, and it has no influence of the specific pressing force, as can be observed in Figure 84B. Some studies define this parameter as material characteristic dependent (Kelly and Spotiwood, 1990; Chimwani et al., 2013).

In parallel, if the parameter k is related to the generation of fines, the form 1-k should refer to the generation of coarse particles, and so does the parameter n_2. This parameter varies with respect to the specific pressing force, and consequently, n_2 must be inversely proportional to the applied specific pressing force (Figure 84C).

Regarding the relationships among the parameters and with the different mono-particle sizes determined in this thesis, the parameters k and n_2 increase directly with the parent particle size at 2.5 N/mm^2 of specific pressing force. Meanwhile, the parameter n_1 remains constant for all particle size types (Figure 84D).

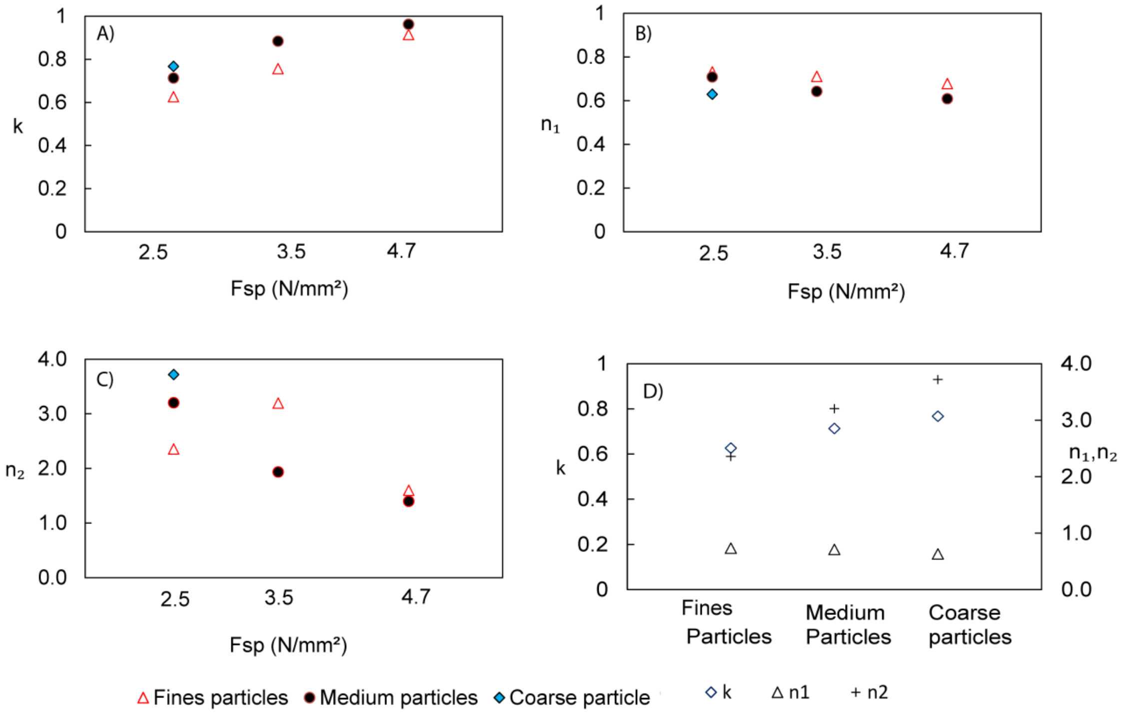

Figure 84. Relationship between the breakage function parameters and the specific pressing force. A) k parameters against Fsp, B) n_1 against Fsp, C) n_2 against Fsp and D) behaviour of all parameters and their size ranges under a specific pressing force of 2.5 [N/mm2].

7.4.2. Gap behaviour in High pressure grinding rolls

The gap, defined as the minimum distance between the rolls during the grinding operation, is not static. The floating rolls create two types of gap: the zero-gap, which is the initial set up of the rollers, and the working gap, which is produced when the material passes through the mill rolls. The behaviour trend of this operative condition was also studied in order to determine its relationship with some other characteristic of the process or with the material itself. For the large HPGR type, the zero-gap is 10 cm. Figure 85 shows the operational gap for all tests of groups I to V. The different values of the gap for the previously defined categories are easily observable. When the feed particle size increases, represented by the top-size parameter D_{80}, the operational gap also increases (Figure 85A). However, at a certain cut-point, the trends are inversed: for the heterogeneous feed particle size distribution, the D_{80} decreases and the gap continues increasing.

There is an evident influence of the specific pressing force on the working gap (Figure 85B), and it seems not to have much relation to the roll speed (Figure 85C). The material moisture appears more dispersed when compared with the gap size (Figure 85D).

The material porosity refers to the voids or spaces that exist between particles, and the cavities within each particle. The perceptible step in the size of the gap produced in the last category group may be related to the change in the porosity of the mill feed material (Figure 85E). In the cases of relatively mono-size feed materials (from categories I to IV) the porosity remains constant. The heterogeneous distribution of particle sizes (category V) generates a filling of the cavities produced by the larger particles at the expense of the smaller particles, causing a decrease of the porosity. Thus, a more cohesive and competent material is formed, creating a resistance of the same material against compression, and therefore a greater opening of the working gap.

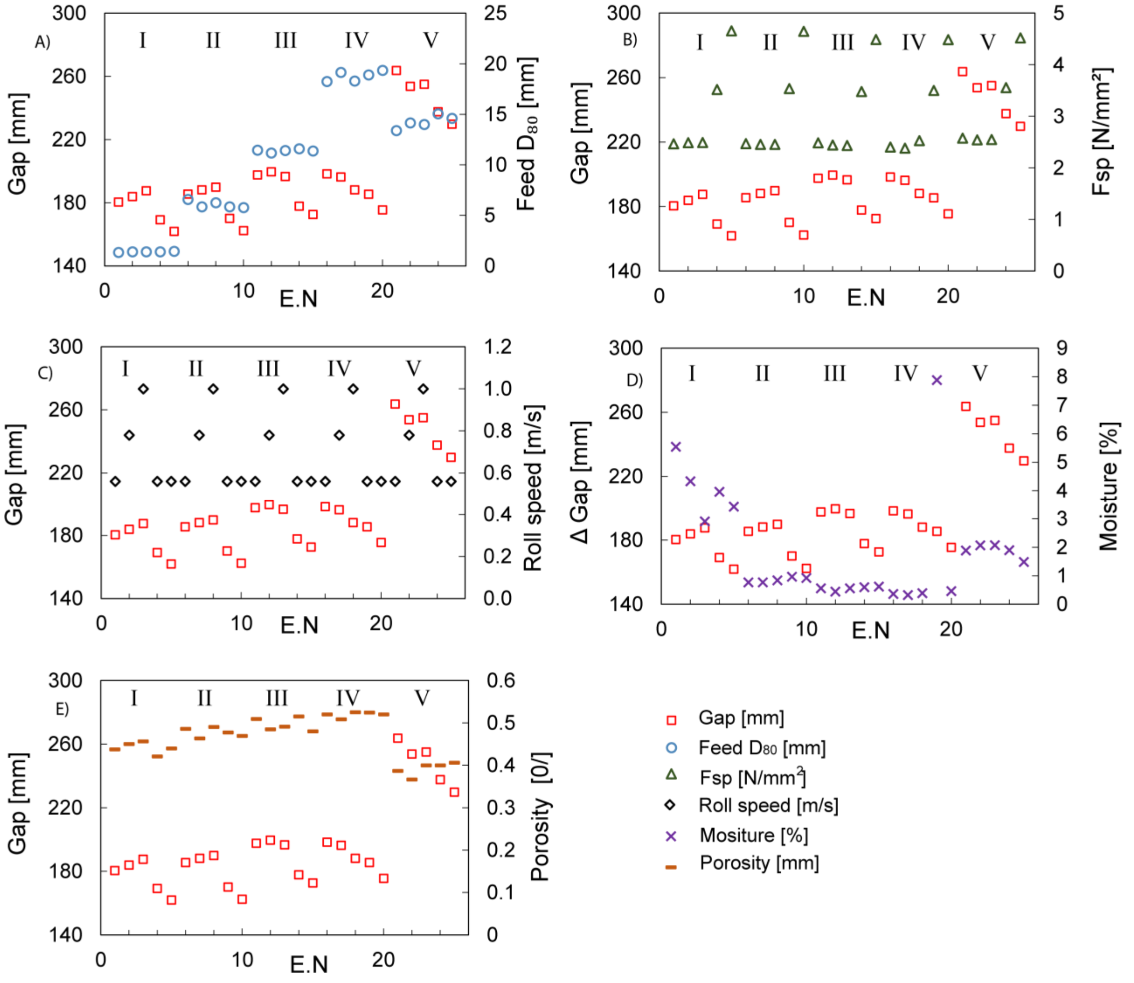

Figure 85. Graphics showing the relationship of the operational gap with other process characteristics, where N. E is the experimental number. A) gap against feed D_{80}, B) gap against specific pressing force Fsp, C) gap against roll speed, D) gap against material moisture, E) gap against material porosity.

Comparing the characteristics against each other, more relations can be established. The working gap behaves in a way that is directly proportional to the feed particle size distribution, which is represented by the value D_{80}. The particle sizes of groups I to IV are slightly positively sloped (Figure 86A) for all HPGR tests, except for group V, in which the gap size is considerable increased with respect to the rest of the values. As seen in Figure 86A, in the tests with same specific pressing force but varying roll speed, in the plot against the feed size (Figure 86B), no variations in the working gap are observed. However, some points from the V group are isolated from the others points. It seems that all tests with an increment of the porosity show low resistance of the floating roll to the material, leading to an increase of the working gap size.

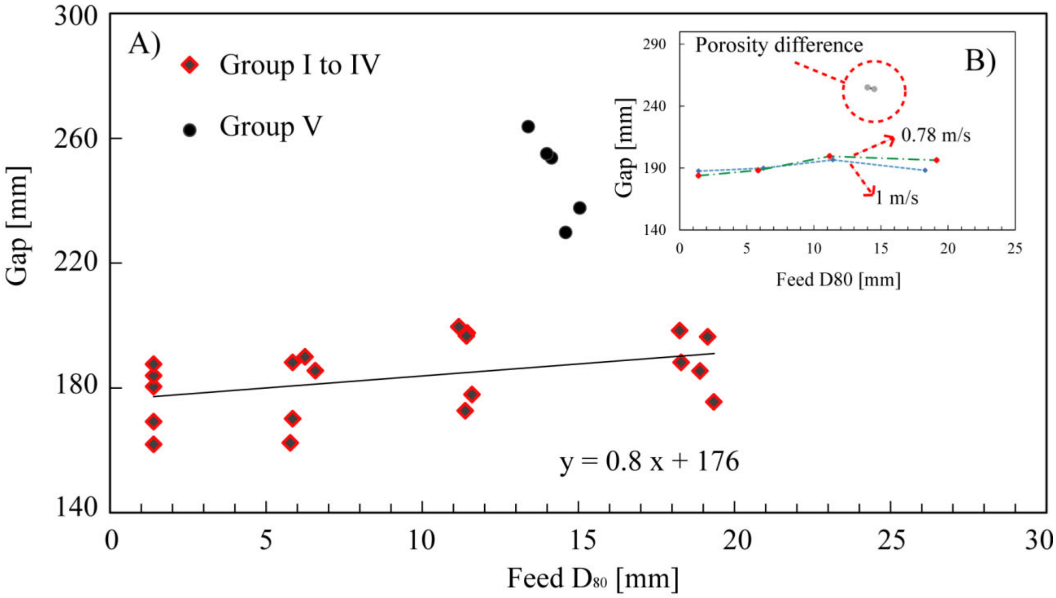

Figure 86. Plots of the trends discovered in the gap size and some process conditions, in this case, the top-feed size D_{80}. A) gap against feed D_{80} of al test, B) gap against feed D_{80} taking test with same pressure but varying roll speed.

Figure 87 shows how the size of the working gap is influenced by the specific pressing force. The average slope value is 11.67, and 0.52 is the standard deviation between all curves; the trend is the same for all particle size classes when the tests are conducted with the same specific pressing force.

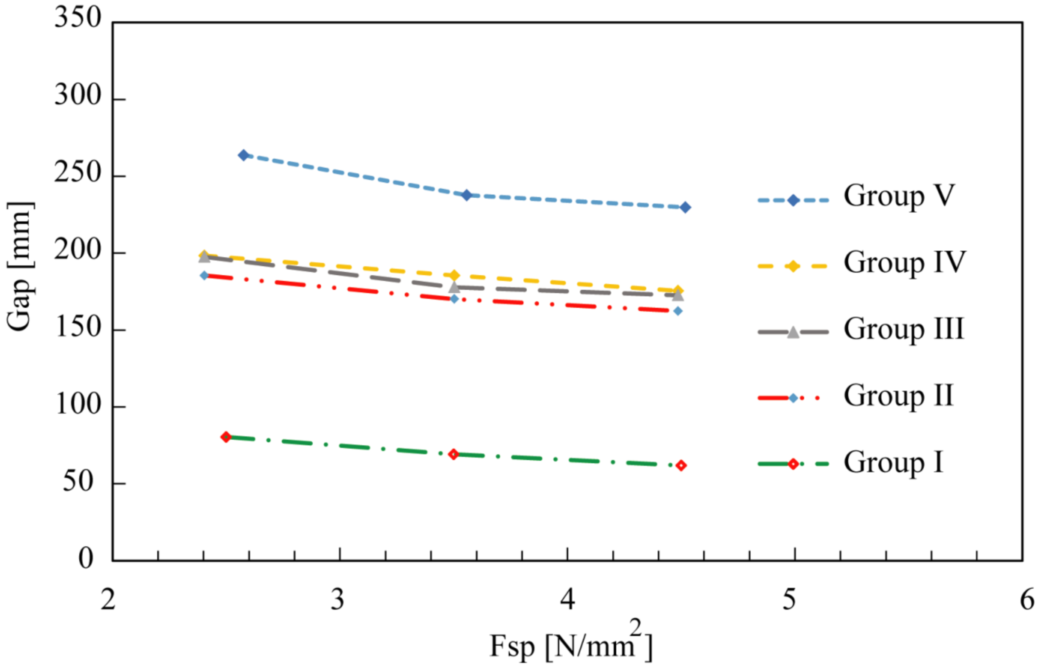

Figure 87. The working gap results are plotted against the specific pressing force, when the test are run with same roll speed.

The porosity is another key parameter in the working gap overture. The porosity ranged from 0.36 to 0.41(differential values), representing the tests with a value of the working gap size that was over 220 mm (Figure 88). It is also interesting to observe small variations in group V when the specific pressing force increases: the floating roll reacts to this, producing the gap size increment (from 225 mm to 250 mm), even when the porosity range between them is imperceptible (0.40-0.41).

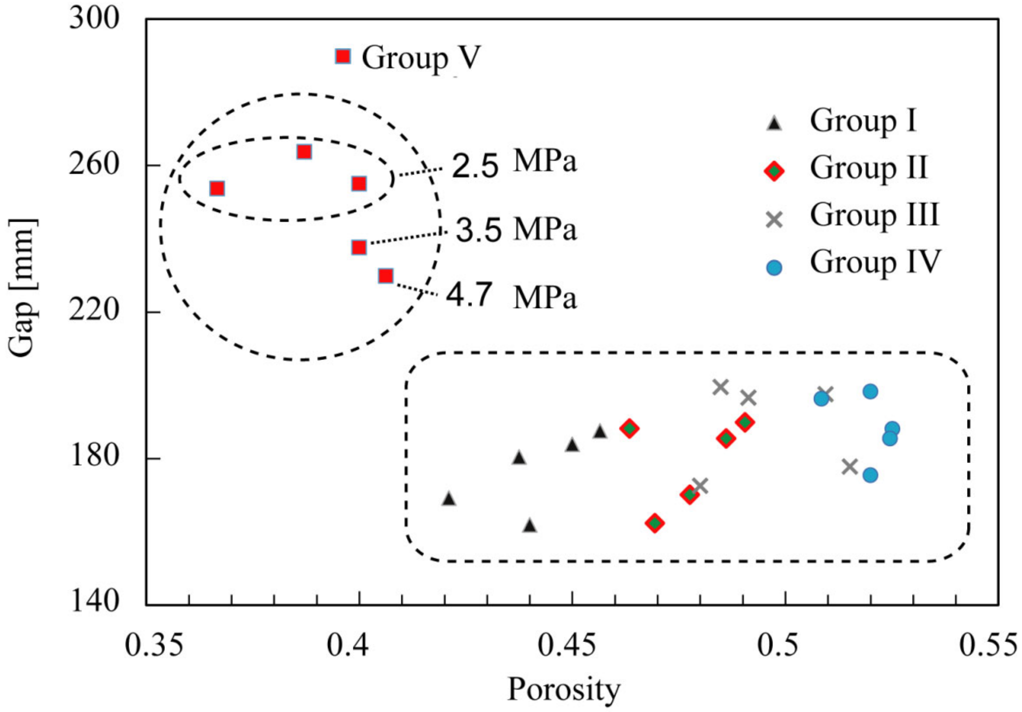

Figure 88. Working gap as affected by the material porosity. The dotted circles indicate tests from the same group and inside the tests with their specific pressing forces.

Despite the dispersion of the material porosity shown in Figure 86B, Figure 89 indicates some tendencies of the working gap size under a certain limited humidity range. It is possible that for some moisture values, the material resistance is stimulated to the point of compression, favouring the movement of the rollers, and then increasing the working gap size.

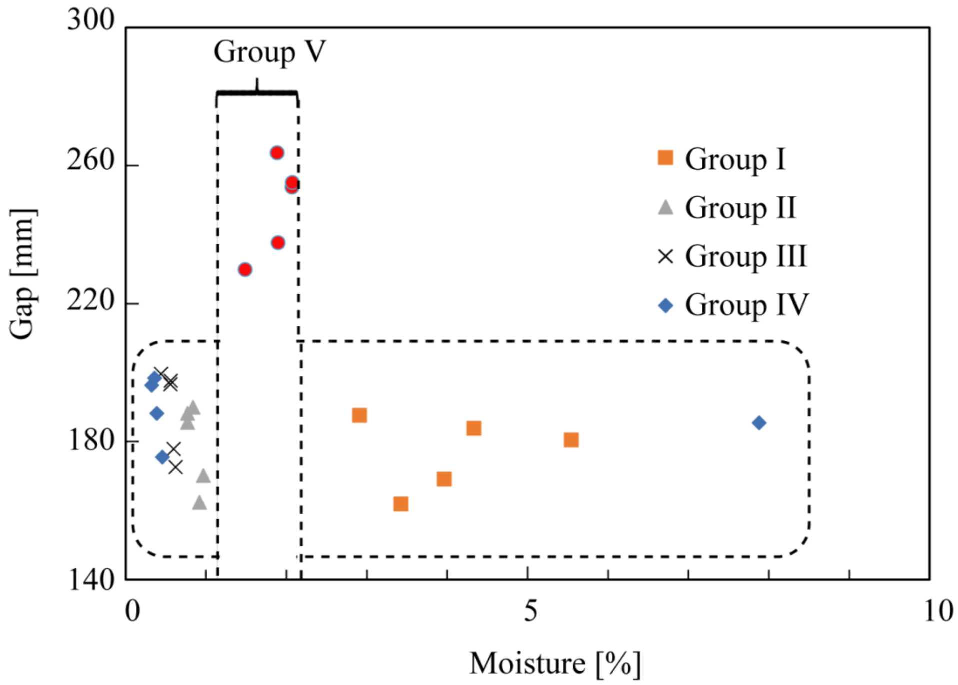

Figure 89. Working gap compared with material moisture.

After these observations, a comparison with previous phenomenological models was undertaken, and they show some coincidences in the working gap determination (Figure 90). However, it does not fit well in the high porosity zone.

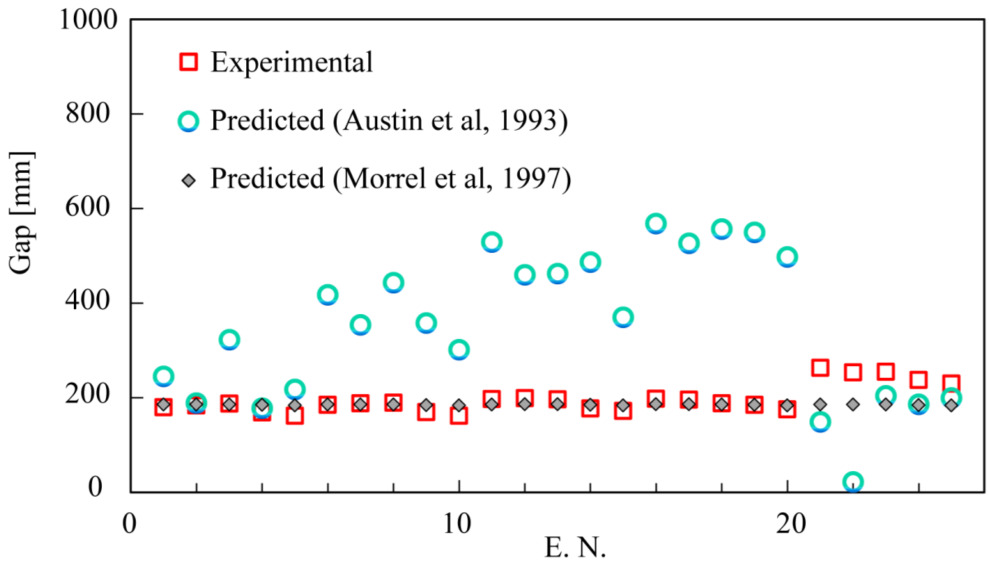

Figure 90. The experimental data and predicted values from Austin et al (1993) and Morrel et al (1997) of the working gap.

7.5. Energy consumption dependency

In order to optimize production, the results of the industrial scale HPGR were analysed in terms of energy consumption and product characteristics. The specific work, also denominated specific energy demand, is a balanced energy consumption, in which the throughput is involved. The connection between pressure and roll speed with this two outputs are shown in Figure 91. The specific work is measured by the load torque generated by all the load, friction and roll movement. The energy consumption is related with the specific work and the throughput of the feed material. The green line shows how the energy consumption is increased with the roll speed increment. This variation is also observed when the specific pressing force is varied, with the pink dotted line. The slope is higher when the variation of the roll speed is produced. For process purposes, the energy consumption is more relevant at higher throughput rather than the increment of the size reduction, which is the main effect on the product when the specific pressing force varies.

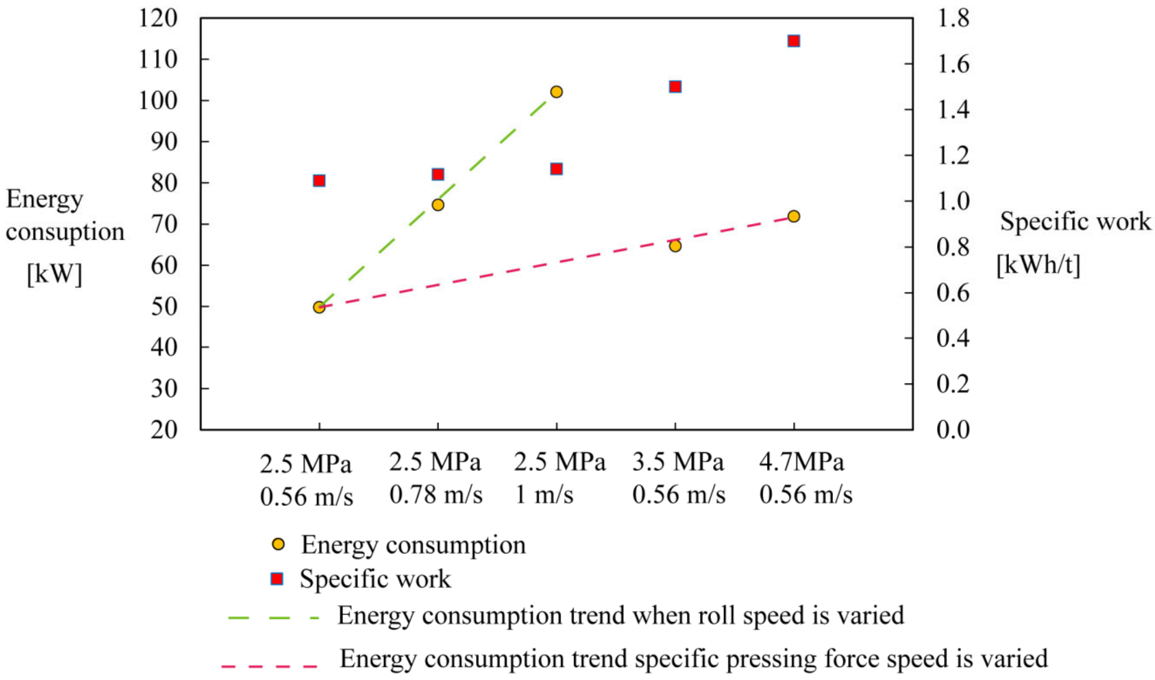

Figure 91. Plot showing specific work, energy consumption when specific pressure or roll speed vary.

The throughput is the most energy consumption agent, being directly proportional with the increment on the rolls speed (Figure 92). When the roll speed remains constant, the throughput also is constant and the energy consumption is only specific pressing force dependent.

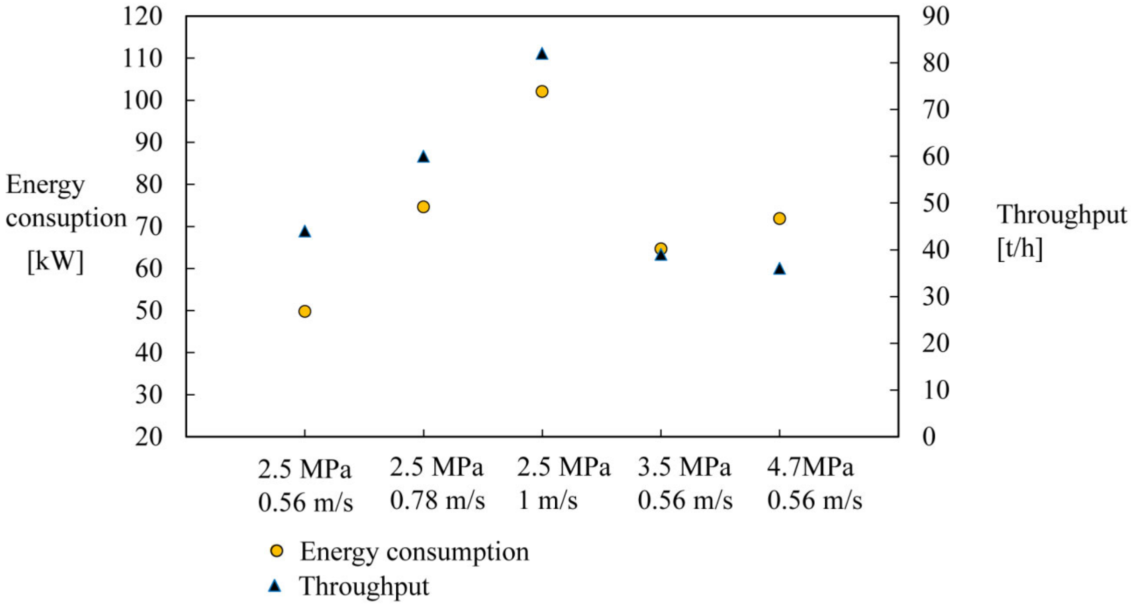

Figure 92. Energy consumption compared with throughput variation.

For product characteristic needs, the energy consumption is also increased, in such a way to get higher reduction ratios (Figure 93). However, this increment in the energy is not relevant as when the roll speed increases.

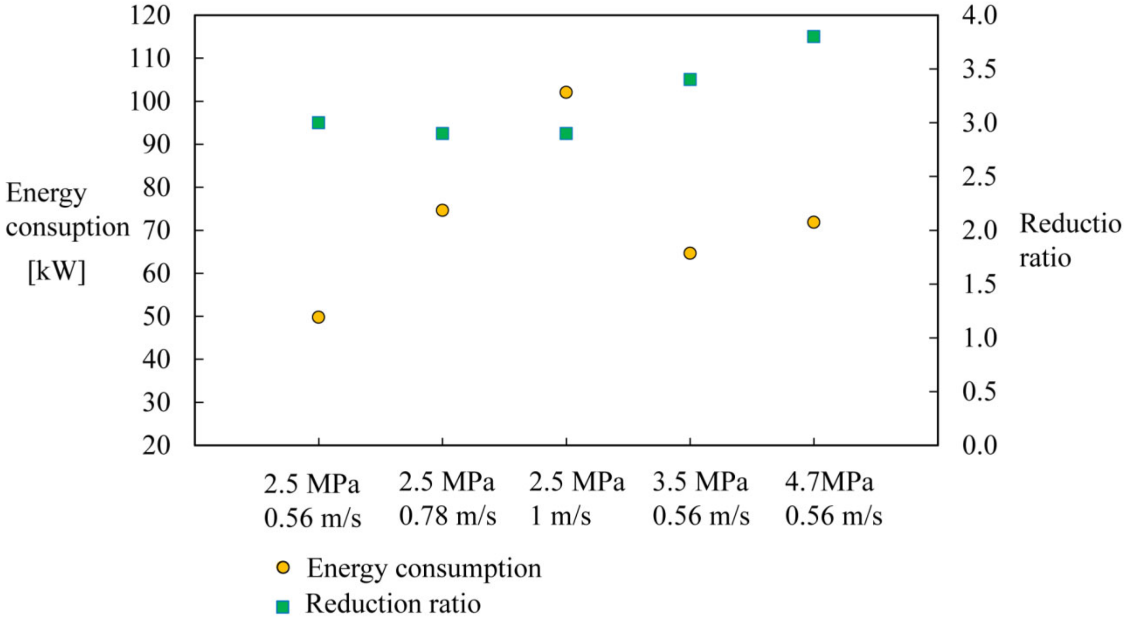

Figure 93. Energy consumption compared with reduction ratio variation.

A matrix analysis is presented in order to summarize the different studied parameters involved in this kind of machinery (Table 32). The model parameters are highly dependent on the material mineralogy, but also on the process condition when the material is under single particle compression or bed particle compression. The throughput is clearly roll speed dependent, but the product characteristic is specific pressing force, feed particle size distribution and mineralogy dependent, and compression condition as well.

Table 32. Influence of all model parameters and output with the operative conditions in industrial HPGR. The term "condition" is referred to single particle compression or bed particle compression.

Parameters	Fsp	dp	Condition	V	Feed size	Operative gap	Mineralogy
k	🟢	🟢	🟢	🔴	🔴	🔴	🟢
n1	🔵	🔵	🔵	🔴	🔴	🔴	🟢
n2	🟢	🟢	🟢	🔴	🔴	🔴	🟢
Throughput	🔴	🔴	🔴	🟢	🔵	🔴	🔴
Product	🟢	🟢	🟢	🔴	🟢	🔵	🟢

🟢 Highly dependent
🔵 Sligthly dependent
🔴 Not dependent

CHAPTER VI

Conclusions

8. CONCLUSIONS

The High pressure grinding rolls have been study in all its phases and approaches. Several conclusions are obtained from this study, based on the experimental results, validation and discussion:

1. The mechanical behaviour of the material was determined, by mean of a new methodology to find the breakage distribution function: the piston-die test. This new procedure gives an overview of how the particle breaks under two main conditions: single particle compression and bed particle compression. Furthermore, it has been found that the breakage distribution function is also non-normalizable when is under specific pressing force variation and for particle size range.
2. The breakage distribution function is a mathematical expression that show how is the particle size daughter fraction from a parent particle population under certain breakage mechanism. In this case, the function represents how the particles collapse and break under pressurizing conditions and the evolution of the parameters determination have contributed to the new reformed model for high pressure grinding rolls. This new approach takes the new finding in the compression behaviour of the particles and a selection function based on the same criteria of selective compression in different compression stages.
3. The determined parameters of the breakage distribution function was proven to be closely linked with the mineral composition of the tested material. The content of competent minerals or the presence of altered phases, resulted on variation on these parameters values: the parameter k was the one responsible of fines particles generation, and in a minor grade, the parameter n_1. The value of the parameter k ranges from 0 to 1, and the low percentage of quartz content should give values over 0.5 on this parameter: the piston-die test resulted in $k=0.68$, which is in agreement with the mineral characterization. This fact is complemented with the high content of albite and kaolinite, generating more quantity of fines. In this case, is possible to determine, or to predict an approximate value of the parameter k and n_l with two criteria: the piston-die test and the initial mineral characterization.
4. The model was proved using three different materials types, from the mineralogical composition and mechanical behaviour point of views. In a first instance, the model should correctly predict the comminution of any material. The error range in the lab-scale experiments were less than 10 RMSE in almost all the cases, but it showed some discordances when the specific pressing force was varied

5. The industrial scale test was performed using the same breakage functions parameters determination methodology, but including the specific pressing force into the piston-die procedure. The prediction of the product in this case was remarkable, reaching less than 2 RMSE in many cases.
6. The working gap was studied, determining its dependency on operative conditions or material characteristics as composition, size or moisture. There are models created to predict the gap size, but further studies are necessary in this field.
7. The energy consumption was determined and related with the product characteristics and the throughput, two critical parameters for the comminution industry. It has been found how the roll speed is the most energy demanding concept in this type of machinery, and is the responsible of the plant throughput. The specific pressing force, which has an influenced on the product characteristic, has an important influence on the energy demand as well, but is not as high as in the case of the increment on the roll speed.
8. The current models to predict product of HPGR uses different breakage distribution function compared with the present model of this study. One of these function is the so called T_{10}, based on the impact energy, but in this case, should be based on the compression energy. It would be interesting to compare the different functions, and if you have any agreement between them. Further research is necessary in this field.

REFERENCES

Abouzeid, A.Z.M., Fuerstenau, D.W. (2009). Grinding of mineral mixtures in high-pressure grinding rolls. International Journal of Mineral Processing, 93, 59–65.

Andrews, J. and Mika, T. (1976) Comminution of heterogeneous material. Development of a model for liberation phenomena. Proceedings of the 11th International Mineral Processing Congress, 59-88.

Apling, A., Bwalya, M. (1997). Evaluating high pressure milling for liberation enhancement and energy saving. Mineral Engineering, 10-9, 1013-1022.

Austin, L. G., Luckie, P. T. (1971). The estimation of Non-normalized breakage distribution parameters from batch grinding test. Powder technology, 267-271.

Austin, L. G., Luckie, P. T. (1972). Methods for determination of breakage distribution parameters. Powder technology 5, 215-222.

Austin, L.G., Concha, F. (1994). Diseño y simulación de circuitos de molienda y clasificación. Programa iberoamericano de ciencia y tecnología para el desarrollo, CYTED.

Austin, L.G., Weller, K.R., Lim, I.L. (1993). Phenomenological Modelling of the High Pressure Grinding Rolls, Proceedings of the XVIII International Mineral Processing Congress, 1, 87-95.

Austin, L.G., Trubelja, P.M. (1994). The capacity and product size distribution of high pressure grinding rolls. Mineral Processing and environment. In: Castro, S. and Concha, F. (Eds.), Mineral Processing and Environment. Proceedings of the IV Meeting of the southern hemisphere of mineral technology. 49-67. Universidad de Concepción, Chile.

Ahmad, S., H., Alfonso, P., Anticoi, H., Guasch, E., Oliva, J., Dosbaba, M., Garcia-Valles, M., Chugunova, M. (2018). Quantitative mineralogical comparison between HPGR and ball mil products of a Sn-Ta ore. Minerals, 8, 151.

Allain, E., Kanari, N., Diot, F., Yvon, J. (2019). Development of a process for the concentration of the strategic tantalum and niobium oxides from tin slags. Mineral Engineering, 134, 97-103.

Anticoi, H., Guasch, E.,Ahmad, S.H , Oliva, J., Alfonso, P., Bascompta, M., Sanmiquel, L., Escobet, T., Escobet, A., Parcerisa, D., Peña-Pitarch, E., Argelaguet, R., de Felipe, J. J. (2018). An Improved High-Pressure Roll Crusher Model for Tungsten and Tantalum Ores. Minerals, 8, 483.

Anticoi, H., Guasch, E., Hamid, S.A., Alfonso, P., Oliva, J., Bascompta, M., Sanmiquel, L., Escobet, A., Argelaguet, R., Escobet, T. (2018). Breakage function for HPGR: Mineral and mechanical characterization of tantalum and tungsten ores. Minerals, 8, 170.

Alfonso, P., Hamid, S., Garcia-Valles, M., Llorens, T., López Moro, J., Tomasa, O., Calvo, D., Guasch, E., Anticoi, H., Oliva, J. (2018). Textural and mineral-chemistry constraints on columbite-group minerals in the Penouta deposit: Evidence from magmatic and fluid-related processes. Mineralogical Magazine. 82, S1, 199-222.

Alfonso, P., Castro, D., Garcia-Valles, M., Tarragó, M., Tomasa, O., Martinez, S. (2016). Recycling of tailings from the Barruecopardo tungsten deposit for the production of glass. Journal of Thermal Analysis and Calorimetry 2016, 125(2), 681–687.

Barrios, G.K., Tavares, L.M. (2016). A preliminary model of high pressure roll grinding using the discrete element method and multi-body dynamics coupling. International Journal of Mineral Processing, 156, 32-42.

Baum, W., Ausburn, K. (2011). HPGR comminution for optimization of copper leaching. Mining, Metallurgy & Exploration, 28, 77-81.

Benzer, H.; Aydogan, N.; Dundar, H. (2011). Investigation of the breakage of hard and soft components under high compression: HPGR application. Mineral Engineering, 22, 303-307.

Broadbent, S.R. and Callcott, T.G., (1956) A matrix analysis involving particle assemblies. Philosophical Transactions of the Royal Society of London. Series A, Mathematical and Physical Sciences, 249(960), 99-123.

Ballantyne, G. R., Hilden, M., van der Meer, F. P. (2018). Improved characterisation of ball milling energy requirements for HPGR products. Minerals Engineering 116, 72-81.

Bouchard, J., Leblanc, G., Germain, Y., Levesque, M., Tremblay, N., Légaré, B., Dallaire, D., Radziszewski, P. (2016). The CMIC/CanmetMINES comminution energy recovery potential initiative - the Agnico Eagle Goldex division case. In: Proceedings of the XXVIII International Mineral Processing Congress. Québec, Canada.

Buckingham, L., Dupont, J.,Stieger, J., Blain, B., Brits, C. (2011). Improving energy efficiency in Barrick grinding circuits. In: Proceedings of the V International Conference on Autogenous and Semiautogenous Grinding. Vancouver, Canada.

Černý, P, Blevin, P L, Cuney, M, London, D (2005) Granite-related ore deposits. Econ Geol 100th Anniversary. V: 337–370

Charikinya, E., Bradshaw, S., Becker, M. (2015). Characterising and quantifying microwave induced damage in coarse sphalerite ore particles. Minerals Engineering, 82, 14-24.

Daniel, M. (2007). Energy Efficient Mineral Liberation Using HPGR Technology. University of Queensland, Australia. PhD thesis.

Daniel, M.J., Morrell, S. (2004). HPGR model verification and scale-up. Minerals Engineering, 17 (11–12), 1149–1161.

Dundar, H.; Benzer, H.; Aydogan, N. (2013). Application of population balance model to HPGR crushing. Mineral Engineering, 50-51,114-120.

Daniel, M.J., Morrell, S. (2004). HPGR model verification and scale-up. Minerals Engineering 17 (11-12), 1149-1161.

Datta, A., Rajamani, R.K., (2002). A direct approach of modelling batch grinding in ball mills using population balance principles and impact energy distribution. International Journal of Mineral Processing. 64, 181-200.

Esnault, V.P.B., Zhou, H., Heitzmann, D. (2015). New population balance model for predicting particle size evolution in compression grinding. Minerals Engineering, 73, 7-15.

Evertsson, C.M.; Bearman, R.A. (1997). Investigation of inter-particle breakage as applied to cone crushing. Mineral Engineering, 10, 199-214.

Fernandez, M.G., Brochot, S. (2014). HPGR modelling with mineral liberation for plant optimization. Proceedings of the 27th International Mineral Processing Congress, IMPC , 21-31.

Fuerstenau, D.W., Abouzeid, A.Z., (2002). The energy efficiency of ball milling in comminution. International Journal of Mineral Processing. 67 (4), 161-185.

Fuerstenau, D.W., Kapur, P.C. (1994). A new approach to assessing the grindability of solids and the energy efficiency of grinding mills. Minerals and Metallurgical Processing 11, 210.

Fuerstenau, D.W., Shukla, A., Kapur, P.C. (1991). Energy consumption and product size distribution in choke-fed high compression roll mill. International Journal of Mineral Processing, 32, 59.

Genç, Ö. Benzer, A.H. (2016). Effect of High Pressure Grinding Rolls (HPGR) pre-grinding and ball mill intermediate diaphragm grate design on grinding capacity of an industrial scale two-compartment cement ball mill classification circuit. Mineral Engineering, 92, 47-56.

Ghorbani, Y., Mainza, A.N., Petersen, J., Becker, M., Franzidis, J-P., Kalala, J.T. (2013). Investigation of particles with high crack density produced by HPGR and its effect on the redistribution of the particle size fraction in heaps. Mineral Engineering, 43-44, 44-51.

Ghorbani, Y., Becker,M., Mainza,M., Franzidis,J-P., Petersen, J. (2011). Large particle effects in chemical/biochemical heap leach processes - A review. Minerals Engineering, 24, 1172-1184.

Guasch, E.; Anticoi, H.; Hamid, S.A.; Alfonso, P.; Oliva, J.; Escobet, T. (2018). New approach to ball mill modelling as a piston flow. Mineral Engineering, 116, 82–87.

Guevara F., Menacho J. (1993). Modelación mecánica y metalúrgica del molino de rodillos de alta presión. Centro de lnvestigación Minera y Metalúrgica, Santiago de Chile, 547-563.

Gupta, A. and Yan, D.S. (2006) Mineral Processing Design and Operations. Elsevier. ISBN 0 444 51636 0.

Hasanzadeh, V., Farzanegan, A. (2011). Robust HPGR model calibration using genetic algorithms. Minerals Engineering 24, 424–432.

Hill, P., Ka, M. (1996). Statistics of multiple particle breakage. American Institute of Chemical Engineers Journal 42-6, 1600-1611.

Han, Y., Liu, L., Yuan, Z., Wang, Z., Zhang, P. (2012). Comparison of low-grade hematite product characteristics in a high-pressure grinding roller and jaw crusher. Mining, Metallurgy & Exploration, 29, 75-80.

Hinde, A.L., Kalala, J.T. (2009). The application of a simplified approach to modelling tumbling mills, stirred media mills and HPGR's. Minerals Engineering, 22(7-8), 633-641.

Holl, R. (1979). Time- and stratabound early paleozoicscheelite, stibnite and cinnabar deposits in the Eastern Alps. Proceed 3ª ISMIDA, Leoben, Oct., 195-213.

Instituto de Estudos do Territorio, IET. 2019. https://cmatv.xunta.gal/organizacion/c/CMAOT_Instituto_Estudos_Territorio. Consulted 21/03/2019. 12:23 hrs.

Jønsson, J. B., Flod, N. (2011). Mining ‘from below’: Taking Africa‘s artisanal miners seriously. Geography compass 5/7, 479-493.

Kanda, Y., sano, S., Yashima, S. (1986). A consideration of grinding limit base on fractures mechanics. Powder Technology, 48: 263-267.

Kazerani, R. Sam, A. (2017). The wear pattern in high pressure grinding rolls. Mineral processing and extractive metallurgy, 126-4, 238-244.

Kellerwessel, H, (1990). High pressure material bed comminution in practice. Zement-Kalk-Gips 2, 57–64.

Kelly, E.G.; Spottiswood, D.J. (1990). The breakage function; what is it really? Mineral Engineering, 3, 405-414.

King, R.P. (2012). Modelling and Simulation of Mineral Processing Systems; Butterworth-Heinemann: Oxford, UK,

Klymowsky R, Patzelt N, Knecht J, Burchardt E. (2002). Selection and sizing of high pressure grinding rolls. In: A Mular, D Halbe, D Barratt, editor. Mineral processing plant design, practice, and control proceedings. 1st ed. Littleton: SME, 636–668.

Korinek, G. J. (1998). Tantalum in electrolytic capacitors. Tungsten and refractory metals 2. Bose and R. J. Dowding.MPIF, 587-596

Kwon, J., Cho, H., Mun, M., Kim, K. (2012). Modelling of coal breakage in a double roll crusher considering the re-agglomeration phenomena. Powder Technology, 232, 113-123.

King, R. P. (1990). Calculation of the liberation spectrum in products produced in continuous milling circuits. Proceedings 7th European Symposium on comminution, Ljubljana, June, 2, 429-444

King, R.P., Schneider, C.L. (1998). Mineral liberation and the batch comminution equation. Mineral Engineering, 11-12, 1143-1160.

Kodali, P., Dhawan, N., Depci, T., Lin, C.L., Miller, J.D. (2011). Particle damage and exposure analysis in HPGR crushing of selected copper ores for column leaching. Minerals Engineering, 24, 1478-1487.

Levesque, M. Y., Millar, D. L. (2015). The link between operational practices and specific energy consumption in metal ore milling plants-Ontario experiences. Mineral Engineering, 71, 146-158.

Liang, G., Wei, D., Xu, X., Xia, X., Li, Y. (2016). Study on the Selection of Comminution Circuits for a Magnetite Ore in Eastern Hebei, China. Minerals, 6(2), 39.

Liu, L., Tan, Q., Liu, L., Cao, J. (2018). Comparison of different comminution flowsheets in terms of minerals liberation and separation properties. Mineral Engineering, 125, 26-33.

Linnen, R L, Samson, I M, Williams-Jones, A. E., Chakhmouradian, A. R. (2014). Geochemistry of the Rare-Earth Element, Nb, Ta, Hf, and Zr Deposits In: Holland, Heinrich, Turekian, Karl (eds) Reference Module in Earth Systems and Environmental Sciences Treatise on Geochemistry, 2nd ed 13 Elsevier, pp 543–564

Llorens Gonzalez, T., Gargcía Polonio, P., López Moro, F. J., ferenandez Fernandez, A., Sanz Contreras, J. L., Moro Benito, M. C. (2017). Tin-Tantalum-niobium mineralization in the Penouta deposit (NW Spain): Textural features and mineral chemistry to unravel the genesis and evolution of cassiterite and columbite group minerals in a peraluminous system. Ore Geology Reviews. 81, 79-95.

López-Moro, F. J., Gracía Polonio, F., Llorens Gonzalez, T., Sanz Contreras, J. L., Fernández Fernández, A., Moro Benito, M. C. (2017). Ta and Sn concentration by muscovite fractionation and degassing in a lens-like granite body: the case of study of the Penouta rare-metal albite granite (NW Spain). Ore Geology Review, 82, 10-30.

Mackay, D. A. R., Simandl, G. J. (2014) Geology, market and supply chain of niobium and tantalum- a review. Mineralium Deposita, 49, 1025–1047

Mangas, J., Arribas, A. (1991). Fluid inclusion study of tin-mineralized greisens and quartz veins in the Penouta apogranite (Orense, Spain). Mineralogical Magazine, 55, 211-223.

Monov, V., Sokolov, B., Stoenchev, S. (2012). Grinding in ball mills: Modelling and process control. Ybernetics and information technologies, 12-2, 51-68.

Morrel, S., Lim, W., Tondo, L. (1997). Modelling and scale up of the high pressure grinding rolls. In: Proceedings of the. XX International Mineral Congress. IMPC, Aachen, Germany.

Mosser, K, D. (1999). The manufacturer and fabrication of tantalum. Journal of The Minerals, Metals & Materials Society, 51, 29-31.

Napier-Munn, T. J., Morrel, S., Morrison,R.D., Kojovic, T. (1996). Mineral Comminution Circuits: Their operation and optimization. JKMRC Mining and mineral processing.

Nikolov, S. (2002). A performance model for impact crushers. Minerals Engineering, 15, 715-721.

Nikolov, S. (2004). Modelling and simulation of particle breakage in impact crushers. International Journal of Mineral Processing, 74S, S219–S225.

Numbi, B.P., Xia, X. (2015). Systems optimization model for energy management of a parallel HPGR crushing process. Applied Energy, 149, 133-147.

Özbek, A., Gül, M., Karacan, E., Alca, Ö. (2018). Anisotropy effect on strengths of metamorphic rocks. Journal of rock mechanic and geotechnical engineering. 10, 164-175.

Pérez-García, E.M., Bouchard, J., Poulinc É. (2018). Integration of a liberation model in a simulation framework for comminution circuits. Mineral Engineering, 126, 167-176.

Raith, J. G., Schmidt, S. (2010). Tungsten deposit Felbertal, Salzburg, Austria. Acta Mineralogica-Petrographica, 3, 1-24

Radziszewski, P. (2013). Energy recovery potential in comminution processes. Mineral Engineering, 46-47, 83-88.

Reid, K.J. (1965). A solution to the batch grinding equation. Chemical Engineering Science, 20, 953-963.

Rietveld, H.M. (1969). A profile refinement method for nuclear and magnetic structures. Journal of Applied Crystallography, 2, 65-71.

Roy, K., Das, R.N., Ambure, P., Aher, R. (2016). Be aware of error measures. Further studies on validation of predictive QSAR models. Chemical Intelligent Laboratory System, 152, 18–33.

Saramak, D. (2011). Technological issues of high-pressure grinding rolls operation in ore comminution processes. Archives of Mining Sciences, 56, 517-526.

Sbárbaro, D., Del Villar, R. (2010). Advanced Control and Supervision of Mineral Processing Plants. Springer London Dordrecht Heidelberg New York.

Schönert, K. (1988). A first survey of grinding with High-compression roller mills. International Journal of Mineral Processing, 22, 401-412.

Schneider, C. L., Alves, V. K., Austin, L. G. (2009). Modeling the contribution of specific grinding pressure for the calculation of HPGR product size distribution. Mineral Engineering, 22, 642-649.

Sousa, R., Simons, B., Bruc, K, Botelho de Sousa, A., Rollinson, G., Andersen, J., Martin, M., Machado Leitea, M. (2018). Use of mineral liberation quantitative data to assess separation efficiency in mineral processing – Some case studies. Mineral Engineering, 127, 134-142.

Strategic minerals Spain. 2019. www.strategicminerals.com. Consulted 21/03/2019, 12:21 hrs.

Tromans, D., Meech, J.A., (2004). Fracture toughness and surface energies of covalent minerals: theoretical estimates. Mineral Engineering, 17 (1), 1–15.

Tavares, L.M., (2005). Particle weakening in high-pressure roll grinding. Mineral Engineering, 18, 651-657.

Tavares, L.M. King, R.P. (1998). Single-particle fracture under impact loading. International Journal of Mineral Processing, 54, 1-28.

Torres, M., Casali, A. (2009). A novel approach for the modelling of high-pressure grinding rolls. Minerals Engineering, 22, 1137-1146.

Vyhmeister, E., reyes-Bozo, L., Rodriguez-Maecher, R., Fúnez-Guerra, C., Cepeda-Vaca, F., Valdés-González, H. (2019). Modeling and energy-based model predictive control of high pressure grinding roll. Mineral Engineering, 134, 7-15.

Whiten, W.J. (1974) A matrix theory of comminution machines. Chemical Engineering Science, 29, 588-599.

Whiten, W.J., Walter, G.W. and White, M.E. (1979). A breakage function suitable for crusher models. Fracture at Work, 19.1–19.3.

Wills, B. (2015). Mineral processing technology. Pergamon press, Elsevier.

Willmott, C.; Matsuura, K. (2005). Advantages of the mean absolute error (MAE) over the root mean square error (RMSE) in assessing average model performance. Clim. Res., 30, 79-82.

Yin, W., Tang, Y., Ma, Y., Zuo, W., Yao, J. (2017). Comparison of sample properties and leaching characteristics of gold ore from jaw crusher and HPGR. Minerals Engineering, 111, 140-147.

Zhang, Y.D.; Buscanera, G.; Einav, I. (2016). Grain size dependence of yielding in granular soils interpreted using fracture mechanics, breakage mechanics and Weibull statistics. Géotechnique, 66, 149–160.

LIST OF ORIGINAL PAPERS

PAPER I

Anticoi, H., Guasch, E., Hamid, S.A., Alfonso, P., Oliva, J., Bascompta, M., Sanmiquel, L., Escobet, A., Argelaguet, R., Escobet, T. (2018). Breakage function for HPGR: Mineral and mechanical characterization of tantalum and tungsten ores. Minerals, 8, 170.

URI: https://doi.org/10.3390/min8040170

DOI:10.3390/min8040170

Data related to the paper:

Anticoi Sudzuki, H. F. (2018). Breakage function determination for HPGR [Dataset]. 1 v. Universitat Politècnica de Catalunya. https://doi.org/10.5821/data-2117-168957-1

URI: http://hdl.handle.net/2117/168957

DOI: 10.5821/data-2117-168957-1

PAPER II

Anticoi, H., Guasch, E.,Ahmad, S.H , Oliva, J., Alfonso, P., Bascompta, M., Sanmiquel, L., Escobet, T., Escobet, A., Parcerisa, D., Peña-Pitarch, E., Argelaguet, R., de Felipe, J. J. (2018). An Improved High-Pressure Roll Crusher Model for Tungsten and Tantalum Ores. Minerals, 8, 483.

URI: https://doi.org/10.3390/min8110483

DOI: 10.3390/min8110483

Data related to the paper:

Anticoi Sudzuki, H. F. (2018). High pressure roll crusher modelling [Dataset]. 1 v. Universitat Politècnica de Catalunya. https://doi.org/10.5821/data-2117-168964-1

URI: http://hdl.handle.net/2117/168964

DOI: 10.5821/data-2117-168964-1

PAPER III

Anticoi, H., Guasch, E.,Ahmad, Oliva, J., Alfonso, P., Bascompta, M., Sanmiquel, L. (2018). High-Pressure Grinding Rolls: Model validation and function parameters dependency on process conditions. Journal of materials science and research. In press

URI: Accepted for publication

DOI: Accepted for publication

Data related to the paper:

Anticoi Sudzuki, H. F. (2018). High pressure roll crusher modelling [Dataset]. 1 v. Universitat Politècnica de Catalunya. https://doi.org/10.5821/data-2117-168964-1

URI: http://hdl.handle.net/2117/169056

DOI: 10.5821/data-2117-169056-1

LIST OF CONGRESS PAPERS

Sarbast Hamid, Pura Alfonso, Eduard Guasch, Hernan Anticoi, Josep Oliva, and Teresa Escobet, (2017) Liberation Modelling Based on Comminution of Tungsten Ore Using Mineral Liberation Analysis. The 56th annual conference of metallurgists. Vancouver, Canada.

Alfonso, P.; Oliva, J.; Alvarez, B.; Jorge, J.; Sanmiquel, L.; Parcerisa, D.; Tomasa, O.; Calvo, D.; Guasch, E.; de Felipe, J.J.; Anticoi, H. (2015). Optimization of the tantalum ore production by control the milling process. In: Proceedings of the 2nd International Conference on Mining, Material and Metallurgical Engineering. pp. 344-1 - 344-4.

Guasch, E.; Anticoi, H.; Hamid, S.; Oliva, J.; Alfonso, P.; Escobet, T. (2016). New approach to ball mill modelling as a piston flow process. In: Comminution'16: 11-14 April 2016, Cape Town, South Africa. pp. 1 - 12.

Anticoi, H.; Guasch, E.; Hamid, S.; Oliva, J.; Alfonso, P.; Escobet, T. (2016). High-pressure grinding rolls modelling with population balance models applied to tantalum ore. In: Comminution'16: 11-14 April 2016, Cape Town, South Africa. pp. 1 - 12.

Guasch, E.; Anticoi, H.; Hamid, S.; Oliva, J.; Alfonso, P. (2016). High-pressure grinding rolls modelling with population balance models applied to tantalum ore. In: Conference Proceedings IMPC 2016. pp. 1 - 11.

Alfonso, P.; García-Vallès, M.; Hamid, S.; Tomasa, O.; Llorens, T.; Oliva, J.; Guasch, E.; Anticoi, H.; Garcia-Polonio, F. (2016). Rare-element mineralization in the Sn-Ta Penouta ore deposit, NW Spain. In: 2nd European Mineralogical Conference. Minerals, Rocks and Fluids: alphabet and words of planet Earth. Book of Abstracts. pp. 594.

Alfonso, P.; Hamid, S.A.; Guldris, L.; Guasch, E.; Anticoi, H.; Oliva, J.; López-Moro, J.; Llorens, T. (2017). Quantitative mineralogy for processing Ta-low grade ores: The Penouta deposit. In: GolschmidT 2017: abstracts. pp. 52. 2017.